4 Performance

The performance of an engineering material is judged by its properties and behavior under tensile, compressive, shear, and other static or dynamic loading conditions in both normal and adverse test environments. This information is essential for selecting the proper material in a given application as well as designing a structure with the selected material. In this chapter, we describe the performance of fiber-reinforced polymer composites with an emphasis on the general trends observed in their properties and behavior. A wealth of property data for continuous fiber thermoset matrix composites exists in the published literature. Continuous fiber-reinforced thermoplastic matrix composites are not as widely used as continuous fiber-reinforced thermoset matrix composites and lack a wide database.

Material properties are usually determined by conducting mechanical and physical tests under controlled laboratory conditions. The orthotropic nature of fiber-reinforced composites has led to the development of standard test methods that are often different from those used for traditional isotropic materials. These unique test methods and their limitations are discussed in relation to many of the properties considered in this chapter. The effects of environmental conditions, such as elevated temperature or humidity, on the physical and mechanical properties of composite laminates are presented near the end of the chapter. Finally, long-term behavior, such as creep and stress rupture, and damage tolerance are also discussed.

4.1 STATIC MECHANICAL PROPERTIES

Static mechanical properties, such as tensile, compressive, flexural, and shear properties, of a material are the basic design data in many, if not most, applications. Typical mechanical property values for a number of 0° laminates and sheet-molding compound (SMC) laminates are given in Appendix A.5 and Appendix A.6, respectively.

4.1.1 Tensile Properties

4.1.1.1 Test Method and Analysis

Tensile properties, such as tensile strength, tensile modulus, and Poisson's ratio of flat composite laminates, are determined by static tension tests in accordance

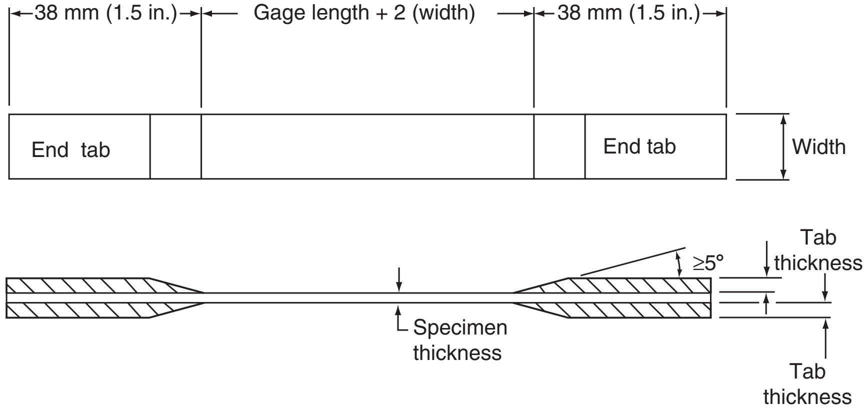

FIGURE 4.1 Tensile test specimen configuration.

with ASTM D3039. The tensile specimen is straight-sided and has a constant cross section with beveled tabs adhesively bonded at its ends (Figure 4.1). A compliant and strain-compatible material is used for the end tabs to reduce stress concentrations in the gripped area and thereby promote tensile failure in the gage section. Balanced [0/90] cross-ply tabs of nonwoven E-glass–epoxy have shown satisfactory results. Any high-elongation (tough) adhesive system can be used for mounting the end tabs to the test specimen.

The tensile specimen is held in a testing machine by wedge action grips and pulled at a recommended cross-head speed of 2 mm/min (0.08 in./min). Longitudinal and transverse strains are measured employing electrical resistance strain gages that are bonded in the gage section of the specimen. Longitudinal tensile modulus E_{11} and the major Poisson's ratio ν_{12} are determined from the tension test data of 0° unidirectional laminates. The transverse modulus E_{22} and the minor Poisson's ratio ν_{21} are determined from the tension test data of 90° unidirectional laminates.

For an off-axis unidirectional specimen ($0° < \theta < 90°$), a tensile load creates both extension and shear deformations (since A_{16} and $A_{26} \neq 0$). Since the specimen ends are constrained by the grips, shear forces and bending couples are induced that create a nonuniform S-shaped deformation in the specimen (Figure 4.2). For this reason, the experimentally determined modulus of an off-axis specimen is corrected to obtain its true modulus [1]:

$$E_{\text{true}} = (1 - \eta)\, E_{\text{experimental}},$$

where

$$\eta = \frac{3\bar{S}_{16}^2}{\bar{S}_{11}^2[3(\bar{S}_{66}/\bar{S}_{11}) + 2(L/w)^2]}, \tag{4.1}$$

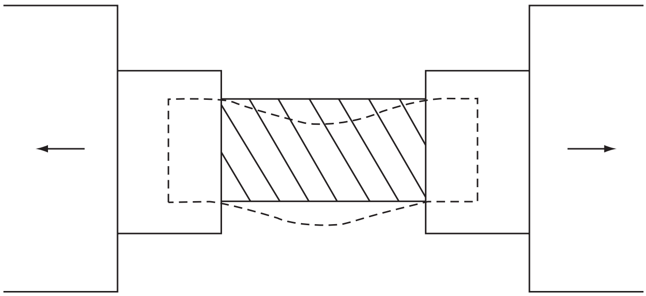

FIGURE 4.2 Nonuniform deformation in a gripped off-axis tension specimen.

where

L is the specimen length between grips

w is the specimen width

$\bar{S}_{11}$,$\bar{S}_{16}$, and $\bar{S}_{66}$ are elements in the compliance matrix (see Chapter 3)

The value of η approaches zero for large values of L/w. Based on the investigation performed by Rizzo [2], L/w ratios >10 are recommended for the tensile testing of off-axis specimens.

The inhomogeneity of a composite laminate and the statistical nature of its constituent properties often lead to large variation in its tensile strength. Assuming a normal distribution, the average strength, standard deviation, and coefficient of variation are usually reported as

$$\text{Average strength} = \sigma_{\text{ave}} = \sum \frac{\sigma_i}{n},$$

$$\text{Standard deviation} = d = \sqrt{\frac{\sum (\sigma_i - \sigma_{\text{ave}})^2}{(n-1)}},$$

$$\text{Coefficient of variation} = \frac{100d}{\sigma_{\text{ave}}}, \tag{4.2}$$

where

n is the number of specimens tested

σ_i is the tensile strength of the ith specimen

Instead of a normal distribution, a more realistic representation of the tensile strength variation of a composite laminate is the Weibull distribution. Using two-parameter Weibull statistics, the cumulative density function for the composite laminate strength is

$$F(\sigma) = \text{Probability of surviving stress } \sigma = \exp\left[-\left(\frac{\sigma}{\sigma_0}\right)^{\alpha}\right], \tag{4.3}$$

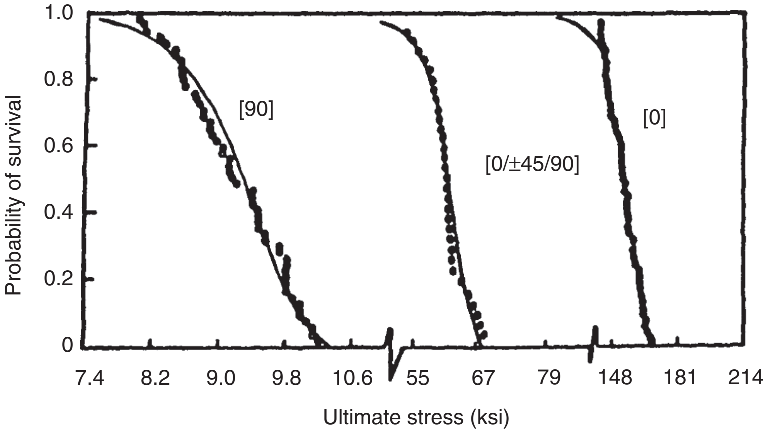

FIGURE 4.3 Tensile strength distribution in various carbon fiber–epoxy laminates. (Adapted from Kaminski, B.E., *Analysis of the Test Methods for High Modulus Fibers and Composites, ASTM STP*, 521, 181, 1973.)

where
  α is a dimensionless shape parameter
  σ_0 is the location parameter (MPa or psi)

The mean tensile strength and variance of the laminates are

$$\bar{\sigma} = \sigma_0 \Gamma\left(\frac{1+\alpha}{\alpha}\right),$$

$$s^2 = \sigma_0^2\left[\Gamma\left(\frac{2+\alpha}{\alpha}\right) - \Gamma^2\left(\frac{1+\alpha}{\alpha}\right)\right], \tag{4.4}$$

where Γ represents a gamma function.

Figure 4.3 shows typical strength distributions for various composite laminates. Typical values of α and σ_0 are shown in Table 4.1. Note that the decreasing value of the shape parameter α is an indication of greater scatter in the tensile strength data.

EXAMPLE 4.1

Static tension test results of 22 specimens of a 0° carbon–epoxy laminate shows the following variations in its longitudinal tensile strength (in MPa): 57.54, 49.34, 68.67, 50.89, 53.20, 46.15, 71.49, 72.84, 58.10, 47.14, 67.64, 67.10, 72.95, 50.78, 63.59, 54.87, 55.96, 65.13, 47.93, 60.67, 57.42, and 67.51. Plot the Weibull distribution curve, and determine the Weibull parameters α and σ_0 for this distribution.

TABLE 4.1
Typical Weibull Parameters for Composite Laminates

Material	Laminate	Shape Parameter, α	Location Parameter, σ_0 MPa (ksi)	
Boron–epoxy[a]	[0]	24.3	1324.2	(192.0)
	[90]	15.2	66.1	(9.6)
	$[0_2/\pm 45]_S$	18.7	734.5	(106.6)
	$[0/\pm 45/90]_S$	19.8	419.6	(60.9)
	$[90_2/45]_S$	19.8	111.9	(16.1)
T-300 Carbon–epoxy[b]	$[0_8]$	17.7	1784.5	(259)
	$[0_{16}]$	18.5	1660.5	(241)
E-glass–polyester SMC[c]	SMC-R25	7.6	74.2	(10.8)
	SMC-R50	8.7	150.7	(21.9)

[a] From B.E. Kaminski, *Analysis of the Test Methods for High Modulus Fibers and Composites, ASTM STP*, 521, 181, 1973.
[b] From R.E. Bullock, *J. Composite Mater.*, 8, 200, 1974.
[c] From C.D. Shirrell, *Polym. Compos.*, 4, 172, 1983.

SOLUTION

Step 1: Starting with the smallest number, arrange the observed strength values in ascending order and assign the following probability of failure value for each strength.

$$P = \frac{i}{n+1},$$

where
$i = 1, 2, 3, \ldots, n$
$n =$ total number of specimens tested

i	σ	P
1	46.15	1/23 = 0.0435
2	47.14	2/23 = 0.0869
3	47.94	3/23 = 0.1304
...	...	...
...	...	...
21	72.84	21/23 = 0.9130
22	72.95	22/23 = 0.9565

Step 2: Plot P vs. tensile strength σ to obtain the Weibull distribution plot (see the following figure).

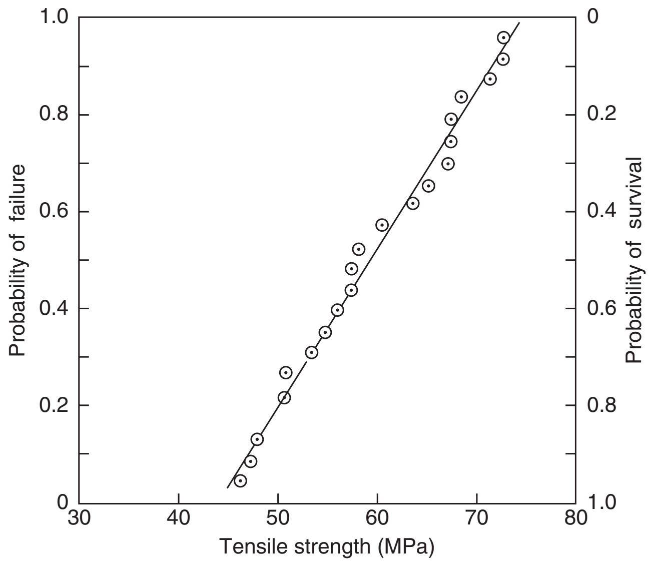

Step 3: Calculate $Y_P = \ln\{\ln[1/(1-P)]\}$ for each strength value, and plot Y_P vs. $\ln \sigma$. Use a linear least-squares method to fit a straight line to the data. The slope of this line is equal to α, and its intersection with the $\ln \sigma$ axis is equal to $\ln \sigma_0$. In our example, $\alpha = 7.62$ and $\ln \sigma_0 = 4.13$, which gives $\sigma_0 = 62.1$ MPa.

4.1.1.2 Unidirectional Laminates

For unidirectional polymer matrix laminates containing fibers parallel to the tensile loading direction (i.e., $\theta = 0°$), the tensile stress–strain curve is linear up to the point of failure (Figure 4.4). These specimens fail by tensile rupture of fibers, which is followed or accompanied by longitudinal splitting (debonding along the fiber–matrix interface) parallel to the fibers. This gives a typical broom-type appearance in the failed area of 0° specimens (Figure 4.5a). For off-axis specimens with $0° < \theta < 90°$, the tensile stress–strain curves may exhibit nonlinearity. For 90° specimens in which the fibers are 90° to the tensile loading direction, tensile rupture of the matrix or the fiber–matrix interface causes the ultimate failure. For intermediate angles, failure may occur by a combination of fiber–matrix interfacial shear failure, matrix shear failure, and matrix tensile rupture. For many of these off-axis specimens (including 90°), matrix craze marks parallel to the fiber direction may appear throughout the gage length at low loads. Representative failure profiles for these specimens are shown in Figure 4.5b and c.

Both tensile strength and modulus for unidirectional specimens depend strongly on the fiber orientation angle θ (Figure 4.6). The maximum tensile strength and modulus are at $\theta = 0°$. With increasing fiber orientation angle, both tensile strength and modulus are reduced. The maximum reduction is observed near $\theta = 0°$ orientations.

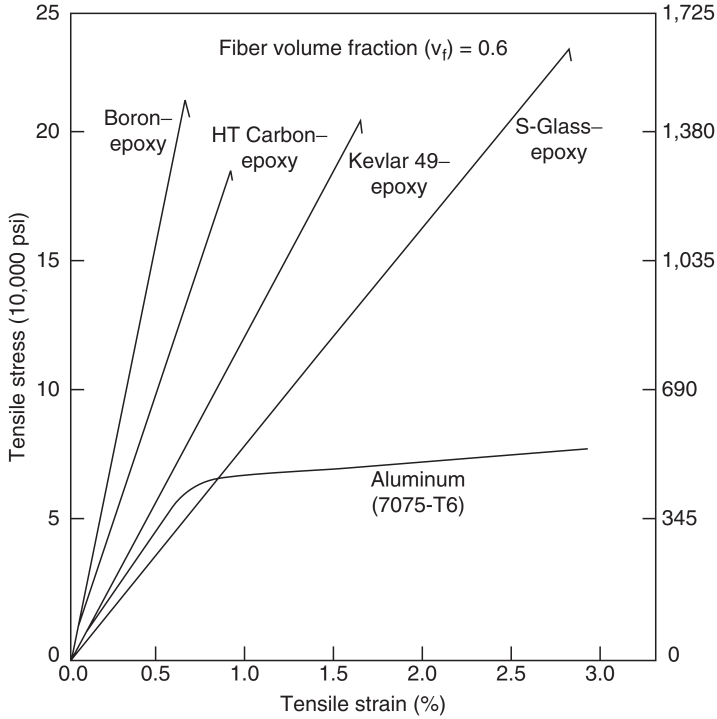

FIGURE 4.4 Tensile stress–strain curves for various 0° laminates.

4.1.1.3 Cross-Ply Laminates

The tensile stress–strain curve for a cross-ply $[0/90]_S$ laminate tested at $\theta = 0°$ direction is slightly nonlinear; however, it is commonly approximated as a bilinear curve (Figure 4.7). The point at which the two linear sections intersect is called the knee and represents the failure of 90° plies. Ultimate failure of the

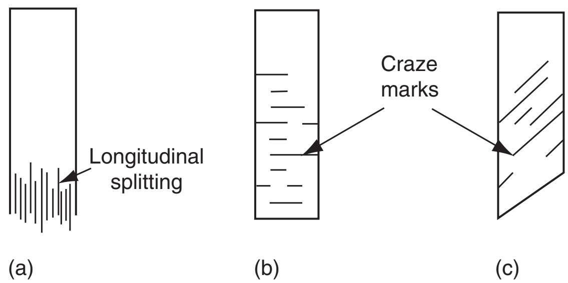

FIGURE 4.5 Schematic failure modes in unidirectional laminates: (a) $\theta = 0°$, (b) $\theta = 90°$, and (c) $0 < \theta < 90°$.

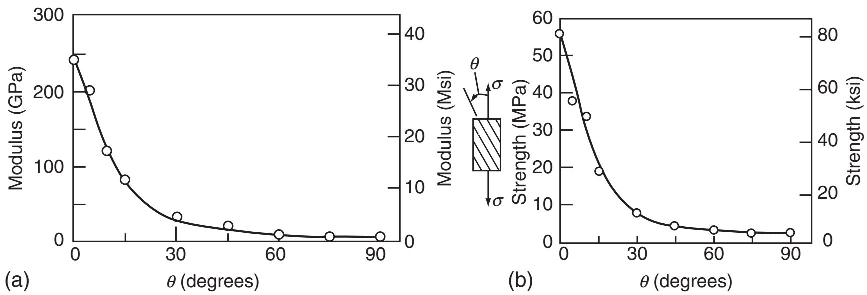

FIGURE 4.6 Variations of tensile modulus and tensile strength of a unidirectional carbon fiber–epoxy laminate with fiber orientation angle. (After Chamis, C.C. and Sinclair, J.H., Mechanical behavior and fracture characteristics of off-axis fiber composites, II—Theory and comparisons, NASA Technical Paper 1082, 1978.)

laminate occurs at the fracture strain of 0° plies. The change in slope of the stress–strain curve at the knee can be reasonably predicted by assuming that all 90° plies have failed at the knee and can no longer contribute to the laminate modulus.

Denoting the moduli of the 0° and 90° plies as E_{11} and E_{22}, respectively, the initial (primary) modulus of the cross-ply laminate can be approximated as

$$E = \frac{A_0}{A} E_{11} + \frac{A_{90}}{A} E_{22}, \tag{4.5}$$

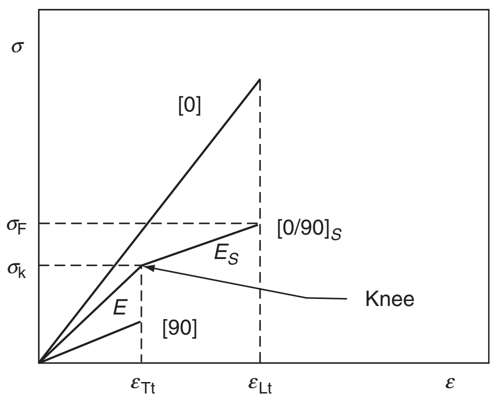

FIGURE 4.7 Schematic tensile stress–strain diagram for a $[0/90]_S$ cross-plied laminate tested at $\theta = 0°$ direction.

where

A_0 = net cross-sectional area of the 0° plies
A_{90} = net cross-sectional area of the 90° plies
A = $A_0 + A_{90}$

At the knee, the laminate strain is equal to the ultimate tensile strain ε_{TU} of the 90° plies. Therefore, the corresponding stress level in the laminate is

$$\sigma_k = E\varepsilon_{TU}, \tag{4.6}$$

where σ_k is the laminate stress at the knee.

If 90° plies are assumed to be completely ineffective after they fail, the secondary modulus (slope after the knee) E_s of the laminate can be approximated as

$$E_s = \frac{A_0}{A} E_{11}. \tag{4.7}$$

Failure of the laminate occurs at the ultimate tensile strain ε_{LU} of the 0° plies. Therefore, the laminate failure stress σ_F is

$$\sigma_F = \sigma_k + E_s(\varepsilon_{LU} - \varepsilon_{TU}). \tag{4.8}$$

Unloading of the cross-ply laminate from a stress level σ_L above the knee follows a path AB (Figure 4.8) and leaves a small residual strain in the laminate. Reloading takes place along the same path until the stress level σ_L is recovered. If the load is increased further, the slope before unloading is also

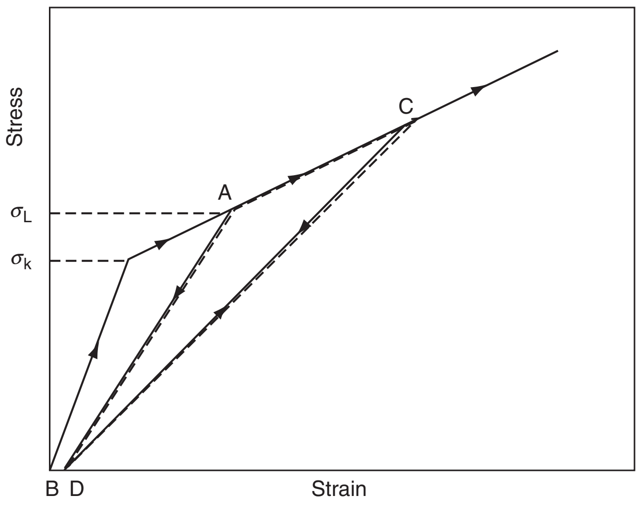

FIGURE 4.8 Unloading and reloading of a $[0/90]_S$ laminate.

recovered. Unloading from a higher stress level follows a path CD, which has a smaller slope than AB. The difference in slope between the two unloading paths AB and CD is evidence that the 90° plies fail in a progressive manner. Neglecting the small residual strains after unloading, Hahn and Tsai [6] predicted the elastic modulus E_D of the damaged laminate as

$$E_D = \frac{E}{1 + [(AE/A_0E_{11}) - 1](1 - \sigma_k/\sigma_L)}. \tag{4.9}$$

4.1.1.4 Multidirectional Laminates

Tensile stress–strain curves for laminates containing different fiber orientations in different laminas are in general nonlinear. A few examples are shown in Figure 4.9. For the purposes of analysis, these curves are approximated by a number of linear portions that have different slopes. When these linear portions are extended, a number of knees, similar to that observed in a cross-ply laminate, can be identified. The first knee in these diagrams is called the first ply failure (FPF) point. Many laminates retain a significant load-carrying capacity beyond the FPF point, but for some laminates with high notch sensitivity, failure occurs just after FPF (Table 4.2). Furthermore, cracks appearing at the FPF may increase the possibility of environmental damage (such as moisture pickup) as well as fatigue failure. For all these reasons, the FPF point has special importance in many laminate designs.

Angle-ply laminates containing [$\pm\theta$] layups exhibit two kinds of stress–strain nonlinearity (Figure 4.10). At values of θ closer to 0°, a stiffening effect

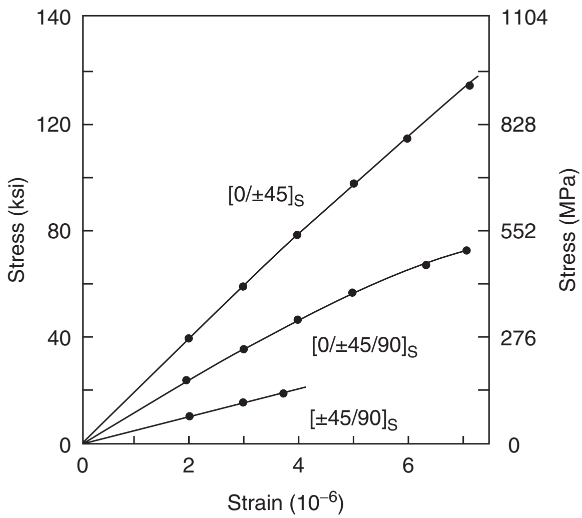

FIGURE 4.9 Typical tensile stress–strain diagrams for multidirectional laminates.

TABLE 4.2
Tensile Strengths and First-Ply Failure (FPF) Stresses in High-Strength Carbon–Epoxy Symmetric Laminates[a]

Laminate	UTS, MPa (ksi)		Estimated FPF Stress, MPa (ksi)		Tensile Modulus, GPa (Msi)	Initial Tensile Strain (%)
	Resin 1	Resin 2	Resin 1	Resin 2		
$[0]_S$	1378 (200)	1378 (200)	—	—	151.6 (22)	0.3
$[90]_S$	41.3 (6)	82.7 (12)	—	—	8.96 (1.3)	0.5–0.9
$[\pm 45]_S$	137.8 (20)	89.6 (13)	89.6 (13)	89.6 (13)	17.2 (2.5)	1.5–4.5
$[0/90]_S$	447.8 (65)	757.9 (110)	413.4 (60)	689 (100)	82.7 (12)	0.5–0.9
$[0_2/\pm 45]_S$	599.4 (87)	689 (110)	592.5 (86)	689 (100)	82.7 (12)	0.8–0.9
$[0/\pm 60]_S$	461.6 (67)	551.2 (80)	323.8 (47)	378.9 (55)	62 (9)	0.8–0.9
$[0/90/\pm 45]_S$	385.8 (56)	413.4 (60)	275.6 (40)	413.4 (60)	55.1 (8)	0.8–0.9

Source: Adapted from Freeman, W.T. and Kuebeler, G.C., *Composite Materials: Testing and Design* (*Third Conference*), *ASTM STP*, 546, 435, 1974.

[a] Resin 2 is more flexible than resin 1 and has a higher strain-to-failure.

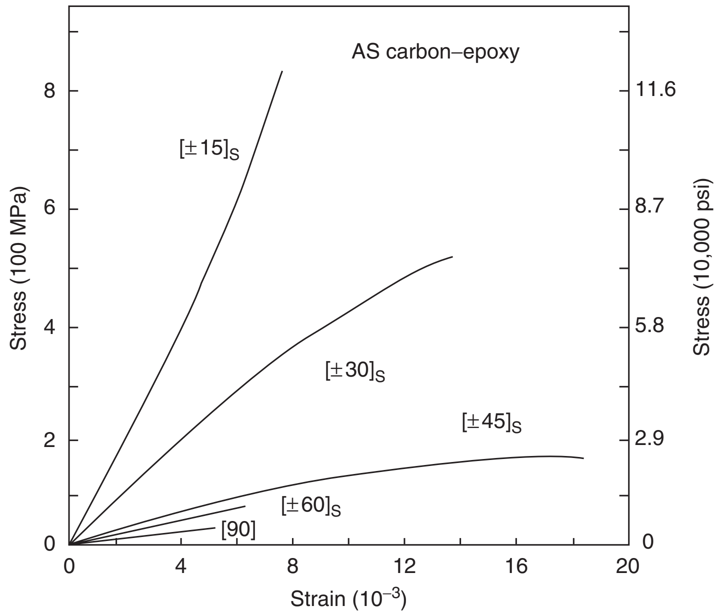

FIGURE 4.10 Typical tensile stress–strain diagrams for angle-ply laminates. (Adapted from Lagace, P.A., *AIAA J.*, 23, 1583, 1985.)

is observed so that the modulus increases with increasing load. At larger values of θ, a softening effect is observed so that the modulus decreases with the increasing load [7]. The stiffening effect is attributed to the longitudinal tensile stresses in various plies, whereas the softening effect is attributed to the shear stresses. Stiffening laminates do not exhibit residual strain on unloading. Softening laminates, on the other hand, exhibit a residual strain on unloading and a hysteresis loop on reloading. However, the slope of the stress–strain curve during reloading does not change from the slope of the original stress–strain curve.

The tensile failure mode and the tensile strength of a multidirectional laminate containing laminas of different fiber orientations depend strongly on the lamina stacking sequence. An example of the stacking sequence effect is observed in the development of cracks in $[0/\pm45/90]_S$ and $[0/90/\pm45]_S$ laminates (Figure 4.11). In both laminates, intralaminar transverse cracks (parallel to fibers) appear in the 90° plies. However, they are arrested at the

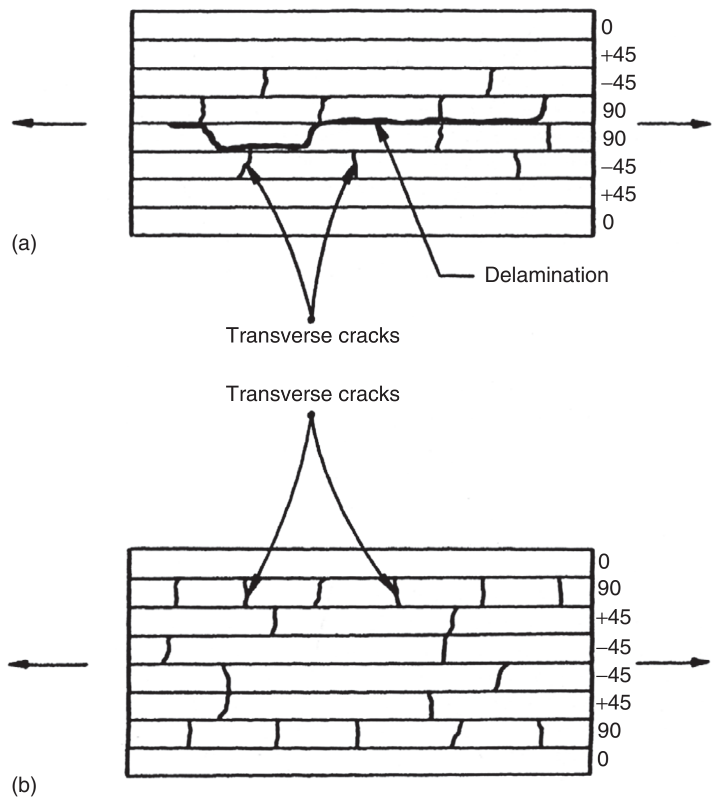

FIGURE 4.11 Damage development in (a) $[0/\pm45/90]_S$ and (b) $[0/90/\pm45]_S$ laminates subjected to static tension loads in the 0° direction.

lamina interfaces and do not immediately propagate into the adjacent plies. The number of transverse cracks in the 90° plies increases until uniformly spaced cracks are formed throughout the specimen length [8]; however, these transverse cracks are more closely spaced in $[0/90/\pm45]_S$ laminates than $[0/\pm45/90]_S$ laminates. Increasing the tensile load also creates a few intralaminar cracks parallel to the fiber directions in both $-45°$ and $+45°$ plies. Apart from these intralaminar crack patterns, subsequent failure modes in these two apparently similar laminates are distinctly different. In $[0/\pm45/90]_S$ laminates, longitudinal interlaminar cracks grow between the 90° plies, which join together to form continuous edge delaminations with occasional jogging into the $90/-45$ interfaces. With increasing load, the edge delamination extends toward the center of the specimen; however, the specimen fails by the rupture of 0° fibers before the entire width is delaminated. In contrast to the $[0/\pm45/90]_S$ laminate, there is no edge delamination in the $[0/90/\pm45]_S$ laminate; instead, transverse cracks appear in both $+45°$ and $-45°$ plies before the laminate failure. The difference in edge delamination behavior between the $[0/\pm45/90]_S$ and $[0/90/\pm45]_S$ laminates can be explained in terms of the interlaminar normal stress σ_{zz}, which is tensile in the former and compressive in the latter.

Table 4.3 presents the tensile test data and failure modes observed in several multidirectional carbon fiber–epoxy laminates. If the laminate contains 90° plies, failure begins with transverse microcracks appearing in these plies. With increasing stress level, the number of these transverse microcracks increases until a saturation number, called the characteristic damage state (CDS), is reached. Other types of damages that may follow transverse microcracking are delamination, longitudinal cracking, and fiber failure.

4.1.1.5 Woven Fabric Laminates

The principal advantage of using woven fabric laminates is that they provide properties that are more balanced in the 0° and 90° directions than unidirectional laminates. Although multilayered laminates can also be designed to produce balanced properties, the fabrication (layup) time for woven fabric laminates is less than that of a multilayered laminate. However, the tensile strength and modulus of a woven fabric laminate are, in general, lower than those of multilayered laminates. The principal reason for their lower tensile properties is the presence of fiber undulation in woven fabrics as the fiber yarns in the fill direction cross over and under the fiber yarns in the warp direction to create an interlocked structure. Under tensile loading, these crimped fibers tend to straighten out, which creates high stresses in the matrix. As a result, microcracks are formed in the matrix at relatively low loads. This is also evidenced by the appearance of one or more knees in the stress–strain diagrams of woven fabric laminates (Figure 4.12). Another factor to consider is that the fibers in woven fabrics are subjected to additional mechanical handling during the weaving process, which tends to reduce their tensile strength.

TABLE 4.3
Tensile Test Data and Failure Modes of Several Symmetric Carbon Fiber-Reinforced Epoxy Laminates

Laminate Type	Secant Modulus at Low Strain, GPa	Failure Stress, MPa	Failure Strain	Transverse Ply Strain Cracking	Failure Modes (in Sequence)
$[0_4/90]_S$	122	1620	0.0116	0.0065	Small transverse ply cracks in 90° plies, transverse cracks growing in number as well as in length up to 0° plies, delamination at 0/90 interfaces, 0° ply failure
$[0_4/90_2]_S$	109	1340	0.011	0.004	
$[0_4/90_4]_S$	93	1230	0.0114	0.0035	
$[0_4/90_8]_S$	72	930	0.0115	0.003	
$[\pm 45]_S$	17.3	126	0.017	—	Edge crack formation, edge cracks growing across the width parallel to fiber direction, delamination at the +45/−45 interfaces, single or multiple ply failure
$[+45_2/-45_2]_S$	19	135	0.0117	—	
$[+45_3/-45_3]_S$	14	89	0.01	—	
$[+45/-45_2/45]_S$	18.2	152	0.016	—	
$[(+45/-45)_2]_S$	17	125	0.014	—	
$[\pm 45/90_2/0_2]_S$	64.2	690	0.014	0.0028	Transverse microcracks in 90° plies, longitudinal or angled cracks in 90° plies in the first three laminates, a few edge cracks in 45° plies, delamination (45/90, 0/90, ±45, and 45/0 interfaces in ascending order of threshold strain), longitudinal ply failure
$[\pm 45/0_2/90_2]_S$	61.2	630	0.014	0.0022	
$[0_2/\pm 45/90_2]_S$	56.4	640	0.012	0.0016	
$[0_2/90_2/\pm 45]_S$	59.1	670	0.012	0.0035	

Source: Adapted from Harrison, R.P. and Bader, M.G., *Fibre Sci. Technol.*, 18, 163, 1983.

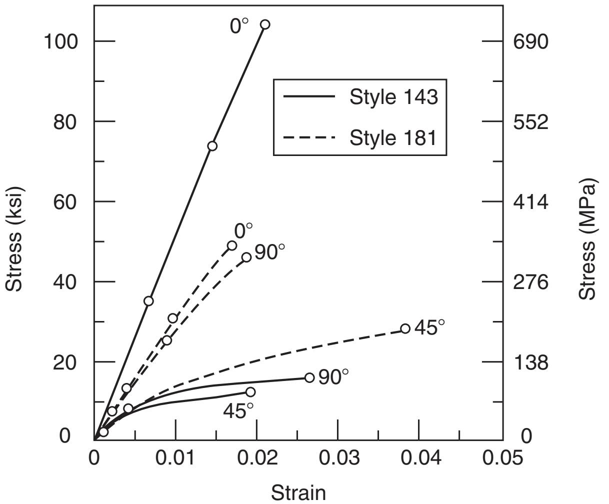

FIGURE 4.12 Stress–strain diagrams of woven glass fabric-epoxy laminates with fabric style 143 (crowfoot weave with 49 × 30 ends) and fabric style 181 (8-harness satin weave with 57 × 54 ends).

Tensile properties of woven fabric laminates can be controlled by varying the yarn characteristics and the fabric style (see Appendix A.1). The yarn characteristics include the number of fiber ends, amount of twist in the yarn, and relative number of yarns in the warp and fill directions. The effect of fiber ends can be seen in Table 4.4 when the differences in the 0° and 90° tensile properties of the parallel laminates with 181 fabric style and 143 fabric style are compared. The difference in the tensile properties of each of these laminates in the 0° and 90° directions reflects the difference in the number of fiber ends in the warp and fill

TABLE 4.4
Tensile Properties of Glass Fabric Laminates

	Tensile Strength, MPa Direction of Testing			Tensile Modulus, GPa Direction of Testing		
Fabric Style[a]	**0° (Warp)**	**90° (Fill)**	**45°**	**0° (Warp)**	**90° (Fill)**	**45°**
181 Parallel lamination	310.4	287.7	182.8	21.4	20.34	15.5
143 Parallel lamination	293.1	34.5	31.0	16.5	6.9	5.5
143 Cross lamination	327.6	327.6	110.3	23.4	23.4	12.2

Source: Adapted from Broutman, L.J., in *Modern Composite Materials*, L.J. Broutman and R.H. Krock, eds., Addison-Wesley, Reading, MA, 1967.

[a] Style 181: 8-harness satin weave, 57 (warp) × 54 (fill) ends, Style 143: Crowfoot weave, 49 (warp) × 30 (fill) ends.

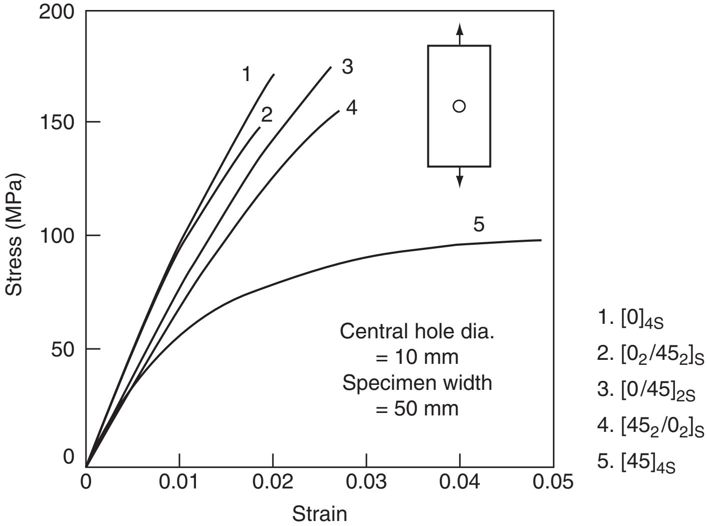

FIGURE 4.13 Effect of stacking sequence on the tensile properties of woven fabric laminates with a central hole. (Adapted from Naik, N.K., Shembekar, P.S., and Verma, M.K., *J. Compos. Mater.*, 24, 838, 1990.)

directions, which is smaller for the 181 fabric style than for the 143 fabric style. Tensile properties of fabric-reinforced laminates can also be controlled by changing the lamination pattern (see, e.g., parallel lamination vs. cross lamination of the laminates with 143 fabric style in Table 4.4) and stacking sequence (Figure 4.13).

4.1.1.6 Sheet-Molding Compounds

Figure 4.14 shows the typical tensile stress–strain diagram for a random fiber SMC (SMC-R) composite containing randomly oriented chopped fibers in a $CaCO_3$-filled polyester matrix. The knee in this diagram corresponds to the development of craze marks in the specimen [9]. At higher loads, the density of craze marks increases until failure occurs by tensile cracking in the matrix and fiber pullout. Both tensile strength and tensile modulus increase with fiber volume fraction. The stress at the knee is nearly independent of fiber volume fractions >20%. Except for very flexible matrices (with high elongations at failure), the strain at the knee is nearly equal to the matrix failure strain. In general, SMC-R composites exhibit isotropic properties in the plane of the laminate; however, they are capable of exhibiting large scatter in strength values from specimen to specimen within a batch or between batches. The variation in strength can be attributed to the manufacturing process for SMC-R composites. They are compression-molded instead of the carefully controlled hand layup technique used for many continuous fiber laminates. A discussion of process-induced defects in compression-molded composites is presented in Chapter 5.

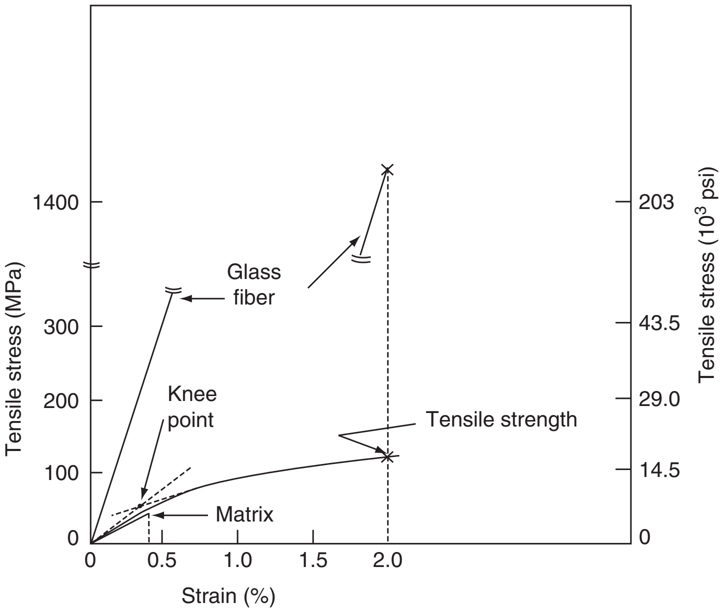

FIGURE 4.14 Tensile stress–strain diagram of an SMC-R laminate. (After Watanabe, T. and Yasuda, M., *Composites*, 13, 54, 1982.)

Tensile stress–strain diagrams for SMC composites containing both continuous and randomly oriented fibers (SMC-CR and XMC) are shown in Figure 4.15. As in the case of SMC-R composites, these stress–strain diagrams are also bilinear. Unlike SMC-R composites, the tensile strength and modulus of SMC-CR and XMC composites depend strongly on the fiber orientation angle of continuous fibers relative to the tensile loading axis. Although the longitudinal tensile strength and modulus of SMC-CR and XMC are considerably higher than those of SMC-R containing equivalent fiber volume fractions, they decrease rapidly to low values as the fiber orientation angle is increased (Figure 4.16). The macroscopic failure mode varies from fiber failure and longitudinal splitting at $\theta = 0°$ to matrix tensile cracking at $\theta = 90°$. For other orientation angles, a combination of fiber–matrix interfacial shear failure and matrix tensile cracking is observed.

4.1.1.7 Interply Hybrid Laminates

Interply hybrid laminates are made of separate layers of low-elongation (LE) fibers, such as high-modulus carbon fibers, and high-elongation (HE) fibers, such as E-glass or Kevlar 49, both in a common matrix. When tested in tension, the interply hybrid laminate exhibits a much higher ultimate strain at failure than the LE fiber composites (Figure 4.17). The strain at which the LE fibers

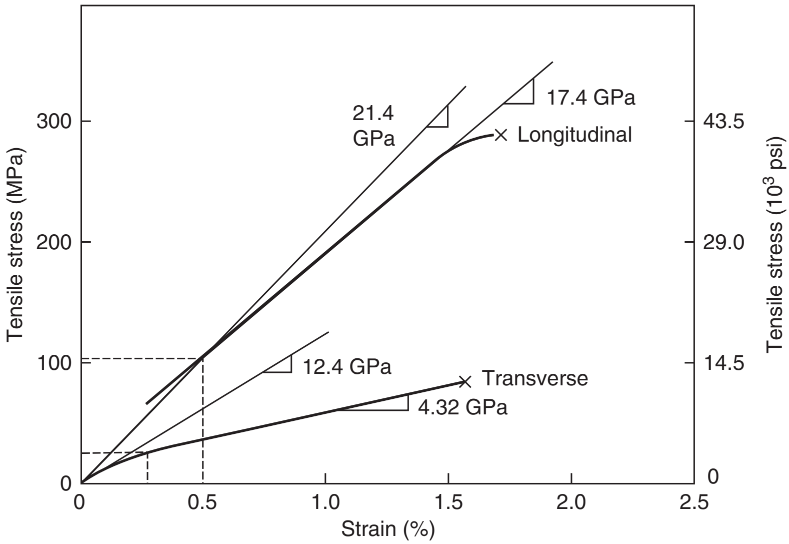

FIGURE 4.15 Tensile stress–strain diagrams for an SMC-C20R30 laminate in the longitudinal (0°) and transverse (90°) directions. (After Riegner, D.A. and Sanders, B.A., A characterization study of automotive continuous and random glass fiber composites, *Proceedings National Technical Conference*, Society of Plastics Engineers, November 1979.)

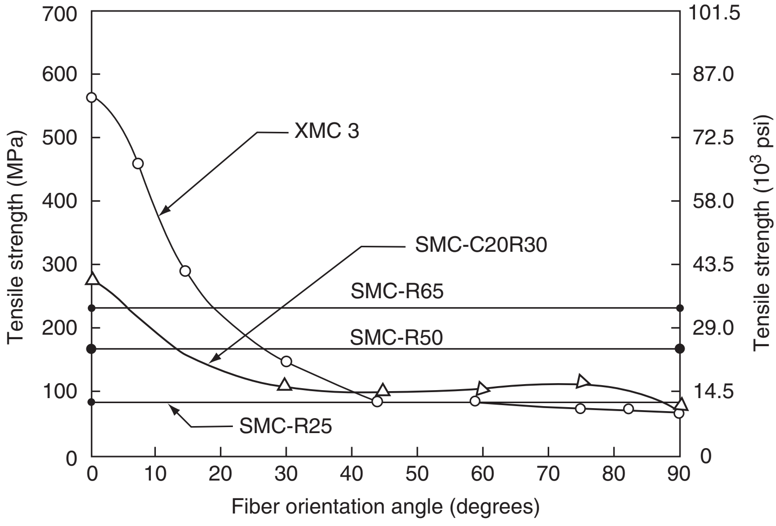

FIGURE 4.16 Variation of tensile strength of various SMC laminates with fiber orientation angle. (After Riegner, D.A. and Sanders, B.A., A characterization study of automotive continuous and random glass fiber composites, *Proceedings National Technical Conference*, Society of Plastics Engineers, November 1979.)

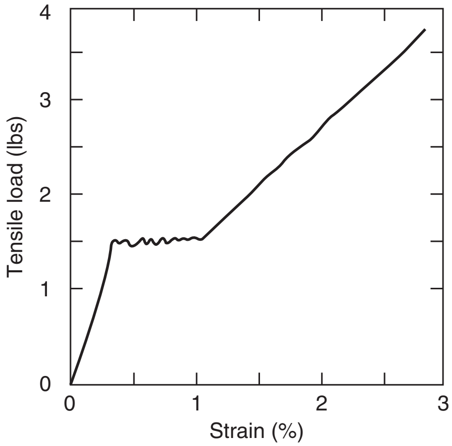

FIGURE 4.17 Tensile stress–strain diagram for a GY-70 carbon/S glass–epoxy interply hybrid laminate. (After Aveston, J. and Kelly, A., *Phil. Trans. R. Soc. Lond., A*, 294, 519, 1980.)

in the hybrid begin to fail is either greater than or equal to the ultimate tensile strain of the LE fibers. Furthermore, instead of failing catastrophically, the LE fibers now fail in a controlled manner, giving rise to a step or smooth inflection in the tensile stress–strain diagram. During this period, multiple cracks are observed in the LE fiber layers [10].

The ultimate strength of interply hybrid laminates is lower than the tensile strengths of either the LE or the HE fiber composites (Figure 4.18). Note that

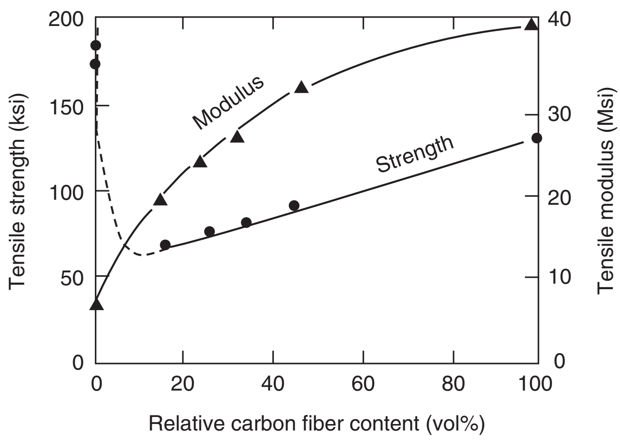

FIGURE 4.18 Variations of tensile strength and modulus of a carbon/glass–epoxy interply hybrid laminate with carbon fiber content. (After Kalnin, L.E., *Composite Materials: Testing and Design* (*Second Conference*), *ASTM STP*, 497, 551, 1972.)

the ultimate strain of interply hybrid laminates is also lower than that of the HE fiber composite. The tensile modulus of the interply hybrid laminate falls between the tensile modulus values of the LE and HE fiber composites. Thus, in comparison to the LE fiber composite, the advantage of an interply hybrid laminate subjected to tensile loading is the enhanced strain-to-failure. However, this enhancement of strain, referred to as the hybrid effect, is achieved at the sacrifice of tensile strength and tensile modulus.

The strength variation of hybrid laminates as a function of LE fiber content was explained by Manders and Bader [11]. Their explanation is demonstrated in Figure 4.19, where points A and D represent the tensile strengths of an all-HE fiber composite and an all-LE fiber composite, respectively. If each type of fiber is assumed to have its unique failure strain, the first failure event in the interply hybrid composite will occur when the average tensile strain in it exceeds the failure strain of the LE fibers. The line BD represents the stress in the interply hybrid composite at which failure of the LE fibers occurs. The line AE represents the stress in the interply hybrid composite assuming that the LE fibers carry no load. Thus, if the LE fiber content is less than v_c, the ultimate tensile strength of the interply hybrid laminate is controlled by the HE fibers. Even though the LE fibers have failed at stress levels given by the line BC, the HE fibers continue to sustain increasing load up to the level given by the line AC. For LE fiber contents greater than v_c, the HE fibers fail almost immediately after the failure of the LE fibers. Thus, the line ACD represents the tensile strength of the interply hybrid laminate. For comparison, the rule of mixture prediction, given by the line AD, is also shown in Figure 4.19.

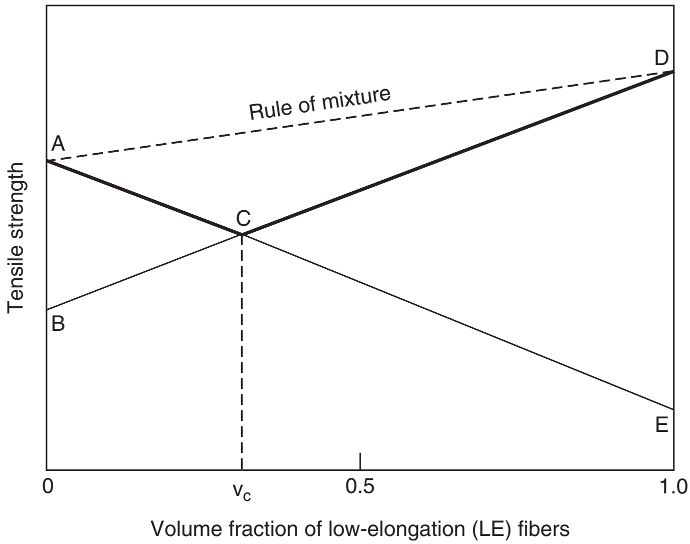

FIGURE 4.19 Model for tensile strength variation in interply hybrid laminates.

4.1.2 Compressive Properties

Compressive properties of thin composite laminates are difficult to measure owing to sidewise buckling of specimens. A number of test methods and specimen designs have been developed to overcome the buckling problem [12]. Three of these test methods are described as follows.

Celanese test: This was the first ASTM standard test developed for testing fiber-reinforced composites in compression; however, because of its several deficiencies, it is no longer a standard test. It employs a straight-sided specimen with tabs bonded at its ends and 10° tapered collet-type grips that fit into sleeves with a matching inner taper (Figure 4.20). An outer cylindrical shell is used for ease of assembly and alignment. As the compressive load is applied at

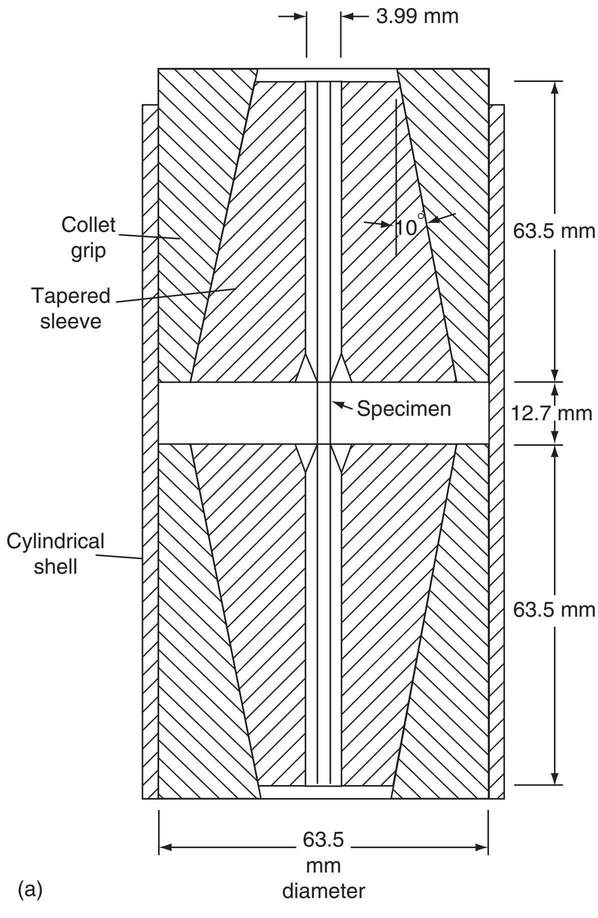

FIGURE 4.20 (a) Celanese test specimen and fixture for compression testing.

(continued)

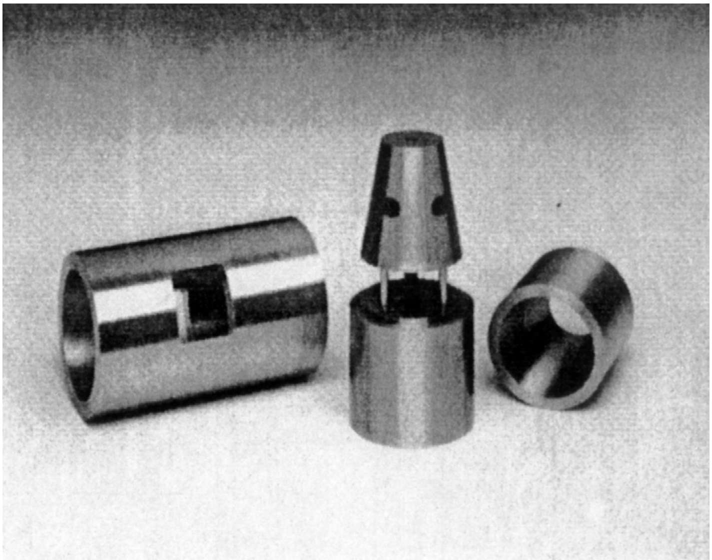

(b)

FIGURE 4.20 (continued) (b) Celanese compression test fixture. (Courtesy of MTS Systems Corporation. With permission.)

the ends of the tapered sleeves, the grip on the specimen tightens and the gage section of the specimen is compressed by the frictional forces transmitted through the end tabs. Strain gages are mounted in the gage section to measure longitudinal and transverse strain data from which compressive modulus and Poisson's ratio are determined.

IITRI test: The IITRI test was first developed at the Illinois Institute of Technology Research Institute and was later adopted as a standard compression test for fiber-reinforced composites (ASTM D3410). It is similar to the Celanese test, except it uses flat wedge grips instead of conical wedge grips (Figure 4.21). Flat wedge surfaces provide a better contact between the wedge and the collet than conical wedge surfaces and improve the axial alignment. Flat wedge grips can also accommodate variation in specimen thickness. The IITRI test fixture contains two parallel guide pins in its bottom half that slide into two roller bushings that are located in its top half. The guide pins help maintain good lateral alignment between the two halves during testing. The standard specimen length is 140 mm, out of which the middle 12.7 mm is unsupported and serves as the gage length. Either untabbed or tabbed specimens can be used; however, tabbing is preferred, since it prevents surface damage and end crushing of the specimen if the clamping force becomes too high.

Sandwich edgewise compression test: In this test, two straight-sided specimens are bonded to an aluminum honeycomb core that provides the necessary

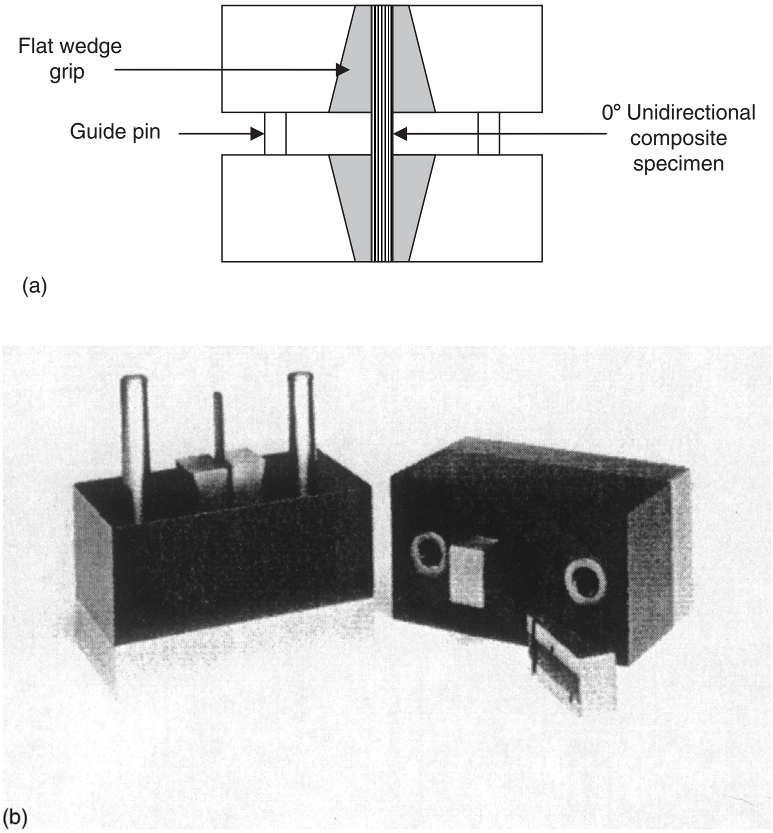

FIGURE 4.21 IITRI compression test fixture. (Courtesy of MTS Systems Corporation. With permission.)

support for lateral stability (Figure 4.22). Compressive load is applied through the end caps, which are used for supporting the specimen as well as preventing end crushing. The average compressive stress in the composite laminate is calculated assuming that the core does not carry any load. Table 4.5 shows representative compressive properties for carbon fiber–epoxy and boron fiber–epoxy laminates obtained in a sandwich edgewise compression test. The data in this table show that the compressive properties depend strongly on the fiber type as well as the laminate configuration.

Compressive test data on fiber-reinforced composites are limited. From the available data on 0° laminates, the following general observations can be made.

1. Unlike ductile metals, the compressive modulus of a 0° laminate is not equal to its tensile modulus.
2. Unlike tensile stress–strain curves, compressive stress–strain curves of 0° laminates may not be linear.

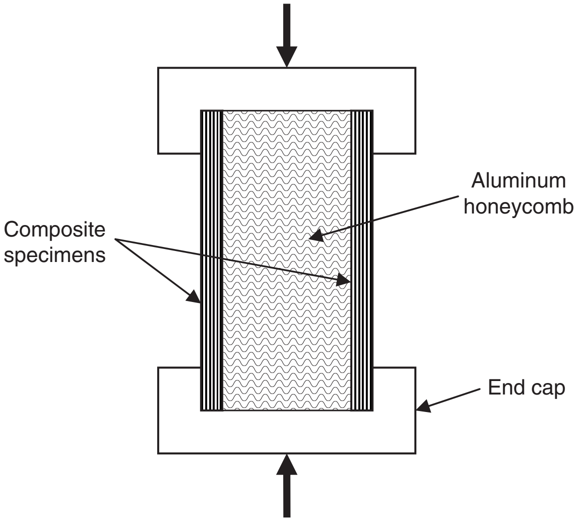

FIGURE 4.22 Sandwich edgewise compression testing specimen.

3. The longitudinal compressive strength of a 0° laminate depends on the fiber type, fiber volume fraction, matrix yield strength, fiber length–diameter ratio, fiber straightness, fiber alignment as well as fiber–matrix interfacial shear strength. The effects of some of these variables on the compressive properties of unidirectional fiber-reinforced polyester composites have been studied by Piggott and Harris and are described in Ref. [4].

TABLE 4.5
Compressive Properties of Carbon and Boron Fiber-Reinforced Epoxy Composites

	Carbon–Epoxy		Boron–Epoxy	
Laminate	Strength, MPa (ksi)	Modulus, GPa (Msi)	Strength, MPa (ksi)	Modulus, GPa (Msi)
[0]	1219.5 (177)	110.9 (16.1)	2101.4 (305)	215.6 (31.3)
[±15]	799.2 (116)	95.8 (13.9)	943.9 (137)	162.9 (23.65)
[±45]	259.7 (37.7)	15.6 (2.27)	235.6 (34.2)	17.4 (2.53)
[90]	194.3 (28.2)	13.1 (1.91)	211.5 (30.7)	20.5 (2.98)
[0/90]	778.6 (113)	60.6 (8.79)	1412.4 (205)	118.3 (17.17)
[0/±45/90]	642.8 (93.3)	46.4 (6.74)	1054.2 (153)	79.0 (11.47)

Source: Adapted from Weller, T., Experimental studies of graphite/epoxy and boron/epoxy angle ply laminates in compression, NASA Report No. NASA-CR-145233, September 1977.

4. Among the commercially used fibers, the compressive strength and modulus of Kevlar 49-reinforced composites are much lower than their tensile strength and modulus. Carbon and glass fiber-reinforced composites exhibit slightly lower compressive strength and modulus than their respective tensile values, and boron fiber-reinforced composites exhibit virtually no difference between the tensile and compressive properties.

4.1.3 Flexural Properties

Flexural properties, such as flexural strength and modulus, are determined by ASTM test method D790. In this test, a composite beam specimen of rectangular cross section is loaded in either a three-point bending mode (Figure 4.23a) or a four-point bending mode (Figure 4.23b). In either mode, a large span–thickness (L/h) ratio is recommended. We will consider only the three-point flexural test for our discussion.

The maximum fiber stress at failure on the tension side of a flexural specimen is considered the flexural strength of the material. Thus, using a homogeneous beam theory, the flexural strength in a three-point flexural test is given by

$$\sigma_{UF} = \frac{3P_{max}L}{2bh^2}, \tag{4.10}$$

where

P_{max} = maximum load at failure
b = specimen width
h = specimen thickness
L = specimen length between the two support points

Flexural modulus is calculated from the initial slope of the load–deflection curve:

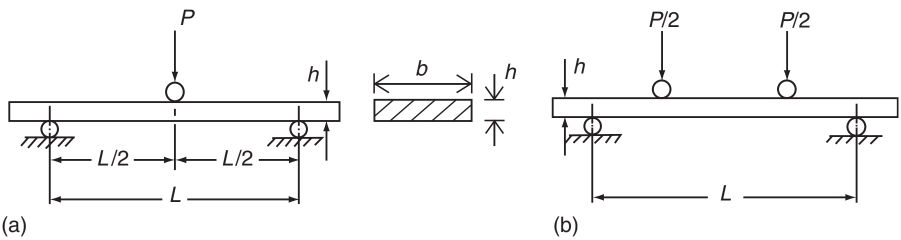

FIGURE 4.23 Flexural test arrangements in (a) three-point bending and (b) four-point bending modes.

$$E_F = \frac{mL^3}{4bh^3}, \quad (4.11)$$

where m is the initial slope of the load–deflection curve.

Three-point flexural tests have received wide acceptance in the composite material industry because the specimen preparation and fixtures are very simple. However, the following limitations of three-point flexural tests should be recognized.

1. The maximum fiber stress may not always occur at the outermost layer in a composite laminate. An example is shown in Figure 4.24. Thus, Equation 4.10 gives only an apparent strength value. For more accurate values, lamination theory should be employed.
2. In the three-point bending mode, both normal stress σ_{xx} and shear stress τ_{xz} are present throughout the beam span. If contributions from both stresses are taken into account, the total deflection at the midspan of the beam is

$$\Delta = \underbrace{\frac{PL^3}{4Ebh^3}}_{\text{normal}} + \underbrace{\frac{3PL}{10Gbh}}_{\text{shear}}$$

$$= \frac{PL^3}{4Ebh^3}\left[1 + \frac{12}{10}\left(\frac{E}{G}\right)\left(\frac{h}{L}\right)^2\right]. \quad (4.12)$$

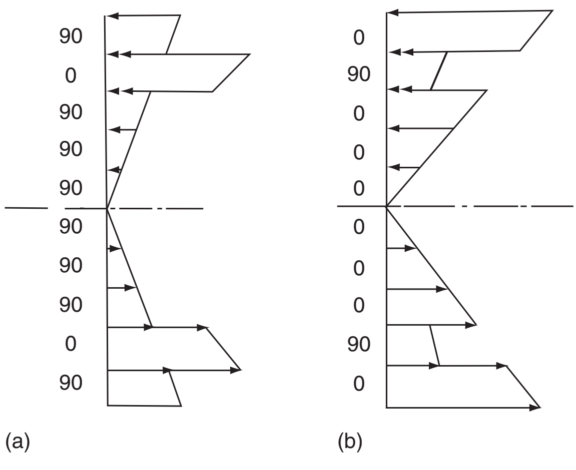

FIGURE 4.24 Normal stress (σ_{xx}) distributions in various layers of (a) [90/0/$(90)_6$/0/90] and (b) [0/90/$(0)_6$/90/0] laminates under flexural loading.

This equation shows that the shear deflection can be quite significant in a composite laminate, since the E/G ratio for fiber-reinforced composites is often quite large. The shear deflection can be reduced employing a high span–thickness (L/h) ratio for the beam. Based on data of Zweben et al. [13], L/h ratios of 60:1 are recommended for the determination of flexural modulus.

3. Owing to large deflection at high L/h ratios, significant end forces are developed at the supports. This in turn affects the flexural stresses in a beam. Unless a lower L/h ratio, say 16:1, is used, Equation 4.10 must be corrected for these end forces in the following way:

$$\sigma_{\max} = \frac{3P_{\max}L}{2bh^2}\left[1 + 6\left(\frac{\Delta}{L}\right)^2 - 4\left(\frac{h}{L}\right)\left(\frac{\Delta}{L}\right)\right], \tag{4.13}$$

where Δ is given by Equation 4.12.

4. Although the flexural strength value is based on the maximum tensile stress in the outer fiber, it does not reflect the true tensile strength of the material. The discrepancy arises owing to the difference in stress distributions in flexural and tensile loadings. Flexural loads create a nonuniform stress distribution along the length, but a tensile load creates a uniform stress distribution. Using a two-parameter Weibull distribution for both tensile strength and flexural strength variations, the ratio of the median flexural strength to the median tensile strength can be written as

$$\frac{\sigma_{\mathrm{UF}}}{\sigma_{\mathrm{UT}}} = \left[2(1+\alpha)^2 \frac{V_{\mathrm{T}}}{V_{\mathrm{F}}}\right]^{1/\alpha}, \tag{4.14}$$

where

α = shape parameter in the Weibull distribution function (assumed to be equal in both tests)

V_{T} = volume of material stressed in a tension test

V_{F} = volume of material stressed in a three-point flexural test

Assuming $V_{\mathrm{T}} = V_{\mathrm{F}}$ and using typical values of $\alpha = 15$ and 25 for 0° E-glass–epoxy and 0° carbon–epoxy laminates, respectively [12], Equation 4.14 shows that

$$\sigma_{\mathrm{UF}} = 1.52\sigma_{\mathrm{UT}} \text{ for } 0^\circ \text{ E-glass–epoxy laminates}$$
$$\sigma_{\mathrm{UF}} = 1.33\sigma_{\mathrm{UT}} \text{ for } 0^\circ \text{ carbon–epoxy laminates}$$

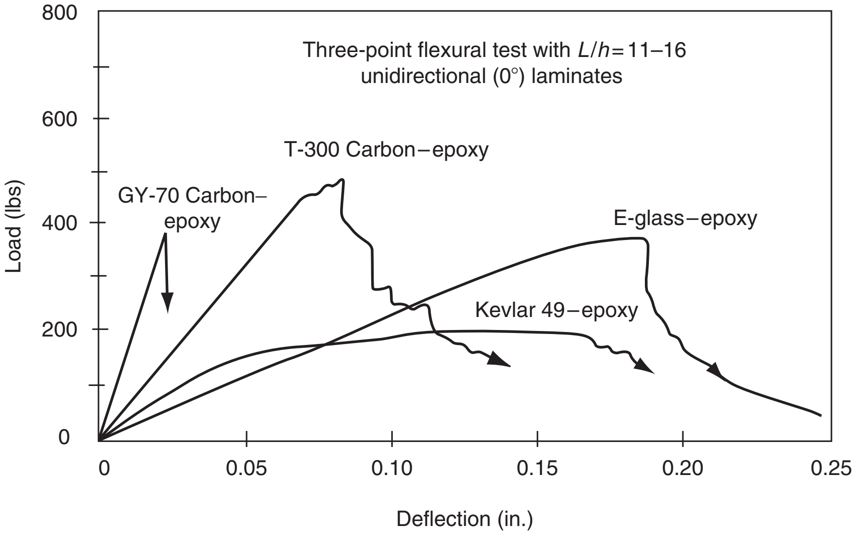

FIGURE 4.25 Load–deflection diagrams for various 0° unidirectional laminates in three-point flexural tests.

Thus, the three-point flexural strength of a composite laminate can be significantly higher than its tensile strength. The experimental data presented by Bullock [14] as well as Whitney and Knight [15] verify this observation.

Figure 4.25 shows the flexural load-deflection diagrams for four unidirectional 0° laminates. The materials of construction are an ultrahigh-modulus carbon (GY-70), a high-strength carbon (T-300), Kevlar 49, and E-glass fiber-reinforced epoxies. The difference in slope in their load–deflection diagrams reflects the difference in their respective fiber modulus. The GY-70 laminate exhibits a brittle behavior, but other laminates exhibit a progressive failure mode consisting of fiber failure, debonding (splitting), and delamination. The Kevlar 49 laminate has a highly nonlinear load–deflection curve due to compressive yielding. Fiber microbuckling damages are observed on the compression side of both E-glass and T-300 laminates. Since high contact stresses just under the loading point create such damage, it is recommended that a large loading nose radius be used.

The flexural modulus is a critical function of the lamina stacking sequence (Table 4.6), and therefore, it does not always correlate with the tensile modulus, which is less dependent on the stacking sequence. In angle-ply laminates, a bending moment creates both bending and twisting curvatures. Twisting curvature causes the opposite corners of a flexural specimen to lift off its supports. This also influences the measured flexural modulus. The twisting curvature is reduced with an increasing length–width (L/b) ratio and a decreasing degree of orthotropy (i.e., decreasing E_{11}/E_{22}).

TABLE 4.6
Tensile and Flexural Properties of Quasi-Isotropic Laminates

Laminate Configuration[b]	Tension Test: Strength, MPa (ksi)	Tension Test: Modulus, GPa (Msi)	Flexural Test[a]: Strength, MPa (ksi)	Flexural Test[a]: Modulus, GPa (Msi)
$[0/\pm 45/90]_S$	506.4 (73.5)	48.23 (7)	1219.5 (177)	68.9 (10)
$[90/\pm 45/0]_S$	405.8 (58.9)	45.47 (6.6)	141.2 (20.5)	18.6 (2.7)
$[45/0/-45/90]_S$	460.9 (66.9)	46.85 (6.8)	263.9 (38.3)	47.54 (6.9)

Source: Adapted from Whitney, J.M., Browning, C.E., and Mair, A., *Composite Materials: Testing and Design* (*Third Conference*), *ASTM STP*, 546, 30, 1974.

[a] Four-point flexural test with $L/h = 32$ and $L/b = 4.8$.
[b] Material: AS carbon fiber–epoxy composite, $v_f = 0.6$, eight plies.

4.1.4 In-Plane Shear Properties

A variety of test methods [16,17] have been used for measuring in-plane shear properties, such as the shear modulus G_{12} and the ultimate shear strength τ_{12U} of unidirectional fiber-reinforced composites. Three common in-plane shear test methods for measuring these two properties are described as follows.

±45 *Shear test*: The ±45 shear test (ASTM D3518) involves uniaxial tensile testing of a $[+45/-45]_{nS}$ symmetric laminate (Figure 4.26). The specimen dimensions, preparation, and test procedure are the same as those described in the tension test method ASTM D3039. A diagram of the shear stress τ_{12} vs. the shear strain γ_{12} is plotted using the following equations:

$$\begin{aligned} \tau_{12} &= \frac{1}{2}\sigma_{xx}, \\ \gamma_{12} &= \varepsilon_{xx} - \varepsilon_{yy}, \end{aligned} \tag{4.15}$$

where σ_{xx}, ε_{xx}, and ε_{yy} represent tensile stress, longitudinal strain, and transverse strain, respectively, in the $[\pm 45]_{nS}$ tensile specimen. A typical tensile stress–tensile strain response of a $[\pm 45]_S$ boron–epoxy laminate and the corresponding shear stress–shear strain diagram are shown in Figure 4.27.

10° *Off-axis test*: The 10° off-axis test [18] involves uniaxial tensile testing of a unidirectional laminate with fibers oriented at 10° from the tensile loading direction (Figure 4.28). The shear stress τ_{12} is calculated from the tensile stress σ_{xx} using the following expression:

$$\tau_{12} = \frac{1}{2}\sigma_{xx}\sin 2\theta\big|_{\theta=10^\circ} = 0.171\sigma_{xx}. \tag{4.16}$$

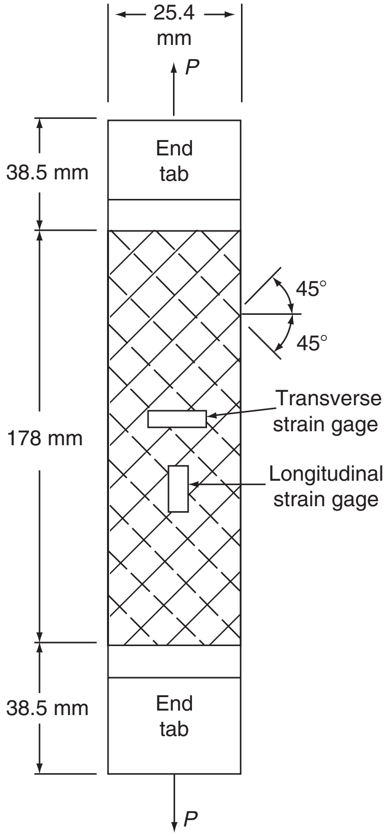

FIGURE 4.26 Test configuration for a $[\pm 45]_S$ shear test.

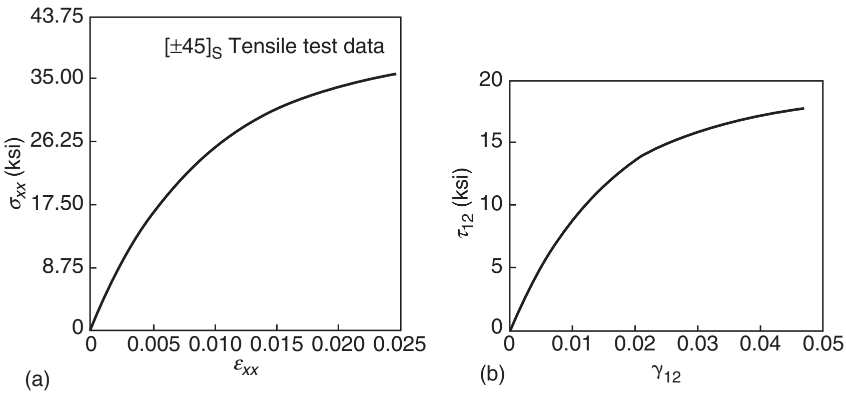

FIGURE 4.27 (a) Tensile stress–strain diagram for a $[\pm 45]_S$ boron–epoxy specimen and (b) the corresponding shear stress–shear strain diagram. (Adapted from the data in Rosen, B.M., *J. Compos. Mater.*, 6, 552, 1972.)

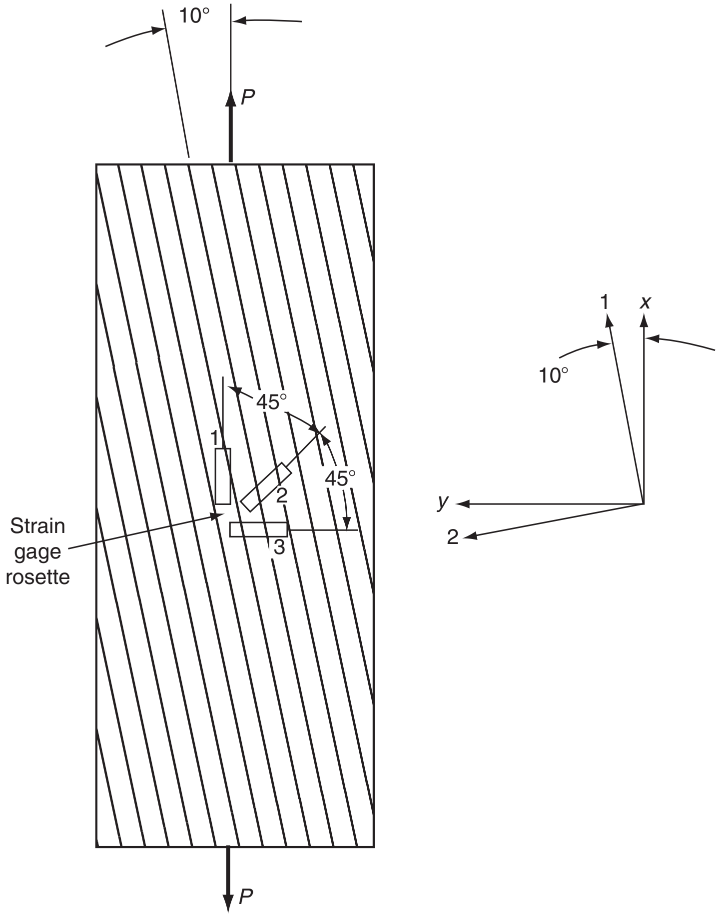

FIGURE 4.28 Test configuration for a 10° off-axis shear test.

Calculation of the shear strain γ_{12} requires measurements of three normal strains using either a rectangular strain gage rosette or a 60° Δ-strain gage rosette. If a rectangular strain gage rosette is used (Figure 4.28), the expression for shear strain γ_{12} is

$$\gamma_{12} = 0.5977\varepsilon_{g1} - 1.8794\varepsilon_{g2} + 1.2817\varepsilon_{g3}, \tag{4.17}$$

where ε_{g1}, ε_{g2}, and ε_{g3} are normal strains in gage 1, 2, and 3, respectively.

Iosipescu shear test: The Iosipescu shear test (ASTM D5379) was originally developed by Nicolai Iosipescu for shear testing of isotropic materials and was later adopted by Walrath and Adams [19] for determining the shear strength and modulus of fiber-reinforced composites. It uses a double V-notched test specimen, which is tested in a four-point bending fixture (Figure 4.29). A uniform transverse shear force is created in the gage section of the specimen, while the bending moment at the notch plane is zero. Various analyses have shown that except at the close vicinity of the notch roots, a state of pure

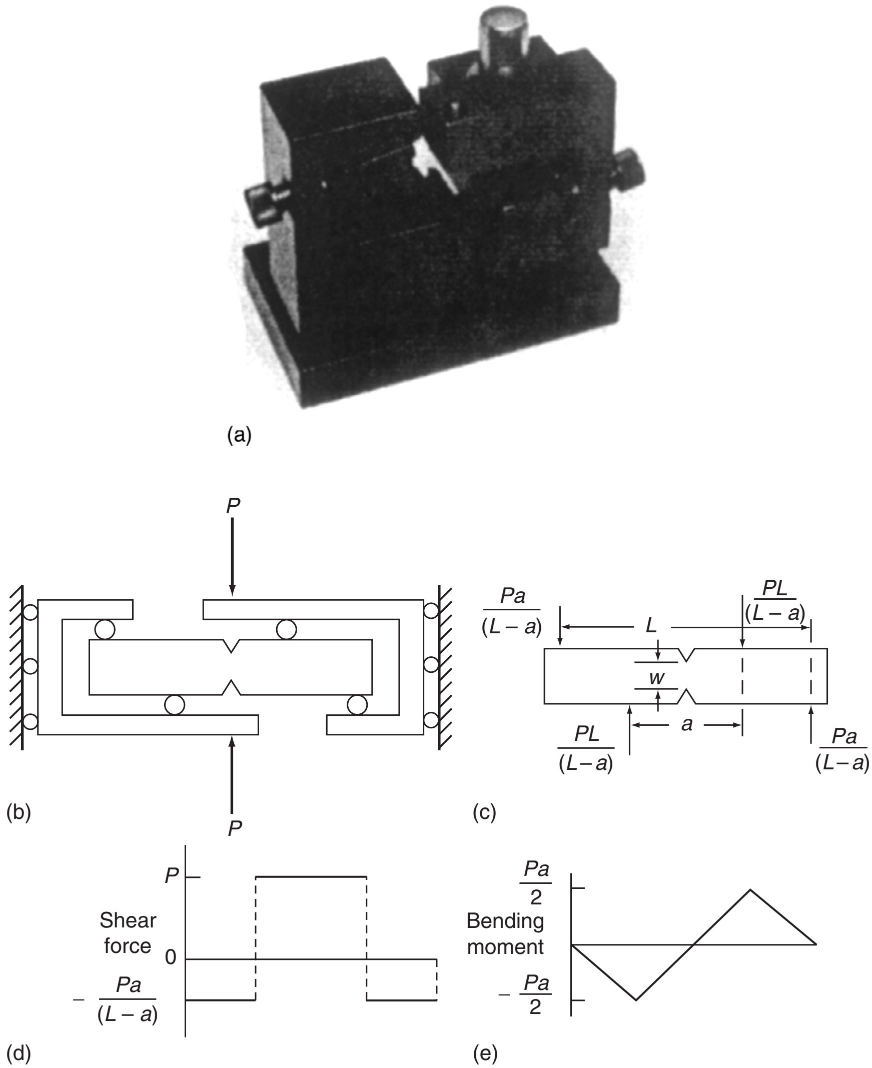

FIGURE 4.29 Iosipescu shear test: (a) test fixture (Courtesy of MTS System Corporation), (b) schematic representation, (c) free body, (d) shear force, and (e) bending moment distribution.

shear exists at the notch plane. The presence of notch creates a shear stress concentration at the notch root, which reduces with increasing notch angle and notch root radius, but increases with increasing orthotropy, that is, increasing (E_{11}/E_{22}). Typical Iosipescu specimens use a 90° notch angle, notch depth equal to 20% of the specimen width, and notch root radius of 1.3 mm.

The shear stress in an Iosipescu shear test is calculated as

$$\tau_{12} = \frac{P}{wh}, \tag{4.18}$$

where
P = applied load
w = distance between the notches
h = specimen thickness

A ±45° strain rosette, centered in the gage section of the specimen, is used to measure the shear strain at the midsection between the notches. The shear strain is given as

$$\gamma_{12} = \varepsilon_{+45^\circ} - \varepsilon_{-45^\circ}. \tag{4.19}$$

Based on a round robin test conducted by the ASTM [20], it is recommended that 0° specimens be used for measuring shear strength $\tau_{12\mathrm{U}}$ and shear modulus G_{12} of a continuous fiber-reinforced composite material. The 90° specimens show evidence of failure due to transverse tensile stresses that exist outside the notch plane. A schematic of the acceptable and unacceptable failure modes in 0° and 90° specimens is shown in Figure 4.30.

In-plane shear properties $\tau_{xy\mathrm{U}}$ and G_{xy} of a general laminate are commonly determined by either a two-rail or a three-rail edgewise shear test method (ASTM D4255). In a two-rail shear test, two pairs of steel rails are fastened along the long edges of a 76.2 mm wide × 152.4 mm long rectangular specimen, usually by three bolts on each side (Figure 4.31a). At the other two edges, the specimen remains free.

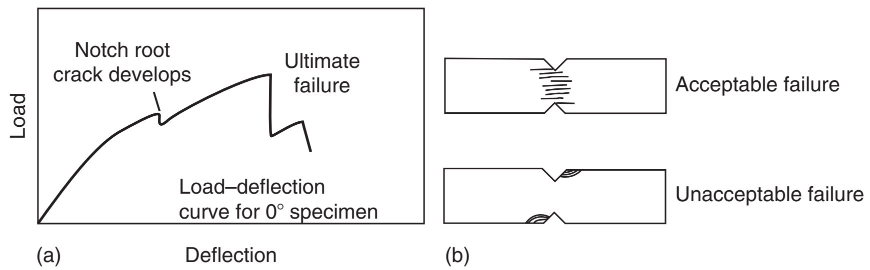

FIGURE 4.30 (a) Load-deflection diagram and (b) acceptable and unacceptable failure modes in an Iosipescu shear test.

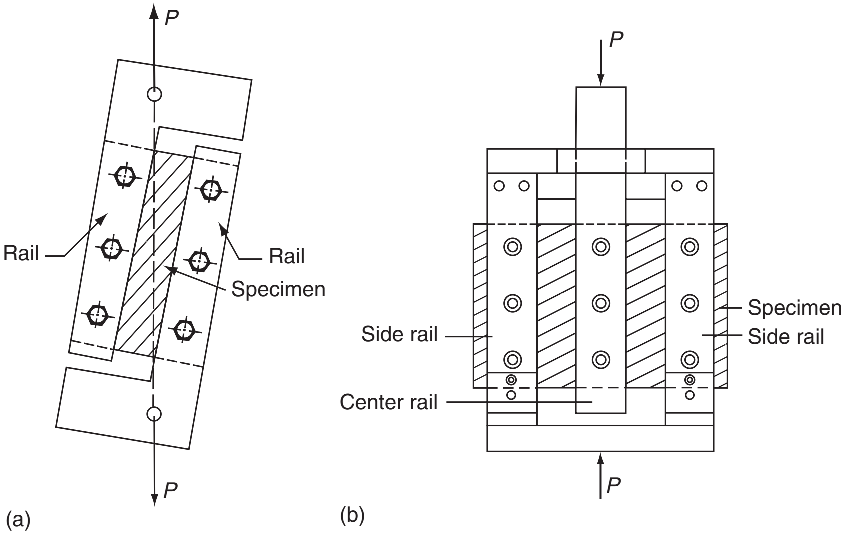

FIGURE 4.31 Test configuration for (a) two-rail and (b) three-rail shear tests.

A tensile load applied to the rails tends to displace one rail relative to the other, thus inducing an in-plane shear load on the test laminate. In a three-rail shear test, three pairs of steel rails are fastened to a 136 mm wide $\times$ 152 mm long rectangular specimen, two along its long edges, and one along its centerline (Figure 4.31b). A compressive load applied at the center rail creates an in-plane shear load in the specimen. The shear stress τ_{xy} is calculated from the applied load P as

$$\text{Two-rail:} \quad \tau_{xy} = \frac{P}{Lh},$$
$$\text{Three-rail:} \quad \tau_{xy} = \frac{P}{2Lh}, \tag{4.20}$$

where
  L is the specimen length
  h is the specimen thickness

The shear strain γ_{xy} is determined using a strain gage mounted in the center of the test section at 45° to the specimen's longitudinal axis. The shear strain γ_{xy} is calculated from the normal strain in the 45° direction:

$$\gamma_{xy} = 2\varepsilon_{45^\circ}. \tag{4.21}$$

In order to assure a uniform shear stress field at a short distance away from the free edges of a rail shear specimen [21], the length–width ratio must be greater than 10:1. A low effective Poisson's ratio for the laminate is also desirable, since

TABLE 4.7
In-Plane Shear Properties of [0] and $[\pm45]_S$ Laminates[a]

Material ($v_f = 60\%$)	Shear Strength, MPa (ksi)		Shear Modulus, GPa (Msi)	
	[0]	$[\pm45]_S$	[0]	$[\pm45]_S$
Boron–epoxy	62 (9)	530.5 (77)	4.82 (0.7)	54.4 (7.9)
Carbon–epoxy	62 (9)	454.7 (66)	4.48 (0.65)	37.9 (5.5)
Kevlar 49–epoxy	55.1 (8)	192.9 (28)	2.07 (0.3)	20.7 (3)
S-Glass–epoxy	55.1 (8)	241.1 (35)	5.51 (0.8)	15.1 (2.2)

[a] For comparison, the shear modulus of steel = 75.8 GPa (11 Msi) and that of aluminum alloys = 26.9 GPa (3.9 Msi).

the shear stress distribution in laminates of a high Poisson's ratio is irregular across the width. For shear properties of unidirectional laminates, either 0° or 90° orientation (fibers parallel or perpendicular to the rails) can be used. However, normal stress concentration near the free edges is transverse to the fibers in a 0° orientation and parallel to the fibers in the 90° orientation. Since normal stresses may cause premature failure in the 0° laminate, it is recommended that a 90° laminate be used for determining τ_{12U} and G_{12} [22].

Although the results from various in-plane shear tests do not always correlate, several general conclusions can be made:

1. The shear stress–strain response for fiber-reinforced composite materials is nonlinear.
2. Even though 0° laminates have superior tensile strength and modulus, their shear properties are poor.

The shear strength and modulus depend on the fiber orientation angle and laminate configuration. The highest shear modulus is obtained with $[\pm45]_S$ symmetric laminates (Table 4.7). The addition of 0° layers reduces both the shear modulus and the shear strength of $[\pm45]_S$ laminates.

4.1.5 Interlaminar Shear Strength

Interlaminar shear strength (ILSS) refers to the shear strength parallel to the plane of lamination. It is measured in a short-beam shear test in accordance with ASTM D2344. A flexural specimen of small span–depth (L/h) ratio is tested in three-point bending to produce a horizontal shear failure between the laminas. To explain the short-beam shear test, let us consider the following homogeneous beam equations:

$$\text{Maximum normal stress } \sigma_{xx} = \frac{3PL}{2bh^2} = \frac{3P}{2bh}\left(\frac{L}{h}\right), \tag{4.22a}$$

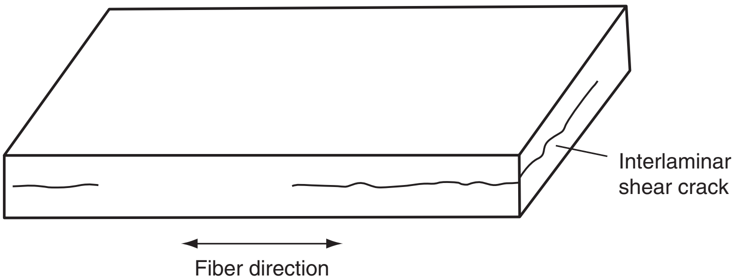

FIGURE 4.32 Interlaminar shear failure in a 0° laminate in a short-beam shear test.

$$\text{Maximum shear stress } \tau_{xz} = \frac{3P}{4bh}. \tag{4.22b}$$

From Equation 4.22, it can be seen that the maximum normal stress in the beam decreases with decreasing L/h ratio and the maximum shear stress (at the neutral axis) is not affected by the L/h ratio. Thus, for sufficiently small L/h ratios, the maximum shear stress in the beam will reach the ILSS of the material even though the maximum normal stress is still quite low. Thus, the beam will fail in the interlaminar shear mode by cracking along a horizontal plane between the laminas (Figure 4.32). The recommended L/h ratios for short-beam shear tests are between 4 and 5. However, testing a few specimens at various L/h ratios is usually needed before the proper L/h ratio for interlaminar shear failure is found. For very small L/h ratios a compressive failure may occur on the top surface of the specimen, whereas for large L/h ratios a tensile failure may occur at the bottom surface of the specimen [23]. Knowing the maximum load at failure, the ILSS is determined using Equation 4.22b.

Because of its simplicity, the short-beam shear test is widely accepted for material screening and quality control purposes [24]. However, it does not provide design data for the following reasons:

1. Equation 4.22b is based on homogeneous beam theory for long slender beams, which predicts a continuous parabolic shear stress distribution in the thickness direction (Figure 4.33). Such symmetrical shear stress distribution may not occur in a short-beam shear test [25]. Additionally, it may also contain discontinuities at lamina interfaces. Therefore, Equation 4.22b is only an approximate formula for ILSS.
2. In the homogeneous beam theory, maximum shear stress occurs at the neutral plane where normal stresses are zero. In short-beam shear tests of many laminates, maximum shear stress may occur in an area where other stresses may exist. As a result, a combination of failure modes, such as fiber rupture, microbuckling, and interlaminar shear cracking, are observed. Interlaminar shear failure may also not take place at the laminate midplane.

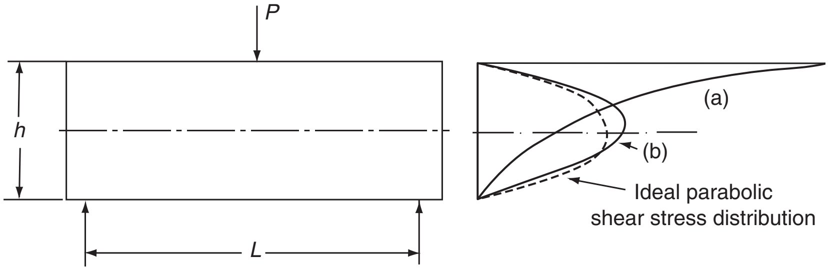

FIGURE 4.33 Shear stress distributions in a short-beam shear specimen: (a) near the support points and (b) near the midspan.

> For these reasons, it is often difficult to interpret the short-beam shear test data and compare the test results for various materials.

The ILSS, $\tau_{xz\mathrm{U}}$ is not the same as the in-plane shear strength, $\tau_{xy\mathrm{U}}$. Furthermore, the short-beam shear test should not be used to determine the shear modulus of a material.

Despite the limitations of the short-beam shear test, interlaminar shear failure is recognized as one of the critical failure modes in fiber-reinforced composite laminates. ILSS depends primarily on the matrix properties and fiber–matrix interfacial shear strengths rather than the fiber properties. The ILSS is improved by increasing the matrix tensile strength as well as the matrix volume fraction. Because of better adhesion with glass fibers, epoxies in general produce higher ILSS than vinyl ester and polyester resins in glass fiber-reinforced composites. The ILSS decreases, often linearly, with increasing void content. Fabrication defects, such as internal microcracks and dry strands, also reduce the ILSS.

4.2 FATIGUE PROPERTIES

The fatigue properties of a material represent its response to cyclic loading, which is a common occurrence in many applications. It is well recognized that the strength of a material is significantly reduced under cyclic loads. Metallic materials, which are ductile in nature under normal operating conditions, are known to fail in a brittle manner when they are subjected to repeated cyclic stresses (or strains). The cycle to failure depends on a number of variables, such as stress level, stress state, mode of cycling, process history, material composition, and environmental conditions.

Fatigue behavior of a material is usually characterized by an *S–N* diagram, which shows the relationship between the stress amplitude or maximum stress and number of cycles to failure on a semilogarithmic scale. This diagram is obtained by testing a number of specimens at various stress levels under sinusoidal loading conditions. For a majority of materials, the number of cycles to failure increases continually as the stress level is reduced. For low-carbon steel and a few other alloys, a fatigue limit or endurance limit is observed between 10^5 and 10^6 cycles. For low-carbon steels, the fatigue limit is $\cong$50% of its ultimate tensile strength. Below the fatigue limit, no fatigue failure occurs so that the material has essentially an infinite life. For many fiber-reinforced composites, a fatigue limit may not be observed; however, the slope of the *S–N* plot is markedly reduced at low stress levels. In these situations, it is common practice to specify the fatigue strength of the material at very high cycles, say, 10^6 or 10^7 cycles.

4.2.1 Fatigue Test Methods

The majority of fatigue tests on fiber-reinforced composite materials have been performed with uniaxial tension–tension cycling (Figure 4.34). Tension–compression and compression–compression cycling are not commonly used since failure by compressive buckling may occur in thin laminates. Completely reversed tension–compression cycling is achieved by flexural fatigue tests. In addition, a limited number of interlaminar shear fatigue and in-plane shear fatigue tests have also been performed.

The tension–tension fatigue cycling test procedure is described in ASTM D3479. It uses a straight-sided specimen with the same dimensions and end tabs as in static tension tests. At high cyclic frequencies, polymer matrix composites may generate appreciable heat due to internal damping, which is turn increases the specimen temperature. Since a frequency-induced temperature rise can affect the fatigue performance adversely, low cyclic frequencies (<10 Hz) are

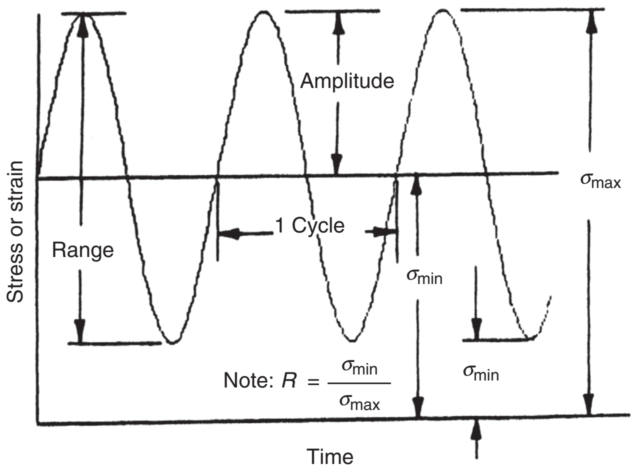

FIGURE 4.34 Stress vs. time diagram in a fatigue test.

preferred. Both stress-controlled and strain-controlled tests are performed. In a stress-controlled test, the specimen is cycled between specified maximum and minimum stresses so that a constant stress amplitude is maintained. In a strain-controlled test, the specimen is cycled between specified maximum and minimum strains so that a constant strain amplitude is maintained.

A unique feature of a fiber-reinforced composite material is that it exhibits a gradual softening or loss in stiffness due to the appearance of microscopic damages long before any visible damage occurs. As a result, the strain in the specimen increases in load-controlled tests, but the stress in the specimen decreases in strain-controlled tests (Figure 4.35). Microscopic damages also cause a loss in residual strength of the material. Instead of specimen separation,

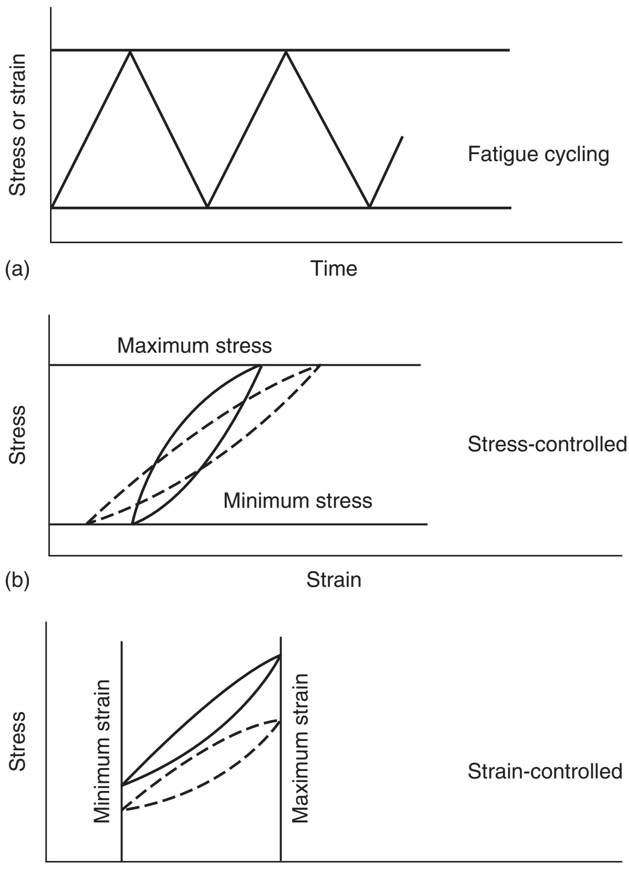

FIGURE 4.35 (a) Fatigue cycling in stress-controlled or strain-controlled fatigue tests. Differences in (b) stress-controlled test and (c) strain-controlled fatigue test of polymer matrix composites.

many fatigue tests are performed until the specimen stiffness or residual strength decreases to a predetermined level. Thus, cycles to failure may not always represent the specimen life at complete fracture.

Many investigators have attempted to describe the S–log N plot for various fiber-reinforced composites by a straight line:

$$S = \sigma_{\mathrm{U}}(m \log N + b), \tag{4.23}$$

where

S = maximum fatigue stress
N = number of cycles to failure
σ_{U} = average static strength
m, b = constants

Values of m and b for a few epoxy matrix composites are given in Table 4.8.

A power-law representation for the S–N plot is also used:

$$\frac{S}{\sigma_{\mathrm{U}}} N^d = c, \tag{4.24}$$

where c and d are constants. Similar expressions can be written for $\varepsilon-N$ plots obtained in strain-controlled fatigue tests.

The number of cycles to failure, also called the fatigue life, usually exhibits a significant degree of scatter. Following a two-parameter Weibull distribution, the probability of fatigue life exceeding L can be written as

$$F(L) = \exp\left[-\left(\frac{L}{L_0}\right)^{\alpha_{\mathrm{f}}}\right], \tag{4.25}$$

TABLE 4.8
Constants in *S–N* Representation of Composite Laminates

Material	Layup	R	Constants in Equation 4.23: m	b	References
E-glass–ductile epoxy	0°	0.1	−0.1573	1.3743	[26]
T-300 Carbon–ductile epoxy	0°	0.1	−0.0542	1.0420	[26]
E-glass–brittle epoxy	0°	0.1	−0.1110	1.0935	[26]
T-300 Carbon–brittle epoxy	0°	0.1	−0.0873	1.2103	[26]
E-glass–epoxy	$[0/\pm45/90]_{\mathrm{S}}$	0.1	−0.1201	1.1156	[27]
E-glass–epoxy	$[0/90]_{\mathrm{S}}$	0.05	−0.0815	0.934	[28]

Note: R represents the ratio of the minimum stress and the maximum stress in fatigue cycling.

where

α_f is the shape parameter in fatigue

L_0 is the location parameter for the fatigue life distribution (cycles)

Comparing the static strength data and fatigue life data of unidirectional 0° E-glass–epoxy, Hahn and Kim [29] proposed the following correlation between the static strength and fatigue data:

$$\frac{L}{L_0} = \left(\frac{S}{\sigma_U}\right)^{\alpha/\alpha_f}. \tag{4.26}$$

Equation 4.26 implies that the higher the static strength of a specimen, the longer would be its fatigue life.

4.2.2 Fatigue Performance

4.2.2.1 Tension–Tension Fatigue

Tension–tension fatigue tests on unidirectional 0° ultrahigh-modulus carbon fiber-reinforced thermoset polymers produce S–N curves that are almost horizontal and fall within the static scatter band (Figure 4.36). The fatigue effect is slightly greater for relatively lower modulus carbon fibers. Unidirectional 0° boron and Kevlar 49 fiber composites also exhibit exceptionally good fatigue strength in tension–tension loading (Figure 4.37). Other laminates, such as $[0/\pm45/90]_S$ carbon, $[0/90]_S$ carbon, $[0/\pm30]_S$ carbon, and $[0/\pm45]_S$ boron

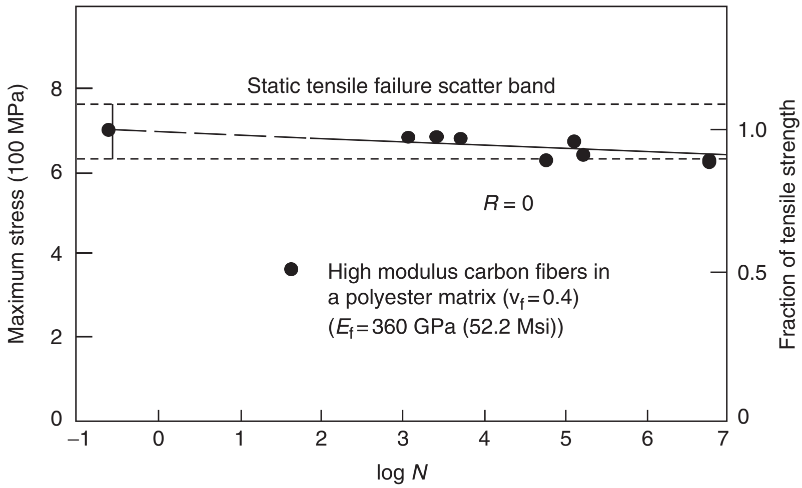

FIGURE 4.36 Tension–tension S–N diagram for a 0° ultrahigh-modulus carbon fiber–polyester composite. (After Owen, M.J. and Morris, S., *Carbon Fibres: Their Composites and Applications*, Plastics Institute, London, 1971.)

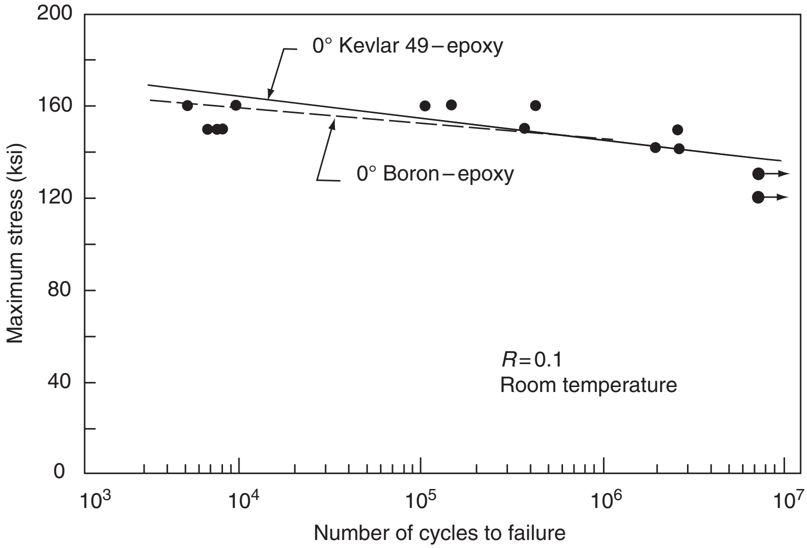

FIGURE 4.37 Tension–tension *S–N* diagram for a 0° boron and Kevlar 49 fiber–epoxy composites. (After Miner, L.H., Wolfe, R.A., and Zweben, C.H., *Composite Reliability, ASTM STP*, 580, 1975.)

(Figure 4.38), show very similar *S–N* diagrams, although the actual fatigue effect depends on the proportion of fibers aligned with the loading axis, stacking sequence, and mode of cycling. The effect of cycling mode is demonstrated in Figure 4.39, in which a tension–compression cycling ($R = -1.6$) produces a steeper *S–N* plot than the tension–tension cycling ($R = 0.1$) and the compression–compression cycling ($R = 10$) gives the lowest *S–N* plot.

The fatigue performances of both E- and S-glass fiber-reinforced composites are inferior to those of carbon, boron, and Kevlar 49 fiber-reinforced

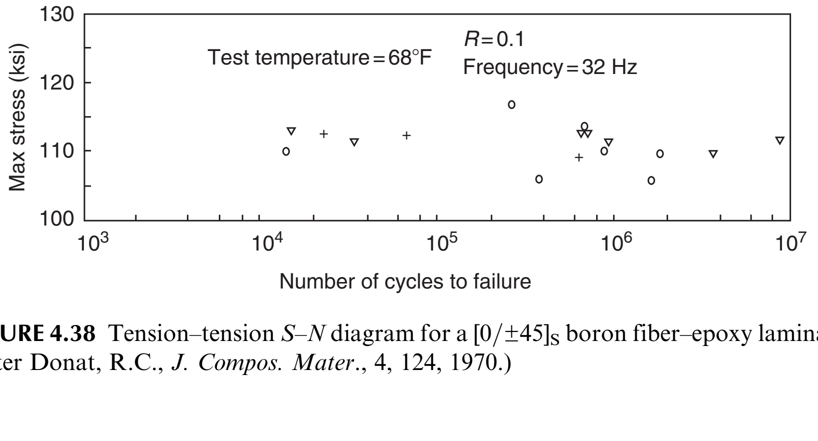

FIGURE 4.38 Tension–tension *S–N* diagram for a $[0/\pm45]_S$ boron fiber–epoxy laminate. (After Donat, R.C., *J. Compos. Mater.*, 4, 124, 1970.)

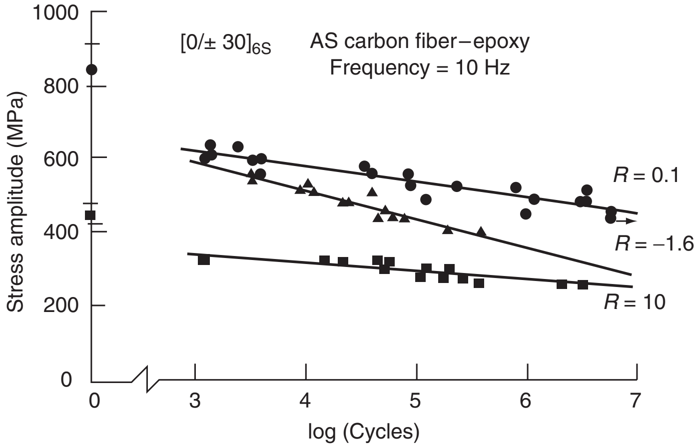

FIGURE 4.39 S–N diagrams for $[0/\pm 30]_{6S}$ AS carbon fiber–epoxy laminates at various fatigue stress ratios (*Note*: $R = 0.1$ in tension–tension cycling, $R = -1.6$ in tension–compression cycling, and $R = 10$ in compression–compression cycling). (After Ramani, S. V. and Williams, D.P., *Failure Mode in Composites III*, AIME, 1976.)

composites. Both types of fibers produce steep S–N plots for unidirectional 0° composites (Figures 4.40 and 4.41). An improvement in their fatigue performance can be achieved by hybridizing them with other high-modulus fibers, such as T-300 carbon (Figure 4.42).

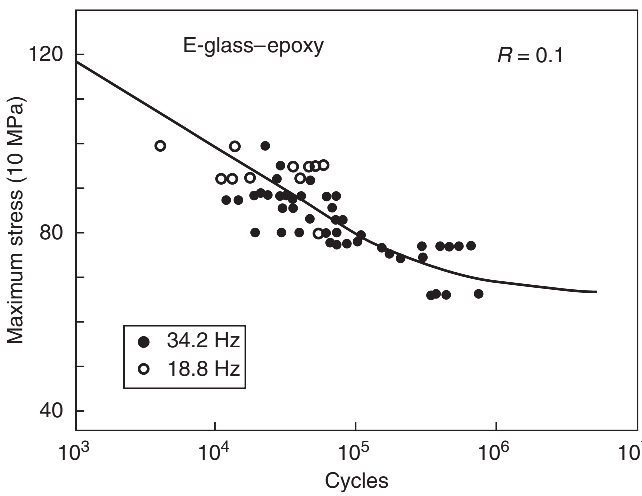

FIGURE 4.40 Tension–tension S–N diagram for a 0° E-glass–epoxy laminate. (After Hashin, Z. and Rotem, A., *J. Compos. Mater.*, 7, 448, 1973.)

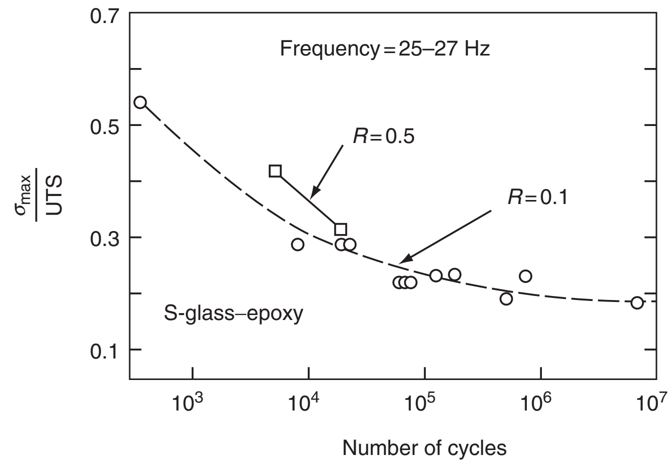

FIGURE 4.41 Tension–tension *S–N* diagram for a 0° S-glass–epoxy laminate at various fatigue stress ratios. (After Tobler, R.L. and Read, D.L., *J. Compos. Mater.*, 10, 32, 1976.)

The tension–tension fatigue properties of SMC composites have been reported by several investigators [30–32]. SMC materials containing E-glass fiber-reinforced polyester or vinyl ester matrix also do not exhibit fatigue limit. Their fatigue performance depends on the proportion of continuous and chopped fibers in the laminate (Figure 4.43).

4.2.2.2 Flexural Fatigue

The flexural fatigue performance of fiber-reinforced composite materials is in general less satisfactory than the tension–tension fatigue performance. This can

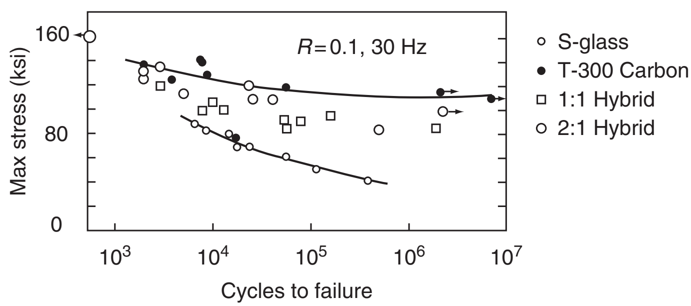

FIGURE 4.42 Tension–tension *S–N* diagram for a 0° S-glass, T-300 carbon, and S-glass/T-300 carbon interply hybrid laminates. (After Hofer, K.E., Jr., Stander, M., and Bennett, L.C., *Polym. Eng. Sci.*, 18, 120, 1978.)

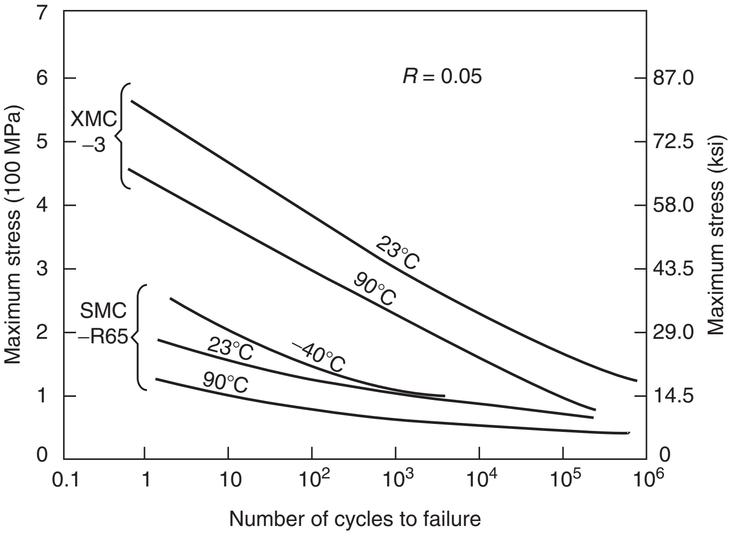

FIGURE 4.43 Tension–tension *S–N* diagrams for SMC laminates.

be observed in Figure 4.44, where the slope of the flexural *S–N* curve is greater than that of the tension–tension *S–N* curve for high-modulus carbon fibers. The lower fatigue strength in flexure is attributed to the weakness of composites on the compression side.

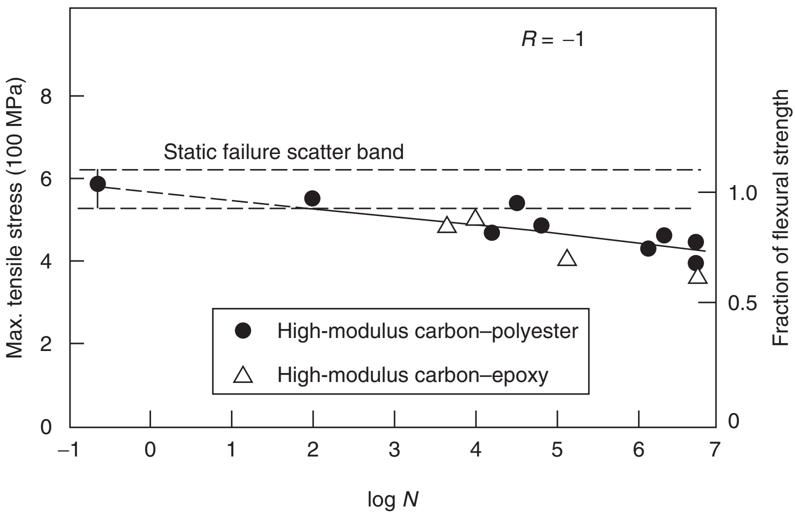

FIGURE 4.44 Flexural *S–N* diagram for 0° carbon fiber–epoxy and polyester laminates. (After Hahn, H.T. and Kim, R.Y., *J. Compos. Mater.*, 10, 156, 1976.)

4.2.2.3 Interlaminar Shear Fatigue

Fatigue characteristics of fiber-reinforced composite materials in the interlaminar shear (τ_{xz}) mode have been studied by Pipes [33] and several other investigators [34,35]. The interlaminar shear fatigue experiments were conducted using short-beam shear specimens. For a unidirectional 0° carbon fiber-reinforced epoxy, the interlaminar shear fatigue strength at 10^6 cycles was reduced to <55% of its static ILSS even though its tension–tension fatigue strength was nearly 80% of its static tensile strength (Figure 4.45). The interlaminar shear fatigue performance of a unidirectional 0° boron–epoxy system was similar to that of unidirectional 0° carbon–epoxy system. However, a reverse trend was observed for a unidirectional 0° S-glass-reinforced epoxy. For this material, the interlaminar shear fatigue strength at 10^6 cycles was ~60% of its static ILSS, but the tension–tension fatigue strength at 10^6 cycles was <40% of its static tensile strength. Unlike the static interlaminar strengths, fiber volume fraction [34] and fiber surface treatment [35] did not exhibit any significant influence on the high cycle interlaminar fatigue strength.

Wilson [36] has studied the interlaminar shear fatigue behavior of an SMC-R50 laminate. His results show that the interlaminar shear fatigue strength of this material at 10^6 cycles and 26°C is equal to 64% of its static ILSS. The interlaminar shear fatigue strength at 10^6 cycles and 90°C is between 45% and 50% of the corresponding ILSS.

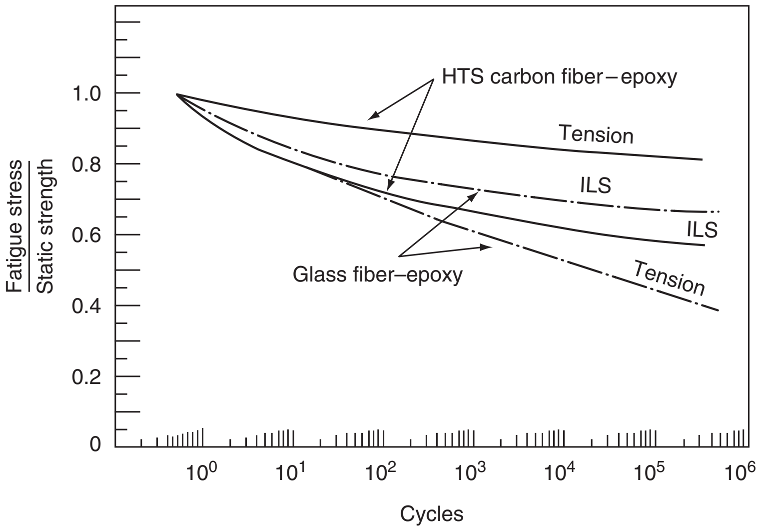

FIGURE 4.45 Interlaminar shear *S–N* diagrams for 0° carbon and glass fiber–epoxy laminates. (After Pipes, R.B., *Composite Materials: Testing and Design* (*Third Conference*), *ASTM STP*, 546, 419, 1974.)

4.2.2.4 Torsional Fatigue

The torsional fatigue behavior of carbon fiber-reinforced epoxy thin tubes is shown in Figure 4.46 for 0° and ±45° orientations. On a log–log scale, the *S–N* plot in alternating ($R = -1$) torsional fatigue exhibits linear behavior. The torsional fatigue strength of ±45° specimens is ~3.7–3.8 times higher than that of the 0° specimens at an equivalent number of cycles. The data for [0/±45] tubes fall between the 0° and ±45° lines. The 0° specimens failed by a few longitudinal cracks (cracks parallel to fibers), and the ±45° specimens failed by cracking along the ±45° lines and extensive delamination. Although the 0° specimens exhibited a lower torsional fatigue strength than ±45° specimens, they retained a much higher postfatigue static torsional strength.

Torsional fatigue data for a number of unidirectional 0° fiber-reinforced composites are compared in Figure 4.47. The data in this figure were obtained by shear strain cycling of solid rod specimens [37]. Fatigue testing under pure shear conditions clearly has a severe effect on unidirectional composites, all failing at ~10^3 cycles at approximately half the static shear strain to failure. Short-beam interlaminar shear fatigue experiments do not exhibit such rapid deterioration.

4.2.2.5 Compressive Fatigue

Compression–compression fatigue *S–N* diagram of various E-glass fiber-reinforced polyester and epoxy composites is shown in Figure 4.48. Similar trends are also observed for T-300 carbon fiber-reinforced epoxy systems [38].

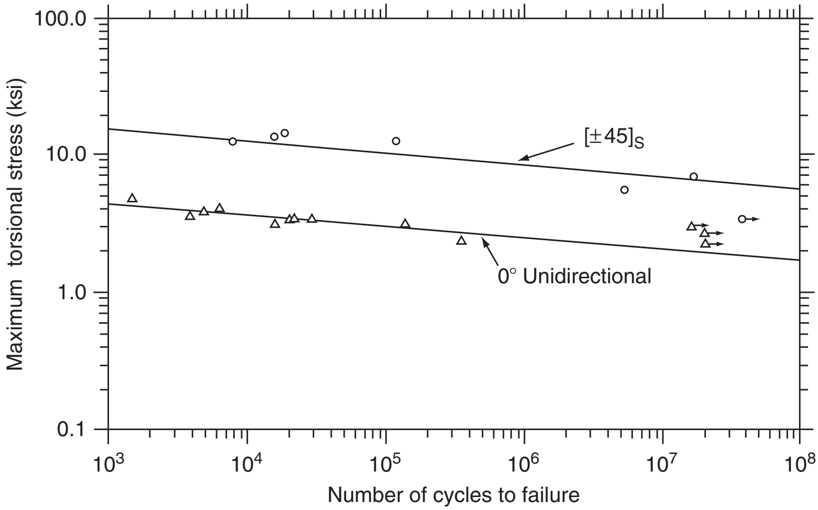

FIGURE 4.46 Torsional *S–N* diagrams for a 0° and $[\pm 45]_S$ high tensile strength carbon fiber–epoxy composites. (After Fujczak, B.R., Torsional fatigue behavior of graphite–epoxy cylinders, U.S. Army Armament Command, Report No. WVT-TR-74006, March 1974.)

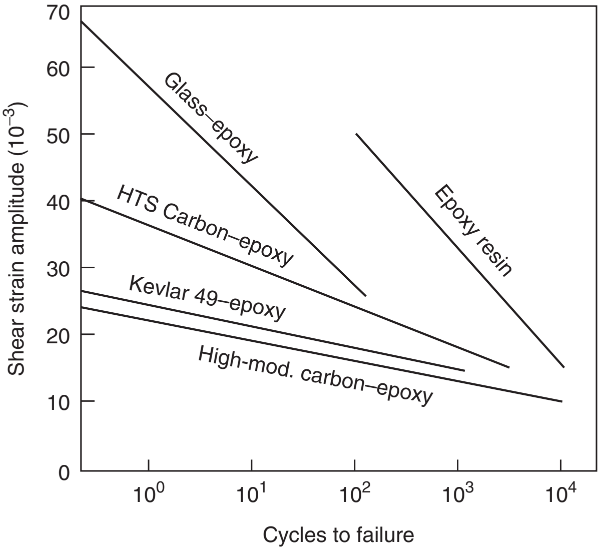

FIGURE 4.47 Torsional shear strain-cycle diagrams for various 0° fiber-reinforced composites. (After Phillips, D.C. and Scott, J.M., *Composites*, 8, 233, 1977.)

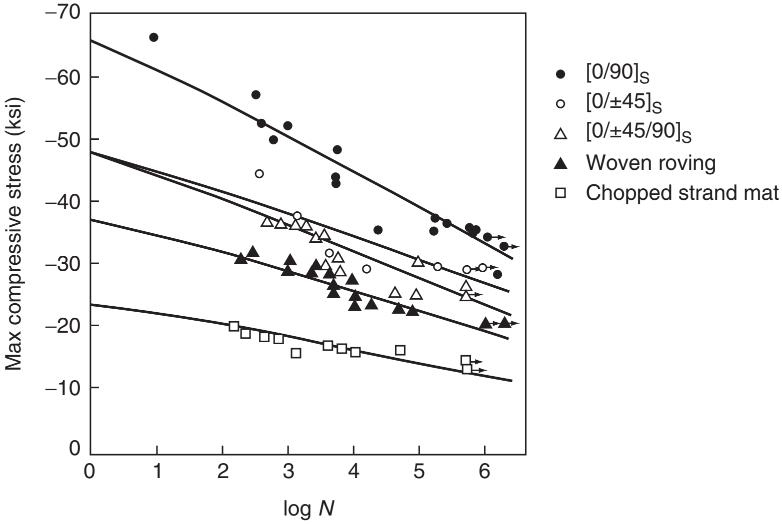

FIGURE 4.48 Compression–compression *S–N* diagrams for various composite laminates. (After Conners, J.D., Mandell, J.F., and McGarry, F.J., Compressive fatigue in glass and graphite reinforced composites, *Proceedings 34th Annual Technical Conference*, Society of the Plastics Industry, 1979.)

4.2.3 Variables in Fatigue Performance

4.2.3.1 Effect of Material Variables

Fatigue tests on unidirectional composites containing off-axis fibers (i.e., $\theta \neq 0°$) show a steady deterioration in fatigue strength with increasing fiber orientation angle [39]. Analogous to static tests, the fatigue failure mode in off-axis composites changes from progressive fiber failure at $\theta < 5°$ to matrix failure or fiber–matrix interface failure at $\theta > 5°$. However, a laminate containing alternate layers of ±5° fibers has higher fatigue strength than a 0° laminate (Figure 4.49). The fatigue performance of 0° laminates is also improved by the addition of a small percentage of 90° plies, which reduce the tendency of splitting (cracks running parallel to fibers in the 0° laminas) due to low transverse strengths of 0° laminas [40]. However, as the percentage of 90° plies increases, the fatigue strength is reduced.

Figure 4.50 shows the zero-tension fatigue data of two carbon fiber-reinforced PEEK laminates, namely, $[-45/0/45/90]_{2S}$ and $[\pm 45]_{4S}$. Higher fatigue strength of the $[-45/0/45/90]_{2S}$ is due to the presence of 0° fibers.

Experiments by Boller [40] and Davis et al. [41] have also shown that the fatigue performance of laminates containing woven fabrics or randomly oriented fibers is lower than that of unidirectional or nonwoven cross-ply laminates (Figure 4.51). Fatigue performance of laminates containing combinations

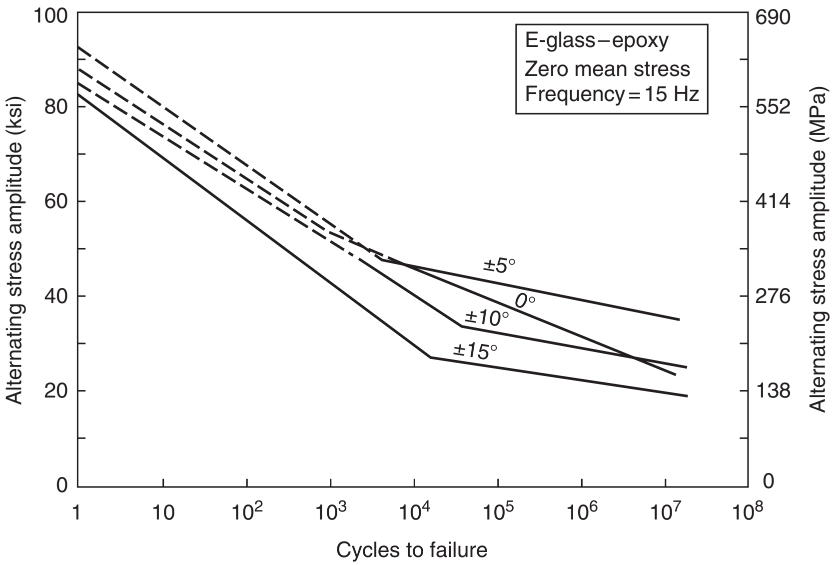

FIGURE 4.49 Effect of fiber orientation angles on the fatigue performance of E-glass–epoxy composites. (After Boller, K.H., *Mod. Plast.*, 41, 145, 1964.)

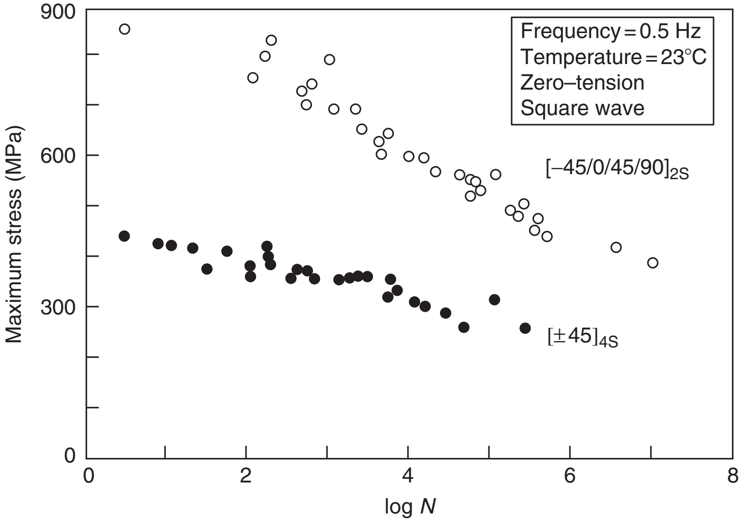

FIGURE 4.50 Zero-tension fatigue data of carbon fiber-reinforced PEEK laminates. (After Carlile, D.R., Leach, D.C., Moore, D.R., and Zahlan, N., *Advances in Thermoplastic Matrix Composite Materials, ASTM STP*, 1044, 199, 1989.)

of fiber orientations, such as $[0/90]_S$ and $[0/\pm45/90]_S$, are particularly sensitive to laminate configuration, since the signs of interlaminar stresses may be reversed by simple variations in stacking sequence (Figure 4.52).

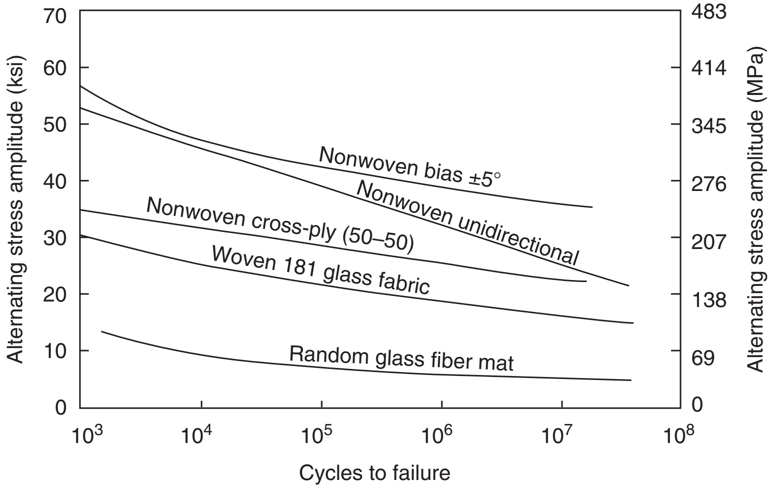

FIGURE 4.51 Fatigue performance of various woven fabric, nonwoven fabric, and mat-reinforced composite laminates. (After Davis, J.W., McCarthy, J.A., and Schrub, J.N., *Materials in Design Engineering*, 1964.)

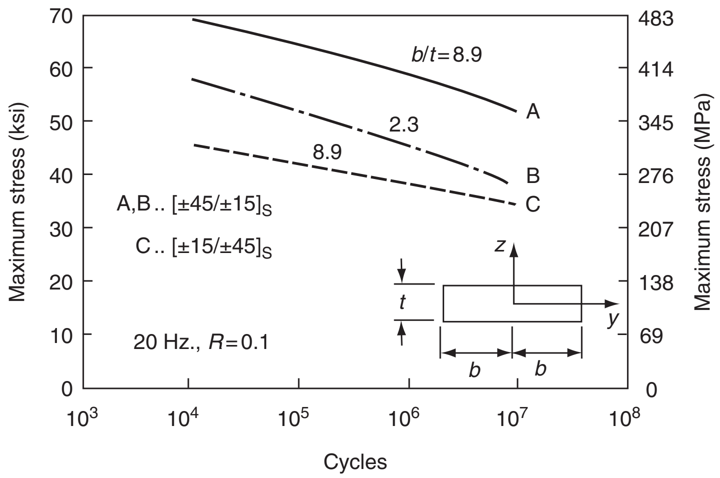

FIGURE 4.52 Effect of laminate stacking sequence on the tension–tension fatigue performance of carbon fiber–epoxy laminates.

A systematic study of the effects of resin type and coupling agents on the fatigue performance of fiber-reinforced polymer composites is lacking. Early work by Boller [40] on balanced E-glass fabric-reinforced laminates has shown the superiority of epoxies over polyesters and other thermoset resins. Mallick [32] has shown that vinyl ester resin provides a better fatigue damage resistance than polyester resin in an SMS-R65 laminate. However, within the same resin category, the effects of compositional differences (e.g., low reactivity vs. high reactivity in polyester resins or hard vs. flexible in epoxy resins) on the long-life fatigue performance are relatively small. In zero-tension fatigue ($R = 0$) experiments with chopped E-glass strand mat–polyester laminates, Owen and Rose [42] have shown that the principal effect of flexibilizing the resin is to delay the onset of fatigue damage. The long-term fatigue lives are not affected by the resin flexibility.

Investigations by Tanimoto and Amijima [43] as well as Dharan [44] have shown that, analogous to static tensile strength, the fatigue strength also increases with increasing fiber volume fraction. An example of the effect of fiber volume fraction is shown in Figure 4.53.

4.2.3.2 Effect of Mean Stress

The effect of tensile mean stress on the fatigue properties of fiber-reinforced composite materials was first studied by Boller [45]. For 0° and ±15° E-glass–epoxy laminates, the stress amplitude at a constant life tends to decrease with increasing tensile mean stress (Figure 4.54). This behavior is

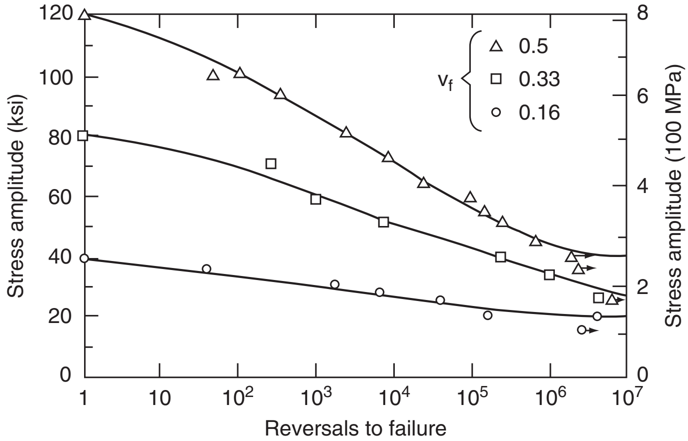

FIGURE 4.53 Effect of fiber volume fraction on the fatigue performance of 0° E-glass–epoxy laminates. (After Dharan, C.K.H., *J. Mater. Sci.*, 10, 1665, 1975.)

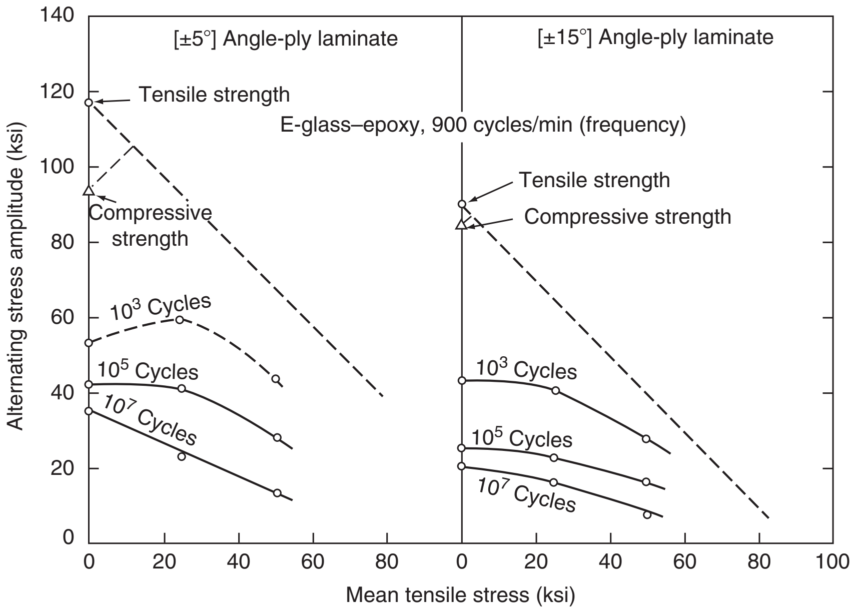

FIGURE 4.54 Effect of tensile mean stress on the fatigue strengths of two E-glass–epoxy laminates. (After Boller, K.H., Effect of tensile mean stresses on fatigue properties of plastic laminates reinforced with unwoven glass fibers, U.S. Air Force Materials Laboratory, Report No. ML-TDR-64–86, June 1964.)

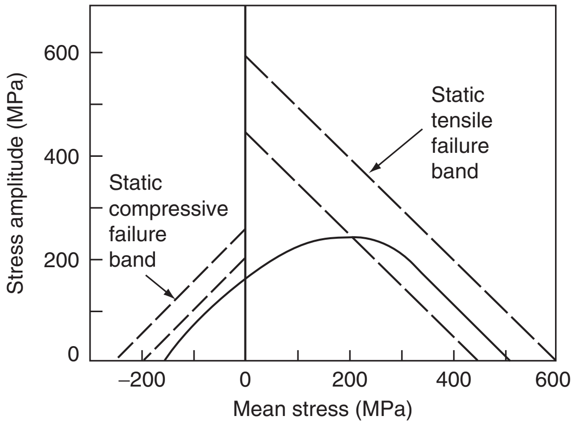

FIGURE 4.55 Effect of mean stress on the fatigue strength of a cross-ply carbon fiber–epoxy laminate. (After Owen, M.J. and Morris, S., *Carbon Fibres: Their Composites and Applications*, Plastic Institute, London, 1971.)

similar to that of ductile metals. However, the Goodman equation,* which is commonly used for ductile metals, may not be applicable for fiber-reinforced composite materials.

Figure 4.55 shows the relationship between mean stress and stress amplitude at 10^6 cycles for a cross-ply high-modulus carbon–epoxy composite. At high tensile mean stresses, the fatigue curve lies within the static tensile strength scatter band. However, low tensile mean stresses as well as compressive mean stresses have a significant adverse effect on the fatigue strength of this material. Similar behavior was also observed for a $[0/\pm 30]_{6S}$ carbon–epoxy composite [46].

Smith and Owen [47] have reported the effect of mean stresses on the stress amplitude for chopped E-glass strand mat–polyester composites. Their data (Figure 4.56) show that a small compressive mean stress may have a beneficial effect on the fatigue performance of random fiber composites.

* The Goodman equation used for taking into account the effect of tensile mean stresses for high cycle fatigue design of metals is given by

$$\frac{\sigma_a}{S_f} + \frac{\sigma_m}{S_{ut}} = 1,$$

where

σ_a = alternating stress
σ_m = mean stress
S_f = fatigue strength with $\sigma_m = 0$
S_{ut} = ultimate tensile strength

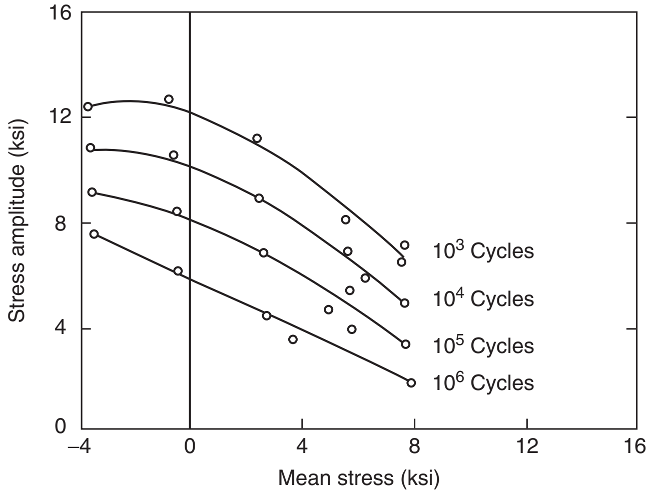

FIGURE 4.56 Effect of mean stress on the fatigue stress amplitude of an E-glass mat-reinforced polyester laminate. (After Smith, T.R. and Owen, M.J., *Mod. Plast.*, 46, 124, 1969.)

4.2.3.3 Effect of Frequency

The viscoelastic nature of polymers causes a phase difference between cyclic stresses and strains in polymer matrix composites, which is exemplified by hysteresis loops even at low stress levels. This results in energy accumulation in the form of heat within the material. Owing to the low thermal conductivity of the material, the heat is not easily dissipated, which in turn creates a temperature difference between the center and surfaces of a polymer matrix laminate. At a constant stress level, the temperature difference due to viscoelastic heating increases with increasing frequency of cycling (Figure 4.57). Depending on the frequency, it may attain a steady-state condition after a few cycles and then rise rapidly to high values shortly before the specimen failure.

In spite of the heating effect at high cyclic frequencies, Dally and Broutman [48] found only a modest decrease in fatigue life with increasing frequency up to 40 Hz for cross-ply as well as quasi-isotropic E-glass–epoxy composites. On the other hand, Mandell and Meier [49] found a decrease in the fatigue life of a cross-ply E-glass–epoxy laminate as the cyclic frequency was reduced from 1 to 0.1 Hz. For a $[\pm45]_{2S}$ T-300 carbon–epoxy laminate containing a center hole, Sun and Chan [50] have reported a moderate increase in fatigue life to a peak value between 1 and 30 Hz (Figure 4.58). The frequency at which the peak life was observed shifted toward a higher value as the load level was decreased. Similar results were observed by Saff [51] for $[\pm45]_{2S}$ AS carbon–epoxy laminates with center holes and Reifsnider et al. [52] for $[0/\pm45/0]_S$ boron–aluminum laminates with center holes.

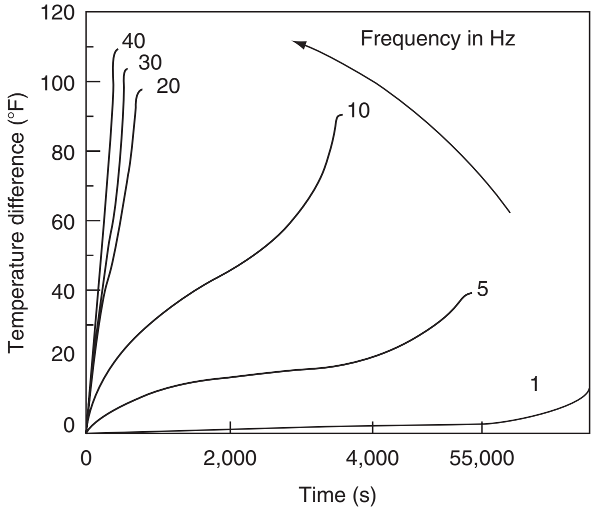

FIGURE 4.57 Difference in temperatures at the center and outside surfaces of cross-ply E-glass–epoxy laminates during fatigue cycling. (After Dally, J.W. and Broutman, L.J., *J. Compos. Mater.*, 1, 424, 1967.)

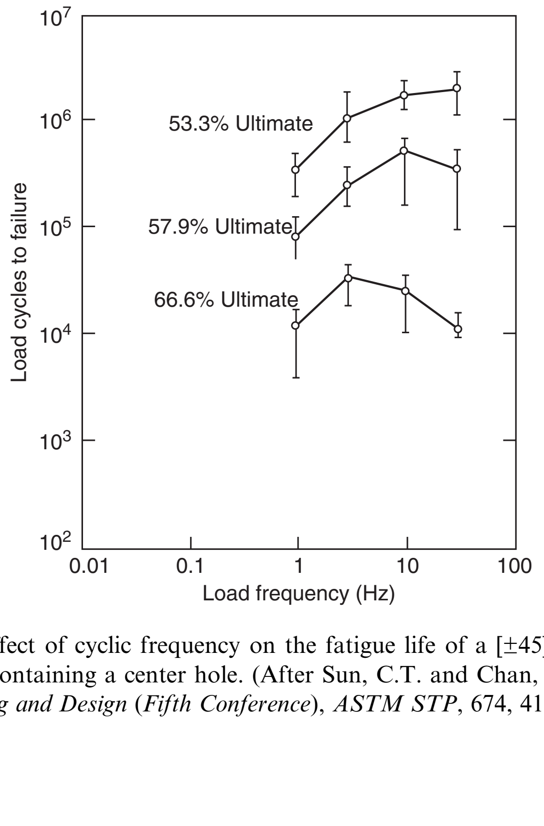

FIGURE 4.58 Effect of cyclic frequency on the fatigue life of a $[\pm 45]_{2S}$ carbon fiber–epoxy laminate containing a center hole. (After Sun, C.T. and Chan, W.S., *Composite Materials, Testing and Design* (*Fifth Conference*), *ASTM STP*, 674, 418, 1979.)

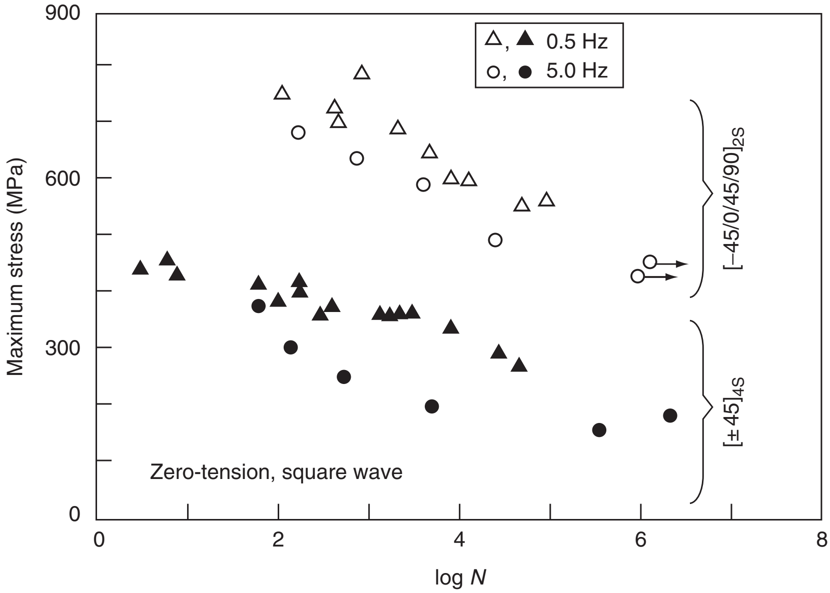

FIGURE 4.59 Influence of test frequency on the fatigue performance of $[-45/0/45/90]_{2S}$ and $[\pm 45]_{4S}$ carbon fiber-reinforced PEEK laminates. (After Carlile, D.R., Leach, D.C., Moore, D.R., and Zahlan, N., *Advances in Thermoplastic Matrix Composite Materials, ASTM STP*, 1044, 199, 1989.)

Frequency-dependent temperature rise was also detected in zero-tension fatigue testing of carbon fiber-reinforced PEEK laminates. Temperature rise was found to be dependent on the laminate configuration. For example, the temperature rise in $[-45/0/45/90]_{2S}$ laminates was only 20°C above the ambient temperature, but it was up to 150°C in $[\pm 45]_{4S}$ laminates, when both were fatigue-tested at 5 Hz. Higher temperature rise in the latter was attributed to their matrix-dominated layup. The difference in the fatigue response at 0.5 and 5 Hz for these laminate configurations is shown in Figure 4.59.

4.2.3.4 Effect of Notches

The fatigue strength of a fiber-reinforced polymer decreases with increasing notch depth (Figure 4.60) as well as increasing notch tip sharpness (Figure 4.61). Stacking sequence also plays an important role in the notch effect in fiber-reinforced polymers. Underwood and Kendall [53] have shown that multidirectional laminates containing 0° layers in the outer surfaces have a much longer fatigue life than either 90° or off-axis layers in the outer surfaces.

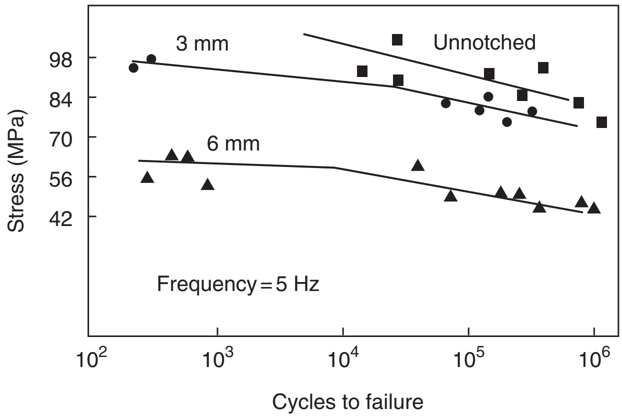

FIGURE 4.60 Effect of notch depth on the fatigue performance of a cross-ply E-glass–epoxy laminate. (After Carswell, W.S., *Composites*, 8, 251, 1977.)

Many fiber-reinforced polymers exhibit less notch sensitivity in fatigue than conventional metals. Fatigue damage created at the notch tip of these laminates tends to blunt the notch severity and increases their residual strengths. A comparison of fatigue strength reductions due to notching in a 2024-T4 aluminum alloy with those in a HT carbon–epoxy laminate (Table 4.9) demonstrates this important advantage of composite materials.

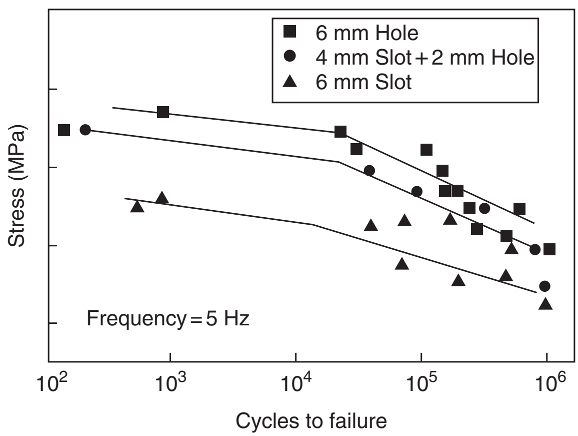

FIGURE 4.61 Effect of notch sharpness on the fatigue performance of a cross-ply E-glass–epoxy laminate. (After Carswell, W.S., *Composites*, 8, 251, 1977.)

TABLE 4.9
Comparison of Unnotched and Notched Fatigue Strengths[a]

			Ratio of Fatigue Strength to UTS			
			Unnotched		Notched ($K_t = 3$)[b]	
Material	Lamination Configuration	UTS, Mpa (ksi)	At 10^4 Cycles	At 10^7 Cycles	At 10^4 Cycles	At 10^7 Cycles
High tensile strength carbon fiber–epoxy ($\rho = 1.57$ g/cm^3)	0°	1138 (165)	0.76	0.70	0.42	0.36
	$[0/90]_S$	759 (110)	0.71	0.59	0.57	0.55
	$[0/90/\pm45]_S$	400 (58)	0.83	0.78	0.55	0.52
2024-T4 aluminum ($\rho = 2.77$ g/cm^3)	—	531 (77)	0.83	0.55	0.65	0.23

Source: Adapted from Freeman, W.T. and Kuebeler, G.C., *Composite Materials: Testing and Design* (*Third Conference*), *ASTM STP*, 546, 435, 1974.

[a] Fatigue stress ratio $R = 0.1$ for all experiments.
[b] K_t is the theoretical stress concentration factor.

4.2.4 Fatigue Damage Mechanisms in Tension–Tension Fatigue Tests

4.2.4.1 Continuous Fiber 0° Laminates

Depending on the maximum stress level, fiber type, and matrix fatigue properties, fatigue damage in continuous fiber 0° laminates is dominated either by fiber breakage or by matrix microcracking [54–56]. At very high fatigue stress levels, the fiber stress may exceed the lower limit of the fiber strength scatter band. Thus, on the first application on the maximum stress, the weakest fibers break. The locations of fiber breakage are randomly distributed in the volume of the composite (Figure 4.62a). High stress concentration at the broken fiber ends initiates more fiber breakage in the nearby areas. Rapidly increasing zones of fiber failure weaken the composite severely, leading eventually to catastrophic failure in a few hundred cycles.

At lower fatigue loads, the fiber stress may be less than the lower limit of the fiber strength scatter band, but the matrix strain may exceed the cyclic strain limit of the matrix. Thus failure initiation takes place by matrix microcracking (Figure 4.62b) instead of fiber failure. High stress concentrations at the ends of matrix microcracks may cause debonding at the fiber–matrix interface and occasional fiber failure. Since the propagation of matrix microcracks is frequently interrupted by debonding, the fatigue failure in this region is progressive and, depending on the stress level, may span over 10^6 cycles.

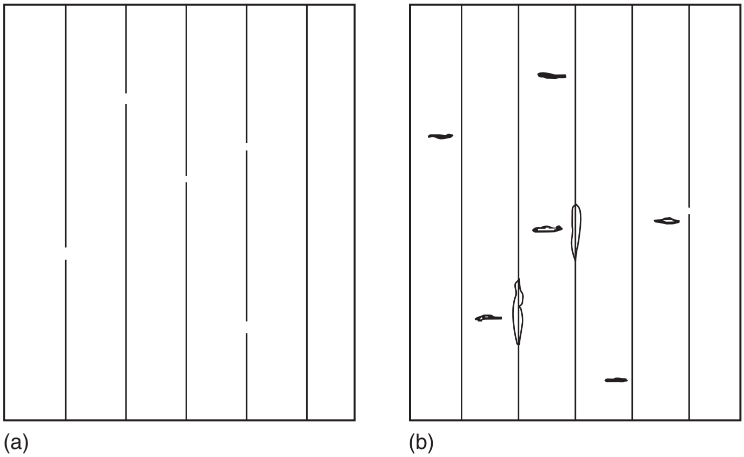

FIGURE 4.62 Damage development during tension–tension fatigue cycling of a 0° laminate. (a) Fiber breakage at high stress levels and (b) Matrix microcracks followed by debonding at low stress levels.

An important factor in determining the fatigue failure mechanism and the nature of the fatigue life diagram in 0° laminates is the fiber stiffness [56], which also controls the composite stiffness. For 0° composites, the composite fracture strain ε_{cu} in the longitudinal direction is equal to the fiber fracture strain ε_{fu}. Their scatter bands are also similar. Now, consider the tensile stress–strain diagrams (Figure 4.63) of a high-modulus fiber composite and a low-modulus fiber composite. For high-modulus fibers, such as GY-70 fibers, ε_{cu} is less than

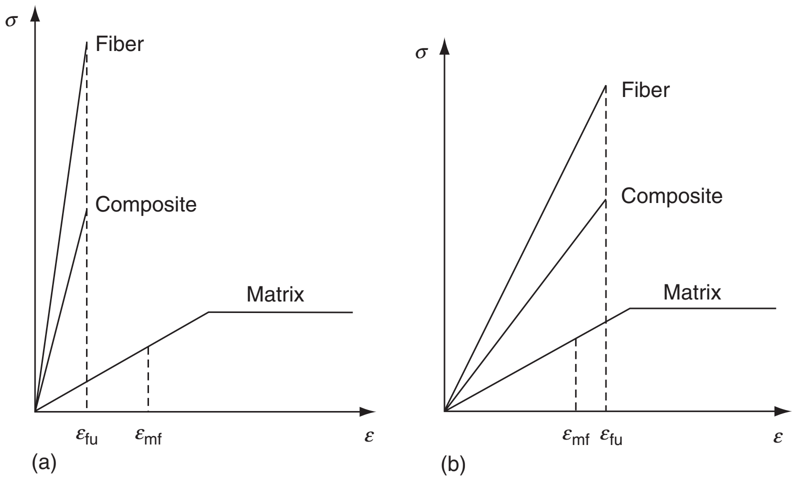

FIGURE 4.63 Schematic longitudinal tensile stress–strain diagrams for (a) high-modulus and (b) low-modulus 0° fiber-reinforced composite laminates. Note that ε_{mf} is the fatigue strain limit of the matrix.

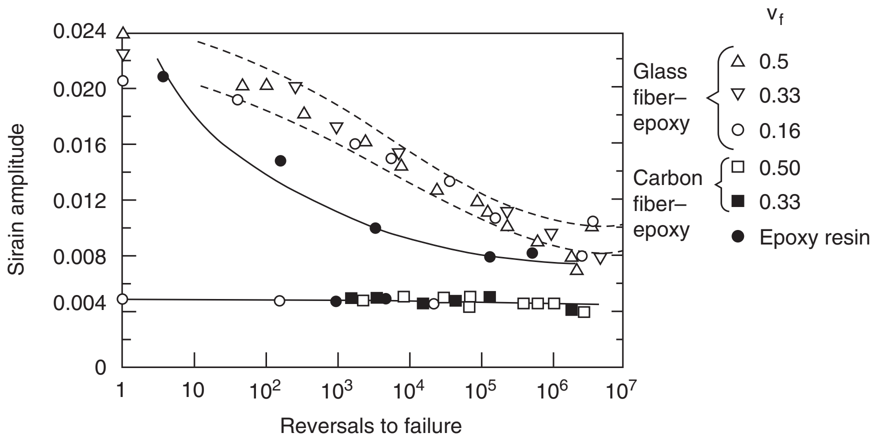

FIGURE 4.64 Cyclic strain amplitude vs. reversals-to-failure. (After Dharan, C.K.H., *J. Mater. Sci.*, 10, 1665, 1975.)

the fatigue strain limit of the matrix ε_{mf}. In this case, catastrophic fatigue failure, initiated by fiber breakage, is expected if the maximum fatigue strain due to applied load, ε_{max}, falls within the fiber fracture scatter band. The fatigue life diagram for such composites is nearly horizontal (as seen for the carbon fiber–epoxy composite in Figure 4.64) and the fatigue strength values are restricted within the fiber strength scatter band, as seen in Figure 4.36. No fatigue failure is expected below this scatter band.

For low-modulus fibers, such as T-300 carbon or E-glass, ε_{mf} falls below the lower bound of ε_{cu}. Thus, if ε_{max} is such that the matrix is strained above ε_{mf}, fatigue failure will be initiated by matrix microcracking and will continue in a progressive manner. The fatigue life diagram in this region will show a sloping band. At very low strain levels, where ε_{max} is less than ε_{mf}, there will be no fatigue failure. On the other hand, if ε_{max} exceeds the lower bound of ε_{cu} there will still be a catastrophic failure dominated by fiber breakage. The entire fatigue strain-life diagram for such composites shows three distinct regions, as seen for the glass fiber–epoxy composite in Figure 4.64:

1. Region I (high strain levels): catastrophic fatigue failure, low cycles to failure, nearly horizontal
2. Region II (intermediate strain levels): progressive fatigue failure, intermediate to high cycles to failure, steep slope
3. Region III (low strain levels): infinite life, horizontal

4.2.4.2 Cross-Ply and Other Multidirectional Continuous Fiber Laminates

Fatigue failure in cross-ply $[0/90]_S$ laminates begins with the formation of transverse microcracks at the fiber–matrix interface in the 90° layers (Figure 4.65).

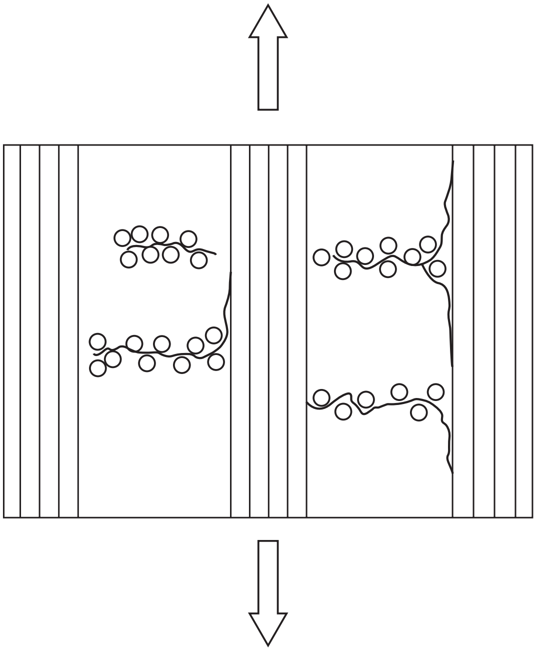

FIGURE 4.65 Damage development during tension–tension fatigue tests of a $[0/90]_S$ laminate.

As the cycling continues, these microcracks propagate across the 90° layers until they reach the adjacent 0° layers. Some of the microcracks are then deflected parallel to the 0° layers, causing delaminations between the 0° and the 90° layers. Depending on the stress level, a number of these transverse microcracks may appear at random locations in the first cycle; however as noted by Broutman and Sahu [57], the transverse crack density (number of microcracks per unit area) becomes nearly constant in a few cycles after their first appearance. It has been found by Agarwal and Dally [28] that delaminations do not propagate for nearly 95% of the fatigue life at a given stress level. It is only during the last 5% of the fatigue life that delaminations propagate rapidly across the 0°/90° interfaces before fiber failure in the 0° layers.

The sequence of damage development events in other multidirectional laminates containing off-axis fibers is similar to that found in cross-ply laminates. Reifsnider et al. [58] have divided this sequence into three regions (Figure 4.66). Region I usually involves matrix microcracking through the thickness of off-axis or 90° layers. These microcracks are parallel to fiber direction in these layers and develop quite early in the life cycle, but they quickly stabilize to a nearly uniform pattern with fixed spacing. The crack pattern developed in region I is called the characteristic damage state (CDS) and is similar to that

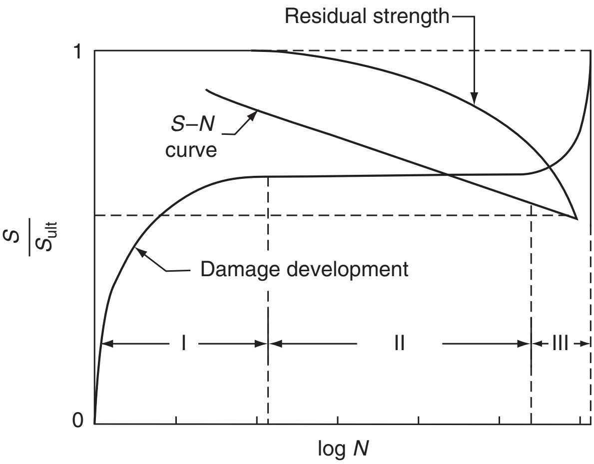

FIGURE 4.66 Three stages of fatigue damage development in multidirectional laminates. (After Reifsnider, K., Schultz, K., and Duke, J.C., *Long-Term Behavior of Composites, ASTM STP*, 813, 136, 1983.)

observed in quasi-static loadings. The CDS is a laminate property in the sense that it depends on the properties of individual layers, their thicknesses, and the stacking sequence. The CDS is found to be independent of load history, environment, residual stresses, or stresses due to moisture absorption.

Region II involves coupling and growth of matrix microcracks that ultimately lead to debonding at fiber–matrix interfaces and delaminations along layer interfaces. Both occur owing to high normal and shear stresses created at the tips of matrix microcracks. Edge delamination may also occur in some laminates (e.g., in $[0/\pm 45/90]_S$ laminates) because of high interlaminar stresses between various layers. As a result of delamination, local stresses in the 0° layers increase, since the delaminated off-axis plies cease to share the 0° load. Additional stresses in 0° layers, in turn, cause fiber failure and accelerate the fatigue failure process.

The principal failure mechanism in region III is the fiber fracture in 0° layers followed by debonding (longitudinal splitting) at fiber–matrix interfaces in these layers. These fiber fractures usually develop in local areas adjacent to the matrix microcracks in off-axis plies. It should be noted that fiber fracture occurs in both regions II and III; however, the rate of fiber fracture is much higher in region III, which leads quickly to laminate failure.

4.2.4.3 SMC-R Laminates

The inhomogeneous fiber distribution and random fiber orientation in SMC-R laminates give rise to a multitude of microscopic cracking modes, such as

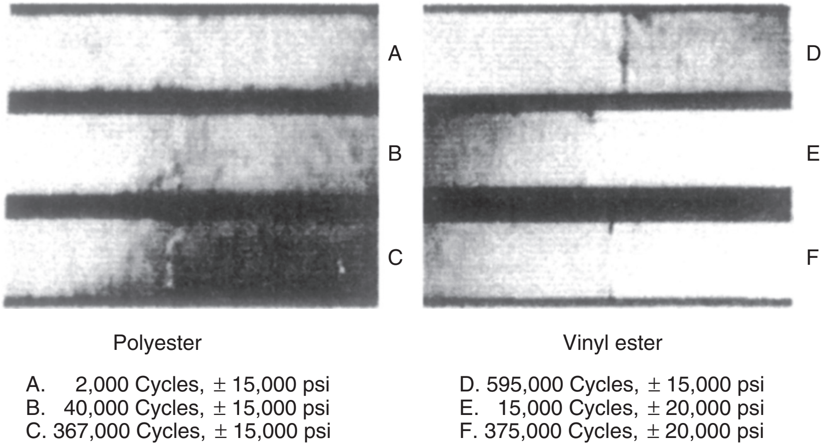

FIGURE 4.67 Damage development during flexural fatigue testing of SMC-R65 laminates containing polyester and vinyl ester matrix. Dark lines at the center of each specimen indicate the formation of microcracks nearly normal to the loading direction. Note that more microcracks were formed in polyester laminates than in vinyl ester laminates.

matrix cracking, fiber–matrix interfacial debonding, and fiber failure [59]. In matrix-rich areas containing sparsely dispersed fibers, matrix cracks are formed normal to the loading direction. Matrix cracks also develop in fiber-rich areas; however, these cracks are shorter in length owing to close interfiber spacing. Furthermore, if the fibers are at an angle with the loading direction, fiber–matrix debonding is observed. Fiber fracture is rarely observed in SMC-R laminates.

Crack density as well as average crack length in SMC-R laminates depends strongly on the stress level. At high fatigue stress levels (>60% of the ultimate tensile strength), the crack density is high but the average crack length is small. At lower stress levels, cracks have a lower density and longer lengths. Another important parameter in controlling crack density and length is the resin type [32]. This is demonstrated in Figure 4.67.

4.2.5 Fatigue Damage and Its Consequences

Unlike metals, fiber-reinforced composites seldom fail along a self-similar and well-defined crack path. Instead, fatigue damage in fiber-reinforced composites occurs at multiple locations in the form of fiber breakage, delamination, debonding, and matrix cracking or yielding. Depending on the stress level, fiber length, fiber orientation, constituent properties, and lamination configuration, some of these failure modes may appear either individually or in combination quite early in the life cycle of a composite. However, they

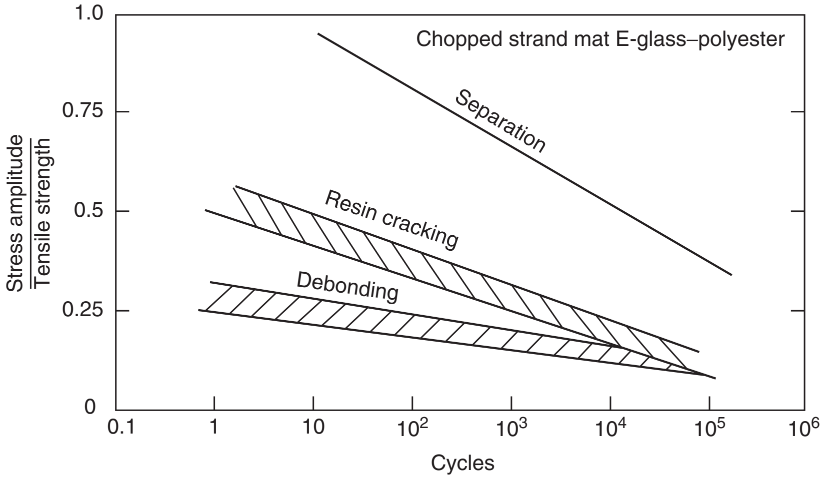

FIGURE 4.68 Various stages of damage growth during tension–tension fatigue cycling of E-glass mat-reinforced polyester laminates. (After Smith, T.R. and Owen, M.J., *Mod. Plast*., 46, 128, 1969.)

may not immediately precipitate a failure in the material. The damage grows in size or intensity in a progressive manner until the final rupture takes place. Figure 4.68 shows the *S*–*N* curve of a randomly oriented chopped E-glass fiber strand mat–polyester composite in which the onset of debonding and matrix cracking was observed two to three decades earlier than its final rupture [60].

As the fatigue damage accumulates with cycling, the dynamic modulus of the material is continuously decreased. This cyclic "softening" phenomenon causes an increase in strain level if a stress-controlled test is used and a decrease in stress level if a strain-controlled test is used. Because of less damage development in a continuously reducing stress field, a strain-controlled test is expected to produce a higher fatigue life than a stress-controlled test.

Many investigators have used the reduction in dynamic modulus as a method of monitoring the fatigue damage development in a composite. Since dynamic modulus can be measured frequently during fatigue cycling without discontinuing the test or affecting the material, it is a potential nondestructive test parameter and can be used to provide adequate warning before a structure becomes totally ineffective [61]. Figure 4.69 shows the dynamic modulus loss of $[\pm 45]_S$ boron fiber–epoxy laminates in strain-controlled tension–tension fatigue tests. Reduction in the dynamic modulus of an SMC-R in deflection-controlled flexural fatigue tests is shown in Figure 4.70. These examples demonstrate that the reduction in dynamic modulus depends on the stress or strain level, resin type, and lamination configuration. Other factors that may influence the dynamic modulus reduction are fiber type, fiber orientation angle, temperature,

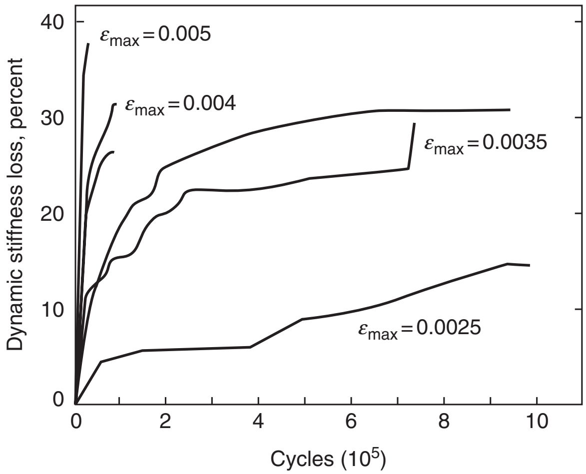

FIGURE 4.69 Reduction in dynamic modulus during strain-controlled fatigue testing of $[\pm 45]_S$ boron–epoxy laminates. (After O'Brien, T.K. and Reifsnider, K.L., *J. Compos. Mater.*, 15, 55, 1981.)

humidity, frequency, and test control mode. The significance of the fiber orientation angle is observed in unidirectional laminates in which the dynamic modulus reduction for $\theta = 0°$ orientation is considerably smaller than that for $\theta = 90°$ orientation.

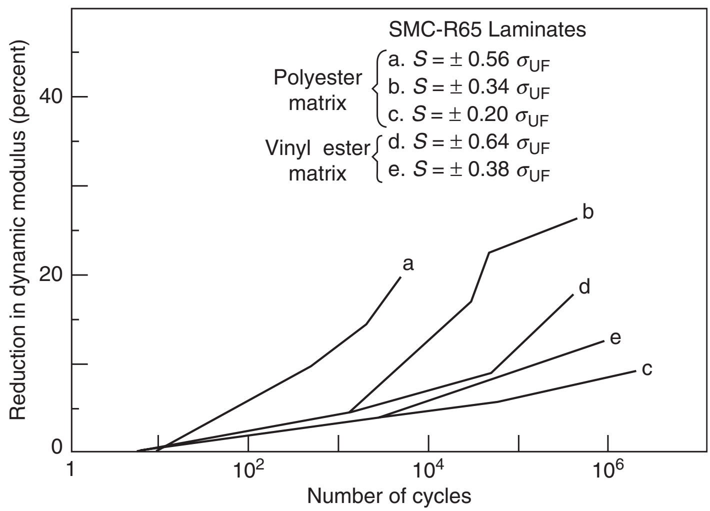

FIGURE 4.70 Reduction in dynamic modulus during flexural fatigue cycling of SMC-R65 laminates. (After Mallick, P.K., *Polym. Compos.*, 2, 18, 1981.)

Several phenomenological models have been proposed to describe the modulus reduction due to fatigue loading. One of them is due to Whitworth [62], who suggested the following equation for calculating the residual modulus E_N after N fatigue cycles in a stress-controlled fatigue test with a maximum stress level S:

$$E_N^a = E_0^a - H(E_0 - E_{\mathrm{ff}})^a \left(\frac{N}{N_{\mathrm{f}}}\right), \tag{4.27}$$

where

E_0 = initial modulus

E_{ff} = modulus at the time of fatigue failure

a, H = damage parameters determined by fitting Equation 4.27 to experimental data (Figure 4.71)

N_{f} = number of cycles to failure when the maximum stress level is $S(N_{\mathrm{f}} > N)$

If the fatigue test is conducted between fixed maximum and minimum stress levels, then the strain level increases with fatigue cycling due to increasing damage accumulation in the material. Assuming that the stress–strain response of the material is linear and the fatigue failure occurs when the maximum strain level reaches the static ultimate strain,

$$E_{\mathrm{ff}} = E_0 \frac{S}{\sigma_{\mathrm{U}}} = E_0 \bar{S}, \tag{4.28}$$

where

σ_{U} = ultimate static strength

$\bar{S} = \frac{S}{\sigma_{\mathrm{U}}}$

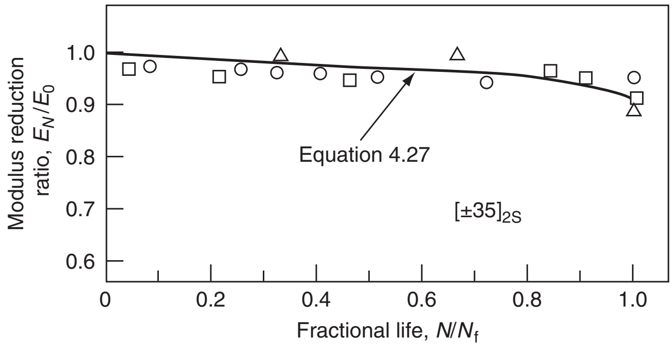

FIGURE 4.71 Dynamic modulus reduction ratio as a function of fractional life for $[\pm 35]_{2S}$ carbon fiber–epoxy laminates (after Whitworth, H.W., *ASME J. Eng. Mater. Technol.*, 112, 358, 1990.)

Thus, Equation 4.27 can be rewritten as

$$E_N^a = E_0^a - HE_0^a(1 - \bar{S})^a \left(\frac{N}{N_\mathrm{f}}\right). \tag{4.29}$$

Whitworth defined the fractional damage D_i in a composite laminate after N_i cycles of fatigue loading with a maximum stress level S_i as

$$D_i = \frac{E_0^a - E_{N_i}^a}{E_0^a - E_{\mathrm{ff}i}^a}. \tag{4.30}$$

Combining Equations 4.28 through 4.30, the fractional damage can be written as

$$D_i = r_i \frac{N_i}{N_{\mathrm{f}i}}, \tag{4.31}$$

where

$$r_i = \frac{H(1 - \bar{S}_i)^a}{1 - \bar{S}_i^a}.$$

In a variable amplitude stress loading, the total damage can be expressed as

$$D = \sum_{i=1}^{m} \frac{r_i}{r_m} \frac{N_i}{N_{\mathrm{f}i}}, \tag{4.32}$$

where

$\frac{r_i}{r_m} = \frac{(1 - \bar{S}_i)(1 - \bar{S}_m^a)}{(1 - \bar{S}_i^a)(1 - \bar{S}_m)}$

N_i = number of cycles endured at a maximum stress level S_i

$N_{\mathrm{f}i}$ = fatigue life at S_i

m = number of the stress level

In a variable amplitude stress loading, failure occurs when the sum of the fractional damages equals 1, that is, $D = 1$. In addition, note that for $a = 1$, Equation 4.32 transforms into the linear damage rule (Miner's rule), which is frequently used for describing damage in metals:

$$\text{Miner's rule: } D = \sum_{i=1}^{m} \frac{N_i}{N_{fi}}. \tag{4.33}$$

EXAMPLE 4.2

A quasi-isotropic T-300 carbon fiber–epoxy laminate is subjected to 100,000 cycles at 382 MPa after which the stress level is increased to 437 MPa. Estimate the number of cycles the laminate will survive at the second stress level. Median fatigue lives at 382 and 437 MPa are 252,852 and 18,922 cycles, respectively. From the modulus vs. fatigue cycle data, the constant a and H in Equation 4.27 have been determined as 1.47 and 1.66, respectively (see Ref. [62]). The ultimate static strength of this material is 545 MPa.

SOLUTION

Using Equation 4.32, we can write, for failure to occur at the end of second stress cycling,

$$D = 1 = \frac{r_1}{r_2}\frac{N_1}{N_{f1}} + \frac{r_2}{r_2}\frac{N_2}{N_{f2}} \text{ which gives,}$$

$$N_2 = N_{f2}\left(1 - \frac{r_1}{r_2}\frac{N_1}{N_{f1}}\right).$$

In this example,

$$\begin{aligned}
\sigma_U &= 545 \text{ MPa} \\
S_1 &= 382 \text{ MPa} \\
N_{f1} &= 252{,}852 \text{ cycles} \\
N_1 &= 100{,}000 \text{ cycles} \\
S_2 &= 437 \text{ MPa} \\
N_{f2} &= 18{,}922 \text{ cycles}
\end{aligned}$$

Therefore,

$$r_1 = (1.66)\frac{\left(1 - \frac{382}{545}\right)^{1.47}}{1 - \left(\frac{382}{545}\right)^{1.47}} = 0.6917.$$

Similarly, $r_2 = 0.5551$

Thus,

$$N_2 = (18{,}922)\left[1 - \left(\frac{0.6917}{0.5551}\right)\left(\frac{100{,}000}{252{,}852}\right)\right] \cong 9{,}600 \text{ cycles.}$$

This compares favorably with the experimental median value of 10,800 cycles [62].

4.2.6 Postfatigue Residual Strength

The postfatigue performance of a fiber-reinforced composite is studied by measuring its static modulus and strength after cycling it for various fractions of its total life. Both static modulus and strength are reduced with increasing number of cycles. Broutman and Sahu [57] reported that much of the static strength of a $[0/90]_S$ E-glass fiber–epoxy composite is reduced rapidly in the first 25% of its fatigue life, which is then followed by a much slower rate of strength reduction until the final rupture occurs (Figure 4.72). Tanimoto and Amijima [43] also observed similar behavior for a woven E-glass cloth–polyester laminate; however, in this case the reduction in strength takes place only after a slight increase at <2% of the total life.

An initial increase in static strength was also observed by Reifsnider et al. [52] for a $[0/\pm45/0]_S$ boron fiber–epoxy laminate containing a center hole. This unique postfatigue behavior of a composite material was explained by means of a wear-in and wear-out mechanism in damage development. The wear-in process takes place in the early stages of fatigue cycling. During this process,

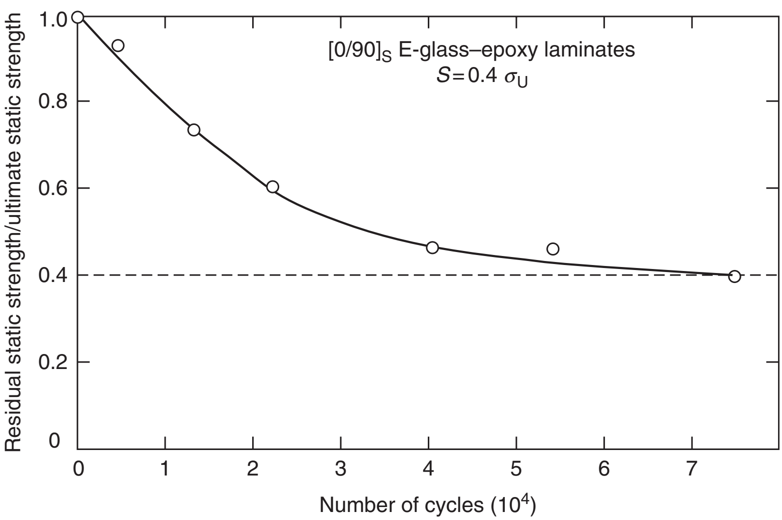

FIGURE 4.72 Reduction in residual static strengths of $[0/90]_S$ laminates after fatigue testing to various cycles. (After Broutman, L.J. and Sahu, S., Progressive damage of a glass reinforced plastic during fatigue, *Proceedings 20th Annual Technical Conference*, Society of the Plastics Industry, 1969.)

the damage developed locally around the center hole reduces the stress concentration in the vicinity of the hole, thus resulting in increased strength. This beneficial stage of fatigue cycling is followed by the wear-out process, which comprises large-scale and widespread damage development leading to strength reduction. Thus, the residual strength of a composite after a period of fatigue cycling is modeled as

$$\sigma_{\text{residual}} = \sigma_{\text{U}} + \sigma_{\text{wear-in}} - \sigma_{\text{wear-out}},$$

where

σ_{U} = ultimate static strength
$\sigma_{\text{wear-in}}$ = change in static strength due to wear-in
$\sigma_{\text{wear-out}}$ = change in static strength due to wear-out

The effect of wear-in is more pronounced at high fatigue load levels. Since fatigue life is longer at low load levels, there is a greater possibility of developing large-scale damage throughout the material. Thus, at low load levels, the effect of wear-out is more pronounced.

A number of phenomenological equations have been proposed to predict the residual static strength of a fatigued composite laminate [63,64]. The simplest among them is based on the assumption of linear strength reduction [63] and is given as

$$\sigma_{r_i} = \sigma_{U_{i-1}} - (\sigma_{U_0} - S_i)\frac{N_i}{N_{\text{f}i}}, \tag{4.34}$$

where

σ_{r_i} = residual strength after N_i cycles at the ith stress level S_i
$N_{\text{f}i}$ = fatigue life at S_i
σ_{U_0} = ultimate static strength of the original laminate
$\sigma_{U_{i-1}}$ = ultimate static strength before being cycled at S_i

In Equation 4.34, the ratio $N_i/N_{\text{f}i}$ represents the fractional fatigue life spent at S_i.

Assuming a nonlinear strength degradation model, Yang [64] proposed the following equation for the residual strength for a composite laminate after N fatigue cycles:

$$\sigma_{\text{res}}^c = \sigma_{\text{U}}^c - \sigma_0^c K S^d N, \tag{4.35}$$

where

c = damage development parameter
σ_0 = location parameter in a two-parameter Weibull function for the static strength distribution of the laminate
S = stress range in the fatigue test = $\sigma_{\max} - \sigma_{\min}$
K, d = parameters used to describe the S–N diagram as $KS^d N_{\text{f}} = 1$

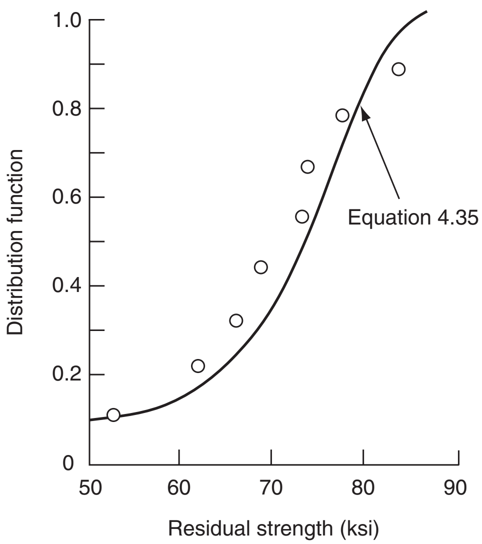

FIGURE 4.73 Residual strength distribution in postfatigue tension tests. (After Yang, J.N., *J. Compos. Mater.*, 12, 19, 1978.)

Procedures for determining c, d, and K are given in Ref. [64]. It is worth noting that, just as the static strengths, the residual strengths at the end of a prescribed number of cycles also follow the Weibull distribution (Figure 4.73).

4.3 IMPACT PROPERTIES

The impact properties of a material represent its capacity to absorb and dissipate energies under impact or shock loading. In practice, the impact condition may range from the accidental dropping of hand tools to high-speed collisions, and the response of a structure may range from localized damage to total disintegration. If a material is strain rate sensitive, its static mechanical properties cannot be used in designing against impact failure. Furthermore, the fracture modes in impact conditions can be quite different from those observed in static tests.

A variety of standard impact test methods are available for metals (ASTM E23) and unreinforced polymers (ASTM D256). Some of these tests have also been adopted for fiber-reinforced composite materials. However, as in the case of metals and unreinforced polymers, the impact tests do not yield basic material property data that can be used for design purposes. They are useful in comparing the failure modes and energy absorption capabilities of two different materials under identical impact conditions. They can also be used in the areas of quality control and materials development.

4.3.1 Charpy, Izod, and Drop-Weight Impact Test

Charpy and Izod impact tests are performed on commercially available machines in which a pendulum hammer is released from a standard height to contact a beam specimen (either notched or unnotched) with a specified kinetic energy. A horizontal simply supported beam specimen is used in the Charpy test (Figure 4.74a), whereas a vertical cantilever beam specimen is used in the Izod test (Figure 4.74b). The energy absorbed in breaking the specimen, usually indicated by the position of a pointer on a calibrated dial attached to the testing machine, is equal to the difference between the energy of the pendulum hammer at the instant of impact and the energy remaining in the pendulum hammer after breaking the specimen.

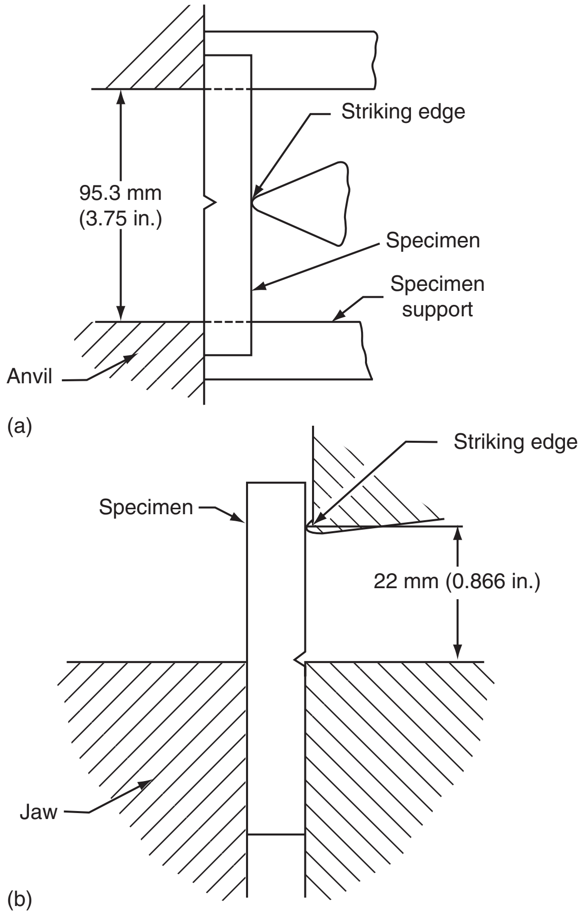

FIGURE 4.74 Schematic arrangements for (a) Charpy and (b) Izod impact tests.

TABLE 4.10
Standard V-Notched Charpy and Izod Impact Energies of Various Materials

Material	Impact Energy, kJ/m^2 (ft lb/in.^{2})	
	Charpy	Izod
S-glass–epoxy, 0°, $v_f = 55\%$	734 (348)	—
Boron–epoxy, 0°, $v_f = 55\%$	109–190 (51.5–90)	—
Kevlar 49–epoxy, 0°, $v_f = 60\%$	317 (150)	158 (75)
AS carbon–epoxy, 0°, $v_f = 60\%$	101 (48)	33 (15.5)
HMS carbon–epoxy, 0°, $v_f = 60\%$	23 (11)	7.5 (3.6)
T-300 carbon–epoxy, 0°, $v_f = 60\%$	132 (62.6)	67.3 (31.9)
4340 Steel ($R_c = 43$–46)	214 (102)	—
6061-T6 aluminum alloy	153 (72.5)	—
7075-T6 aluminum alloy	67 (31.7)	—

Table 4.10 compares the longitudinal Charpy and Izod impact energies of a number of unidirectional 0° laminates and conventional metals. In general, carbon and boron fiber-reinforced epoxies have lower impact energies than many metals. However, the impact energies of glass and Kevlar 49 fiber-reinforced epoxies are equal to or better than those of steel and aluminum alloys. Another point to note in this table is that the Izod impact energies are lower than the Charpy impact energies.

The drop-weight impact test uses the free fall of a known weight to supply the energy to break a beam or a plate specimen (Figure 4.75). The specimen can be either simply supported or fixed. The kinetic energy of the falling weight is adjusted by varying its drop height. The impact load on the specimen is measured by instrumenting either the striking head or the specimen supports. Energy absorbed by the specimen is calculated as

$$U_t = \frac{W}{2g}\left(u_1^2 - u_2^2\right), \tag{4.36}$$

where

W = weight of the striking head
u_1 = velocity of the striking head just before impact ($=\sqrt{2gH}$)
u_2 = measured velocity of the striking head just after impact
g = acceleration due to gravity
H = drop height

A comparison of drop-weight impact energies of carbon, Kevlar 49, and E-glass fiber-reinforced epoxy laminates is given in Table 4.11.

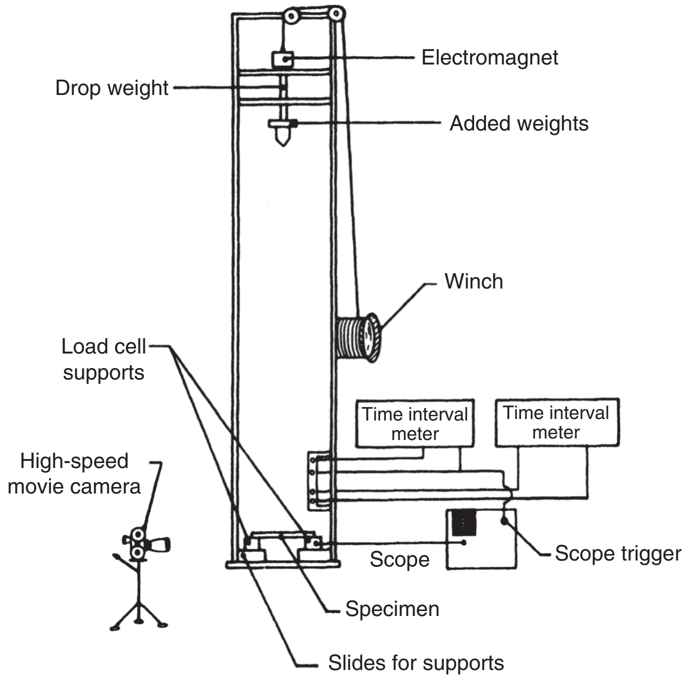

FIGURE 4.75 Schematic arrangement for a drop-weight impact test.

TABLE 4.11
Drop-Weight Impact Force and Energy Values[a]

Material	Force per Unit Thickness, kN/mm (lb/in.)		Energy per Unit Thickness, J/mm (ft lb/in.)	
AS-4 carbon–epoxy				
10-ply cross-ply	1.07	(6,110)	0.155	(2.92)
10-ply fabric	1.21	(6,910)	0.209	(3.94)
Kevlar 49–epoxy				
10-ply cross-ply	1.16	(6,630)	0.284	(5.36)
10-ply fabric	0.91	(5,200)	0.233	(4.39)
E-glass–epoxy				
6-ply cross-ply	2.83	(16,170)	0.739	(13.95)
10-ply cross-ply	2.90	(16,570)	0.789	(14.89)
10-ply fabric	0.99	(5,660)	0.206	(3.89)

Source: Adapted from Winkel, J.D. and Adams, D.F., *Composites*, 16, 268, 1985.

[a] Simply supported 127 mm^2 plate specimens were used in these experiments.

The impact energy measured in all these tests depends on the ratio of beam length to effective depth. Below a critical value of this ratio, there is a considerable increase in impact energy caused by extensive delamination [65]. The effect of notch geometry has relatively little influence on the impact energy because delamination at the notch root at low stresses tends to reduce its severity.

4.3.2 Fracture Initiation and Propagation Energies

The impact energy measured in either of the impact tests does not indicate the fracture behavior of a material unless the relative values of fracture initiation and propagation energies are known. Thus, for example, a high-strength brittle material may have a high fracture initiation energy but a low fracture propagation energy, and the reverse may be true for a low-strength ductile material. Even though the sum of these two energies may be the same, their fracture behavior is completely different. Unless the broken specimens are available for fracture mode inspection, the toughness of a material cannot be judged by the total impact energy alone.

Fracture initiation and propagation energies are determined from the measurements of the dynamic load and striking head velocity during the time of contact. Through proper instrumentation, the load and velocity signals are integrated to produce the variation of cumulative energy as a function of time. Both load–time and energy–time responses are recorded and are then used for energy absorption analysis.

The load–time response during the impact test of a unidirectional composite (Figure 4.76) can be conveniently divided into three regions [66]:

Preinitial fracture region: The preinitial fracture behavior represents the strain energy in the beam specimen before the initial fracture occurs. In unidirectional 0° specimens, strain energy is stored principally by the fibers. The contribution from the matrix is negligible. The fiber strain energy U_f is estimated as

$$U_f = \frac{\sigma_f^2}{6E_f} v_f, \tag{4.37}$$

where

σ_f = longitudinal stress at the outermost fibers in the beam specimen
E_f = fiber modulus
v_f = fiber volume fraction

This equation indicates that the energy absorption in this region can be increased by using a low-modulus fiber and a high fiber volume fraction.

Initial fracture region: Fracture initiation at or near the peak load occurs either by the tensile failure of the outermost fibers or by interlaminar shear

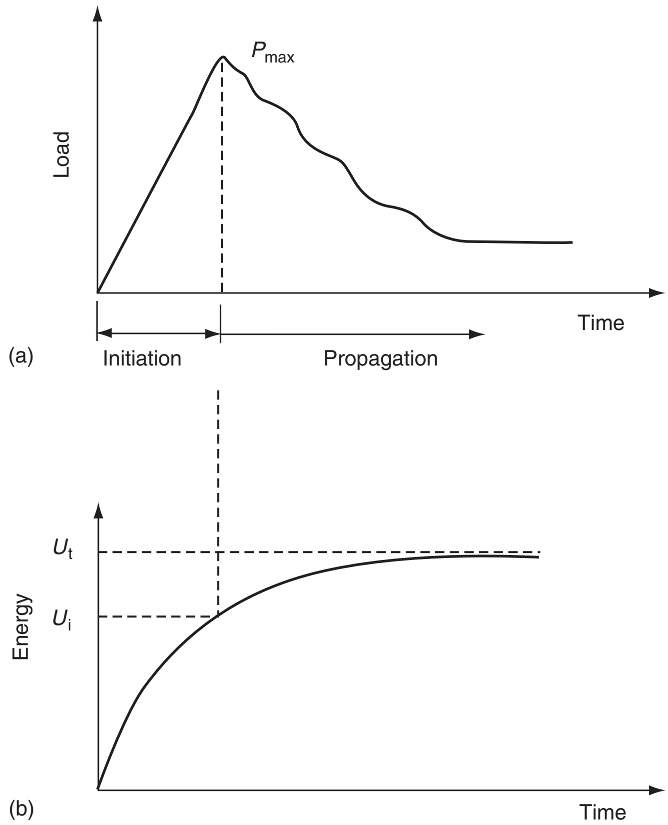

FIGURE 4.76 Schematic (a) load–time and (b) energy–time curves obtained in an instrumented impact test.

failure. In many cases, fiber microbuckling is observed at the location of impact (i.e., on the compression side of the specimen) before reaching the peak load. Compressive yielding is observed in Kevlar 49 composites.

Interlaminar shear failure precedes fiber tensile failure if either the specimen length-to-depth ratio is low or the ILSS is lower than the tensile strength of the material. If the ILSS is high and fibers have either a low tensile strength or a low tensile strain-to-failure, shear failure would not be the first event in the fracture process. Instead, fiber tensile failure would occur on the nonimpacting side as the peak load is reached.

Postinitial fracture region: The postinitial fracture region represents the fracture propagation stage. In unidirectional composites containing low strain-to-failure fibers (e.g., GY-70 carbon fiber), a brittle failure mode is observed. On the other hand, many other fiber-reinforced composites, including unidirectional E-glass, S-glass, T-300 or AS carbon, and Kevlar 49, fail in a sequential manner starting with fiber failure, which is followed by debonding and fiber pullout within each layer and delamination between various layers. Additionally, Kevlar 49 composites exhibit considerable yielding and may not even fracture in an impact test.

Progressive delamination is the most desirable fracture mode in high-energy impact situations. High shear stress ahead of the crack tip causes delamination between adjacent layers, which in turn arrests the advancing crack and reduces its severity as it reaches the delaminated interface. Thus, the specimen continues to carry the load until the fibers in the next layer fail in tension. Depending on the material and lamination configuration, this process is repeated several times until the crack runs through the entire thickness. Energy absorbed in delamination depends on the interlaminar shear fracture energy and the length of delamination, as well as the number of delaminations. Owing to progressive delamination, the material exhibits a "ductile" behavior and absorbs a significant amount of impact energy.

Referring to Figure 4.76b, the energy corresponding to the peak load is called the fracture initiation energy U_i. The remaining energy is called the fracture propagation energy U_p, where

$$U_p = U_t - U_i. \tag{4.38}$$

These energy values are often normalized by dividing them either by the specimen width or by specimen cross-sectional area (effective cross-sectional area in notched specimens).

The fracture initiation and propagation energies of a number of unidirectional fiber-reinforced epoxies are compared in Table 4.12. With the exception of GY-70, other composites in this table fail in a progressive manner. An E-glass–epoxy composite has a much higher fracture initiation energy than other composites owing to higher strain energy. The fracture propagation energy for E-glass and Kevlar 49 fiber composites are higher than that for a T-300 carbon fiber composite. Thus, both E-glass and Kevlar 49 fiber composites have higher impact toughness than carbon fiber composites.

4.3.3 Material Parameters

The primary factor influencing the impact energy of a unidirectional 0° composite is the fiber type. E-glass fiber composites have higher impact energy due to the relatively high strain-to-failure of E-glass fibers. Carbon and boron fiber composites have low strain-to-failure that leads to low impact energies for these composites. Increasing the fiber volume fraction also leads to higher impact energy, as illustrated in Figure 4.77.

TABLE 4.12
Static and Impact Properties of Unidirectional 0° Fiber-Reinforced Epoxy Composites

		Static Flexure Test		Unnotched Charpy Impact Test				
Fiber Type	Fiber Strain Energy Index	L/h	σ_{max}, MPa (ksi)	L/h	σ_{max}, MPa (ksi)	U_i, kJ/m^2 (ft lb/in.^{2})	U_p, kJ/m^2 (ft lb/in.^{2})	U_t, kJ/m^2 (ft lb/in.^{2})
E-Glass	82	15.8	1641 (238)	16.1	1938 (281)	466.2 (222)	155.4 (74)	621.6 (296)
Kevlar 49	29	11	703 (102)	10.5	676 (98)	76 (36.2)	162.5 (77.4)	238.5 (113.6)
T-300 Carbon	10.7	14.6	1572 (228)	14.6	1579 (229)	85.7 (40.8)	101.2 (48.2)	186.9 (89)
GY-70 Carbon	2.8	12.8	662 (96)	14.6	483 (70)	12.3 (5.85)	0	12.3 (5.85)

Source: Adapted from Mallick, P.K. and Broutman, L.J., *J. Test. Eval.*, 5, 190, 1977.

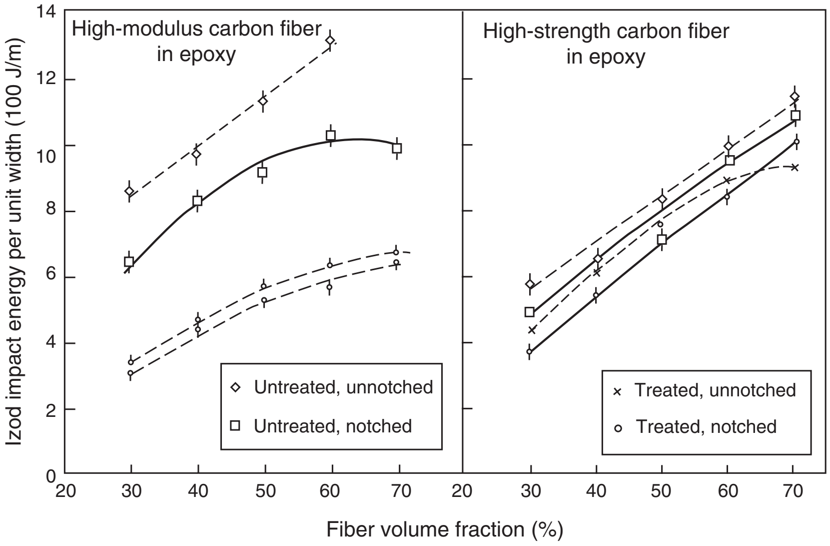

FIGURE 4.77 Variation of unnotched Izod impact energy with fiber volume fraction in 0° carbon–epoxy laminates. (After Hancox, N.L., *Composites*, 3, 41, 1971.)

The next important factor influencing the impact energy is the fiber–matrix interfacial shear strength. Several investigators [69–71] have reported that impact energy is reduced when fibers are surface-treated for improved adhesion with the matrix. At high levels of adhesion, the failure mode is brittle and relatively little energy is absorbed. At very low levels of adhesion, multiple delamination may occur without significant fiber failure. Although the energy absorption is high, failure may take place catastrophically. At intermediate levels of adhesion, progressive delamination occurs, which in turn produces a high impact energy absorption.

Yeung and Broutman [71] have shown that a correlation exists between the impact energy and ILSS of a composite laminate (Figure 4.78). Different coupling agents were used on E-glass woven fabrics to achieve various ILSSs in short-beam shear tests. It was observed that the fracture initiation energy increases modestly with increasing ILSS. However, the fracture propagation energy as well as the total impact energy decrease with increasing ILSS, exhibit a minimum, and appear to level off to intermediate values. The principal failure mode at low ILSSs was delamination. At very high ILSSs, fiber failure was predominant.

The strain energy contribution from the matrix in the development of impact energy is negligible. However, the matrix can influence the impact damage mechanism since delamination, debonding, and fiber pullout energies depend on the fiber–matrix interfacial shear strength. Since epoxies have better

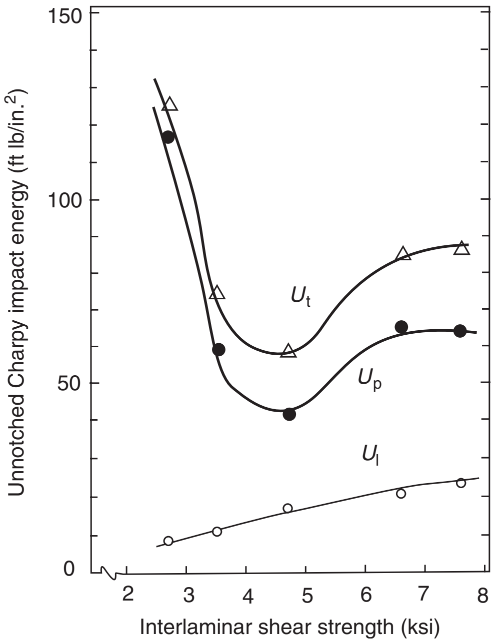

FIGURE 4.78 Variation of unnotched Charpy impact energy with interlaminar shear strength in E-glass fabric–polyester laminates. (After Yeung, P. and Broutman, L.J., *Polym. Eng. Sci.*, 18, 62, 1978.)

adhesion with E-glass fibers than polyesters, E-glass–epoxy composites exhibit higher impact energies than E-glass–polyester composites when the failure mode is a combination of fiber failure and delamination.

In unidirectional composites, the greatest impact energy is exhibited when the fibers are oriented in the direction of the maximum stress, that is, at 0° fiber orientation. Any variation from this orientation reduces the load-carrying capacity as well as the impact energy of the composite laminate. Figure 4.79 shows an example of the effect of fiber orientation on the drop-weight impact energy of $[0/90/0_4/0]_S$ and $[(0/90)_3/0]_S$ laminates [72]. In both cases, a minimum impact energy was observed at an intermediate angle between $\theta = 0°$ and 90°. Furthermore, fracture in off-axis specimens took place principally by interfiber cleavage parallel to the fiber direction in each layer.

The most efficient way of improving the impact energy of a low strain-to-failure fiber composite is to hybridize it with high strain-to-failure fiber laminas. For example, consider the GY-70 carbon fiber composite in Table 4.12 that exhibits a brittle failure mode and a low impact energy. Mallick and Broutman [67] have shown that a hybrid sandwich composite containing GY-70 fiber laminas in the outer skins and E-glass fiber laminas in the core has

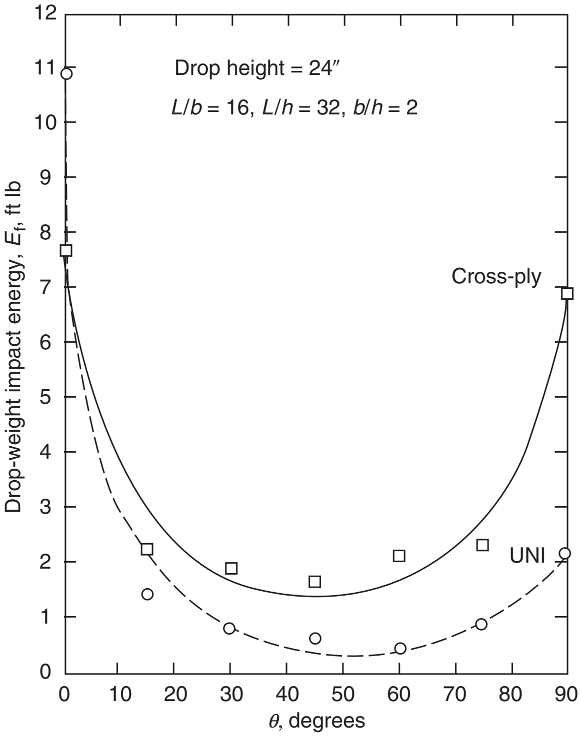

FIGURE 4.79 Variation of drop-weight impact energy with fiber orientation angle. (After Mallick, P.K. and Broutman, L.J., *Eng. Fracture Mech.*, 8, 631, 1976.)

a 35 times higher impact energy than the GY-70 fiber composite. This is achieved without much sacrifice in either the flexural strength or the flexural modulus. The improvement in impact energy is due to delamination at the GY-70/E-glass interface, which occurs after the GY-70 skin on the tension side has failed. Even after the GY-70 skin sheds owing to complete delamination, the E-glass laminas continue to withstand higher stresses, preventing brittle failure of the whole structure. By varying the lamination configuration as well as the fiber combinations, a variety of impact properties can be obtained (Table 4.13). Furthermore, the impact energy of a hybrid composite can be varied by controlling the ratio of various fiber volume fractions (Figure 4.80).

4.3.4 Low-Energy Impact Tests

Low-energy impact tests are performed to study localized damage without destroying the specimen. Two types of low-energy impact tests are performed, namely, the ballistic impact test and the low-velocity drop-weight impact test. In ballistic impact tests, the specimen surface is impinged with very low

TABLE 4.13
Unnotched Charpy Impact Energies of Various Interply Hybrid Laminates

Laminate	Impact Energy, kJ/m^2 (ft lb/in.^{2})		
	U_i	U_p	U_t
GY-70/E-glass: $(0_{5G}/0_{5E})_S$[a]	6.7 (3.2)	419.6 (199.8)	426.3 (203)
T-300/E-glass: $(0_{5T}/0_{5E})_S$[a]	60.3 (28.7)	374.4 (178.3)	434.7 (207)
GY-70/Kevlar 49: $(0_{5G}/0_{5K})_S$[a]	7.3 (3.5)	86.9 (41.4)	94.2 (44.9)
GY-70/E-glass: $[(0_G/0_E)_5/0_G]_S$[a]	13.9 (6.6)	204 (97.2)	217.9 (103.8)
T-300/E-glass: $[(0_T/0_E)_5/0_T]_S$[a]	59.4 (28.3)	80.2 (38.2)	139.6 (66.5)
Modmor II carbon/E-glass:[b] $[(0_E/(45/90/0/-45)_M)_7/0_E/(45/90)_M]_S$	29.4 (14)	264.8 (126)	294.2 (140)
For comparison: All Modmor II carbon:[b] $[(0/45/90/0/-45)_7/0/45/90]_S$	27.3 (13)	56.8 (27)	84.1 (40)

[a] From P.K. Mallick and L.J. Broutman, *J. Test. Eval.*, 5, 190, 1977.
[b] From J.L. Perry and D.F. Adams, *Composites*, 7, 166, 1975.

mass spherical balls at high speeds. In low-velocity drop-weight impact tests, a relatively heavier weight or ball is dropped from small heights onto the specimen surface. After the impact test, the specimen is visually as well as nondestructively inspected for internal and surface damages and then tested

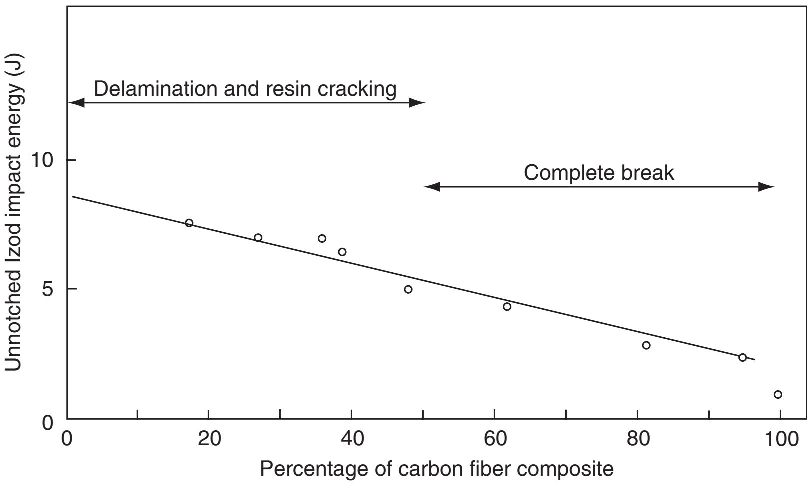

FIGURE 4.80 Effect of carbon fiber content on the unnotched Izod impact energy of 0° carbon/E-glass–epoxy interply hybrid laminates. (After Hancox, N.L. and Wells, H., The Izod impact properties of carbon fibre/glass fibre sandwich structures, U.K. Atomic Energy Research Establishment Report AERE-R7016, 1972.)

in static tension or compression modes to determine its postimpact residual properties.

Sidey and Bradshaw [73] performed ballistic impact experiments on both unidirectional 0° and $[(0/90)]_{2S}$ carbon fiber–epoxy composites. Steel balls, 3 mm in diameter, were impacted on 3 mm thick rectangular specimens. The impact velocity ranged from 70 to 300 m/s. Failure mode in unidirectional composites was longitudinal splitting (through-the-thickness cracks running parallel to the fibers) and subsurface delamination. In cross-ply laminates, the 90° layers prevented the longitudinal cracks from running through the thickness and restricted them to the surface layers only. Delamination was more pronounced with untreated fibers.

Rhodes et al. [74] performed similar ballistic impact experiments on carbon fiber–epoxy composites containing various arrangements of 0°, 90°, and ±45° laminas. Aluminum balls, 12.7 mm in diameter, were impacted on 5–8 mm thick rectangular specimens at impact velocities ranging from 35 to 125 m/s. Their experiments showed that, over a threshold velocity, appreciable internal damage appeared in the impacted area even though the surfaces remained undamaged. The principal internal damage was delamination, which was pronounced at interfaces between 0° and 90° or 0° and 45° laminas. The damaged specimens exhibited lower values of critical buckling loads and strains than the unimpacted specimens.

Ramkumar [75] studied the effects of low-velocity drop-weight impact tests on the static and fatigue strengths of two multidirectional AS carbon fiber–epoxy composites. His experiments indicate that impact-induced delaminations, with or without visible surface damages, can severely reduce the static compressive strengths. Static tensile strengths were affected only if delaminations were accompanied with surface cracks. Fatigue strengths at 10^6 cycles were reduced considerably more in compression–compression and tension–compression fatigue tests than in tension–tension fatigue tests. The growth of impact-induced delaminations toward the free edges was the predominant failure mechanism in these fatigue tests.

Morton and Godwin [76] compared the low-velocity impact damage in carbon fiber-reinforced $[0_2/\pm45]_{2S}$ and $[\pm45/0_3/\pm45/0]_S$ laminates containing either a toughened epoxy or PEEK as the matrix. They observed that the incident impact energy level to produce barely visible impact damage was approximately equal for both toughened epoxy and PEEK composites; however, energy to produce perforation was significantly higher in PEEK composites. Nondestructive inspection of impacted laminates showed that the PEEK laminates had less damage at or near perforation energy. Both epoxy and PEEK laminates showed matrix cracking and ply delamination, but the latter also exhibited local permanent deformation. Morton and Godwin [76] also observed that the stacking sequence with 45° fibers in the outside layers provided a higher residual strength after low-energy impact than that with 0° layers in the outside layers.

4.3.5 Residual Strength After Impact

If a composite laminate does not completely fail by impact loading, it may still be able to carry loads even though it has sustained internal as well as surface damages. The load-carrying capacity of an impact-damaged laminate is measured by testing it for residual strength in a uniaxial tension test.

The postimpact residual strength as well as the damage growth with increasing impact velocity is shown schematically in Figure 4.81. For small impact velocities, no strength degradation is observed (region I). As the damage appears, the residual tensile strength is reduced with increasing impact velocity (region II) until a minimum value is reached just before complete perforation (region III). Higher impact velocities produce complete perforation, and the hole diameter becomes practically independent of impact velocity (region IV). The residual strength in this region remains constant and is equal to the notched tensile strength of the laminate containing a hole of the same diameter as the impacting ball. Husman et al. [77] proposed the following relationship between the residual tensile strength in region II and the input kinetic energy:

$$\sigma_{\mathrm{R}} = \sigma_{\mathrm{U}} \sqrt{\frac{U_{\mathrm{s}} - kU_{\mathrm{KE}}}{U_{\mathrm{s}}}}, \qquad (4.39)$$

where

σ_{R} = residual tensile strength after impact
σ_{U} = tensile strength of an undamaged laminate

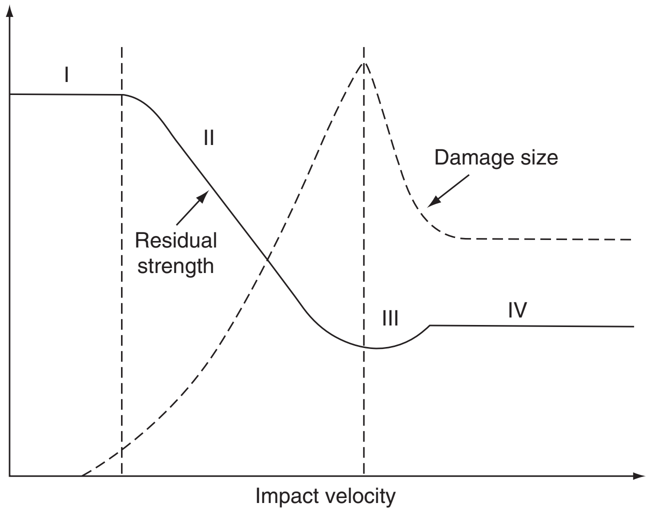

FIGURE 4.81 Schematic representation of the residual static strength in impact-damaged laminates. (After Awerbuch, J. and Hahn, H.T., *J. Compos. Mater.*, 10, 231, 1976.)

U_s = area under the stress–strain curve for an undamaged laminate

U_{KE} = input kinetic energy per unit laminate thickness

k = a constant that depends on the laminate stacking sequence and boundary conditions (e.g., one end fixed vs. both ends fixed)

Two experiments are required to determine the value of k, namely, a static tension test on an undamaged specimen and a static tension test on an impact-damaged specimen. Knowing the preimpact kinetic energy, the value of k can be calculated using Equation 4.39. Although the value of k is not significantly affected by the laminate thickness, it becomes independent of laminate width only for wide specimens. Residual strength measurements on $[0/90]_{3S}$ laminates of various fiber–matrix combinations have shown reasonable agreement with Equation 4.39.

4.3.6 Compression-After-Impact Test

The compression-after-impact test is used for assessing the nonvisible or barely visible impact damage in composite laminates. An edge-supported quasi-isotropic laminated plate, 153 mm × 102 mm × 3–5 mm thick, is impacted at the center with an energy level of 6.7 J/mm (1500 in. lb/in.). After nondestructively examining the extent of impact damage (e.g., by ultrasonic C-scan), the plate is compression-tested in a fixture with antibuckling guides (Figure 4.82).

The compressive strength of an impact-damaged laminate is lower than the undamaged compressive strength. Failure modes observed in compression-after-impact tests are shear crippling of fibers and ply delamination. In brittle epoxy laminates, delamination is the predominant failure mode, while in toughened epoxy matrix composites, significant shear crippling occurs before failure by ply delamination.

Postimpact compressive strength (PICS) of a laminate can be improved by reducing the impact-induced delamination. One way of achieving this is by increasing the interlaminar fracture toughness of the laminate. Figure 4.83 shows that the PICS of carbon fiber-reinforced laminates increases considerably

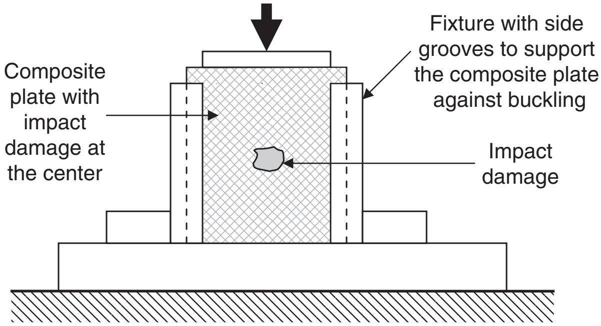

FIGURE 4.82 Test fixture for compression test after impact.

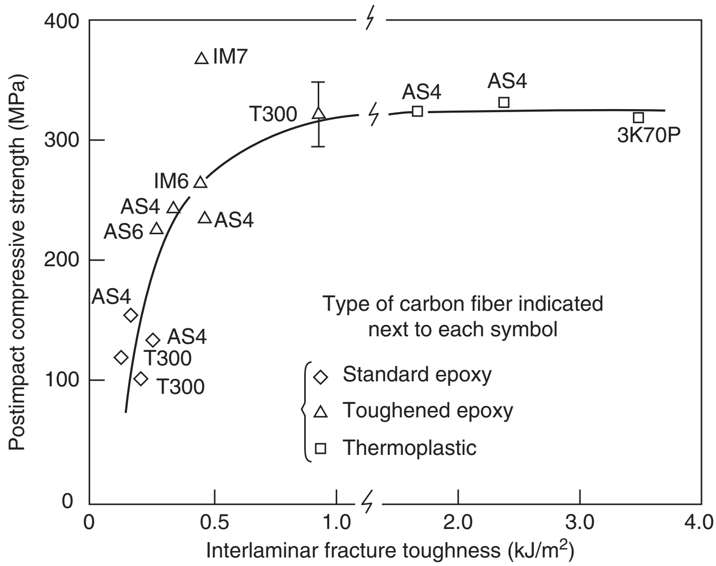

FIGURE 4.83 Postimpact compressive strength of carbon fiber-reinforced laminates as a function of their interlaminar fracture toughness (impact energy = 6.7 J/mm). (Adapted from Leach, D., Tough and damage tolerant composites, *Symposium on Damage Development and Failure Mechanisms in Composite Materials*, Leuven, Belgium, 1987.)

when their interlaminar fracture toughness is increased from 200 to 500 J/m^2; however, above 1000 J/m^2, PICS is nearly independent of the interlaminar fracture toughness. In this case, higher interlaminar fracture toughness was obtained by increasing the fracture toughness of the matrix either by toughening it or by changing the matrix from the standard epoxy to a thermoplastic. Other methods of increasing the interlaminar fracture toughness and reducing ply delamination are discussed in Section 4.7.3.

4.4 OTHER PROPERTIES

4.4.1 PIN-BEARING STRENGTH

Pin-bearing strength is an important design parameter for bolted joints and has been studied by a number of investigators. It is obtained by tension testing a pin-loaded hole in a flat specimen (Figure 4.84). The failure mode in pin-bearing tests depends on a number of geometric variables [78]. Generally, at low w/d ratios, the failure is by net tension with cracks originating at the hole boundary, and at low e/d ratios, the failure is by shear-out. The load-carrying capacity of the laminate is low if either of these failure modes occurs instead of bearing failure.

For bearing failure, relatively high values of w/d and e/d ratios are required. The minimum values of w/d and e/d ratios needed to develop full bearing

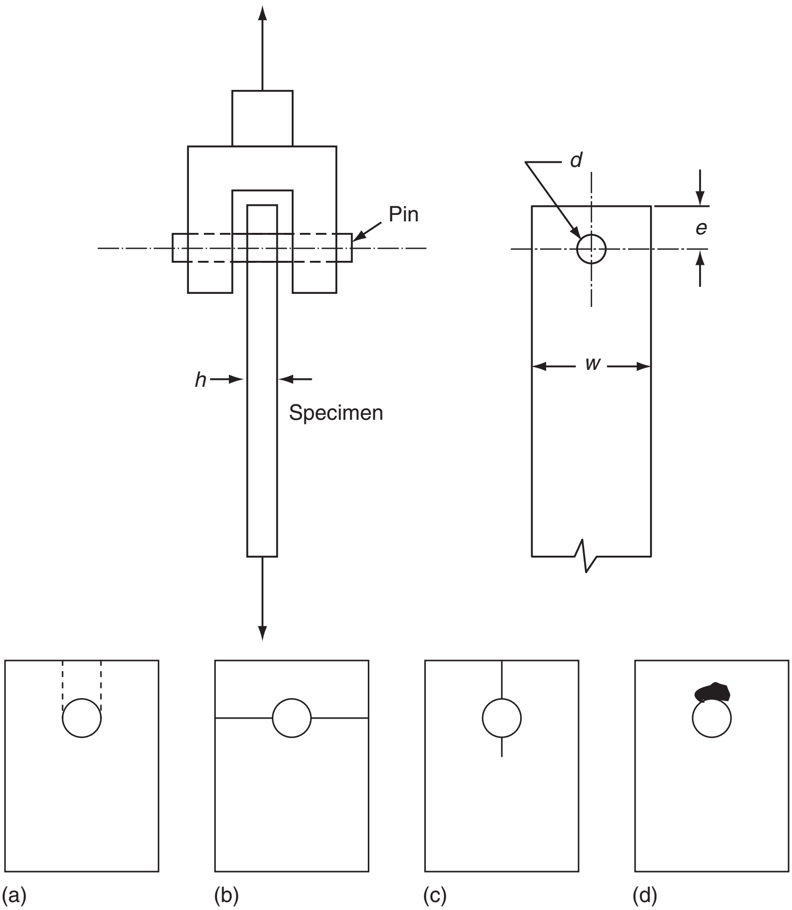

FIGURE 4.84 Pin-bearing test and various failure modes: (a) shear-out, (b) net tension, (c) cleavage, and (d) bearing failure (accompanied by hole elongation).

strength depend on the material and fiber orientation as well as on the stacking sequence. Another geometric variable controlling the bearing strength is the d/h ratio of the specimen. In general, bearing strength is decreased at higher d/h ratios, and a tendency toward shear failure is observed at low d/h ratios. A d/h ratio between 1 and 1.2 is recommended for developing the full bearing strength. A few representative pin-bearing strengths are given in Table 4.14.

For 0° laminates, failure in pin-bearing tests occurs by longitudinal splitting, since such laminates have poor resistance to in-plane transverse stresses at the loaded hole. The bearing stress at failure for 0° laminates is also quite low. Inclusion of 90° layers [79], ±45° layers, or ±60° layers [80] at or near the surfaces improves the bearing strength significantly. However, $[\pm 45]_S$, $[\pm 60]_S$, or $[90/\pm 45]_S$ laminates have lower bearing strengths than $[0/\pm 45]_S$ and $[0/\pm 60]_S$

TABLE 4.14
Representative Pin-Bearing Strength of Various Laminates

Laminates	Tightening Torque, N m (in. lb)	e/d	Pin-Bearing Strength, MPa (ksi)	References
E-glass–vinyl ester SMC-R50	0	3	325 (47.1)	[79]
E-glass–vinyl ester SMC-C40R30	0	3	400 (58)	[79]
E-glass–epoxy				
$[0/90]_S$	1.85 (16.4)	6	600 (87)	[78]
$[0/\pm45]_S$	1.85 (16.4)	4.5	725 (105.1)	[78]
$[\pm45]_S$	1.85 (16.4)	5	720 (104.4)	[78]
HTS carbon–epoxy				
$[0/90]_S$	3.40 (30.2)	6	800 (116)	[80]
$[0/\pm45]_S$	3.40 (30.2)	3	900 (130)	[80]
$[\pm45]_S$	3.40 (30.2)	5	820 (118.9)	[80]

laminates. A number of other observations on the pin-bearing strength of composite laminates are listed as follows.

1. Stacking sequence has a significant influence on the pin-bearing strength of composite laminates. Quinn and Matthews [81] have shown that a $[90/\pm45/0]_S$ layup is nearly 30% stronger in pin-bearing tests than a $[0/90/\pm45]_S$ layup.
2. The number of $\pm\theta$ layers present in a $[0/\pm\theta]_S$ laminate has a great effect on its pin-bearing strength. Collings [80] has shown that a $[0/\pm45]_S$ laminate attains its maximum pin-bearing strength when the ratio of 0° and 45° layers is 60:40.
3. Fiber type is an important material parameter for developing high pin-bearing strength in $[0/\pm\theta]_S$ laminates. Kretsis and Matthews [78] have shown that for the same specimen geometry, the bearing strength of a $[0/\pm45]_S$ carbon fiber-reinforced epoxy laminate is nearly 20% higher than a $[0/\pm45]_S$ E-glass fiber-reinforced epoxy.
4. The pin-bearing strength of a composite laminate can be increased significantly by adhesively bonding a metal insert (preferably an aluminum insert) at the hole boundary [82].
5. Lateral clamping pressure distributed around the hole by washers can significantly increase the pin-bearing strength of a laminate [83]. The increase is attributed to the lateral restraint provided by the washers as well as frictional resistance against slip. The lateral restraint contains the shear cracks developed at the hole boundary within the washer perimeter and allows the delamination to spread over a wider area before final failure occurs. The increase in pin-bearing strength levels off at high clamping pressure. If the clamping pressure is too high, causing the washers to dig into the laminate, the pin-bearing strength may decrease.

4.4.2 DAMPING PROPERTIES

The damping property of a material represents its capacity to reduce the transmission of vibration caused by mechanical disturbances to a structure. The measure of damping of a material is its damping factor η. A high value of η is desirable for reducing the resonance amplitude of vibration in a structure. Table 4.15 compares the typical damping factors for a number of materials. Fiber-reinforced composites, in general, have a higher damping factor than metals. However, its value depends on a number of factors, including fiber and resin types, fiber orientation angle, and stacking sequence.

4.4.3 COEFFICIENT OF THERMAL EXPANSION

The coefficient of thermal expansion (CTE) represents the change in unit length of a material due to unit temperature rise or drop. Its value is used for calculating dimensional changes as well as thermal stresses caused by temperature variation.

The CTE of unreinforced polymers is higher than that of metals. The addition of fibers to a polymer matrix generally lowers its CTE. Depending on the fiber type, orientation, and fiber volume fraction, the CTE of fiber-reinforced polymers can vary over a wide range of values. In unidirectional 0° laminates, the longitudinal CTE, α_{11}, reflects the fiber characteristics. Thus, both carbon and Kevlar 49 fibers produce a negative CTE, and glass and boron fibers produce a positive CTE in the longitudinal direction. As in the case of elastic properties, the CTEs for unidirectional 0° laminates are different in longitudinal and transverse directions (Table 4.16). Compared with carbon fiber-reinforced epoxies, Kevlar 49 fiber-reinforced epoxies exhibit a greater anisotropy in their CTE due to greater anisotropy in the CTE of Kevlar 49

TABLE 4.15
Representative Damping Factors of Various Polymeric Laminates

Material	Fiber Orientation	Modulus (10^6 psi)	Damping Factor η
Mild steel	—	28	0.0017
6061 Al alloy	—	10	0.0009
E-glass–epoxy	0°	5.1	0.0070
Boron–epoxy	0°	26.8	0.0067
Carbon–epoxy	0°	27.4	0.0157
	22.5°	4.7	0.0164
	90°	1.0	0.0319
	$[0/22.5/45/90]_S$	10.0	0.0201

Source: Adapted from Friend, C.A., Poesch, J.G., and Leslie, J.C., Graphite fiber composites fill engineering needs, *Proceedings 27th Annual Technical Conference*, Society of the Plastics Industry, 1972.

TABLE 4.16
Coefficients of Thermal Expansion of Various Laminates[a]

Material	Coefficient of Thermal Expansion, 10^{-6} m/m per °C (10^{-6} in./in. per °F)		
	Unidirectional (0°)		
	Longitudinal	Transverse	Quasi-Isotropic
S-glass–epoxy	6.3 (3.5)	19.8 (11)	10.8 (6)
Kevlar 49–epoxy	−3.6 (−2)	54 (30)	−0.9 to 0.9 (−0.5 to 0.5)
Carbon–epoxy			
High-modulus carbon	−0.9 (−0.5)	27 (15)	0 to 0.9 (0 to 0.5)
Ultrahigh-modulus carbon	−1.44 (−0.8)	30.6 (17)	−0.9 to 0.9 (−0.5 to 0.5)
Boron–epoxy	4.5 (2.5)	14.4 (8)	3.6 to 5.4 (2 to 3)
Aluminum		21.6 to 25.2 (12 to 14)	
Steel		10.8 to 18 (6 to 10)	
Epoxy		54 to 90 (30 to 50)	

Source: Adapted from Freeman, W.T. and Kuebeler, G.C., *Composite Materials: Testing and Design* (*Third Conference*), *ASTM STP*, 546, 435, 1974.

[a] The fiber content in all composite laminates is 60% by volume.

TABLE 4.17
Coefficients of Thermal Expansion of Various E-Glass–Epoxy Laminates

Laminate	Fiber Volume Fraction (%)	Direction of Measurement	Coefficient of Thermal Expansion, 10^{-6} m/m per °C (10^{-6} in./in. per °F)
Unidirectional	63	0°	7.13 (3.96)
		15°	9.45 (5.25)
		30°	13.23 (7.35)
		45°	30.65 (12.08)
		60°	30.65 (17.03)
		75°	31.57 (17.54)
		90°	32.63 (18.13)
$[\pm 30/90]_{7S}$	60	In-plane	15.66 (8.7)
$[(0/90/)_9/(\pm 45)_2]_S$	71	In-plane	12.6 (7.0)

Source: Adapted from Raghava, R., *Polym. Compos.*, 5, 173, 1984.

fibers [84]. The anisotropic nature of the CTE of a unidirectional laminate is further demonstrated in Table 4.17.

In quasi-isotropic laminates as well as randomly oriented discontinuous fiber laminates, the CTEs are equal in all directions in the plane of the laminate. Furthermore, with proper fiber type and lamination configuration, CTE in the plane of the laminate can be made close to zero. An example is shown in Figure 4.85, in which the proportions of fibers in 0°, 90°, and ±45° layers

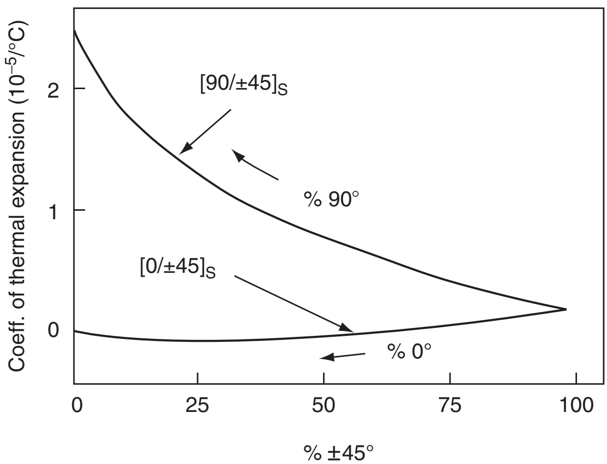

FIGURE 4.85 Coefficients of thermal expansion of $[0/\pm 45]_S$ and $[90/\pm 45]_S$ carbon fiber-epoxy laminates. (After Parker, S.F.H., Chandra, M., Yates, B., Dootson, M., and Walters, B.J., *Composites*, 12, 281, 1981.)

were controlled to obtain a variety of CTEs in the $[0/\pm45]_S$ and $[90/\pm45]_S$ laminates [85].

4.4.4 Thermal Conductivity

The thermal conductivity of a material represents its capacity to conduct heat. Polymers in general have low thermal conductivities, which make them useful as insulating materials. However, in some circumstances, they may also act as a heat sink with little ability to dissipate heat efficiently. As a result, there may be a temperature rise within the material.

The thermal conductivity of a fiber-reinforced polymer depends on the fiber type, orientation, fiber volume fraction, and lamination configuration. A few representative values are shown in Table 4.18. With the exception of carbon fibers, fiber-reinforced polymers in general have low thermal conductivities. Carbon fiber-reinforced polymers possess relatively high thermal conductivities due to the highly conductive nature of carbon fibers. For unidirectional 0° composites, the longitudinal thermal conductivity is controlled by the fibers and the transverse thermal conductivity is controlled by the matrix. This is reflected in widely different values of thermal conductivities in these two directions.

The electrical conductivities of fiber-reinforced polymers are similar in nature to their thermal counterparts. For example, E-glass fiber-reinforced polymers are poor electrical conductors and tend to accumulate static electricity. For protection against static charge buildup and the resulting electromagnetic interference (EMI) or radio frequency interference (RFI), small quantities of conductive fibers, such as carbon fibers, aluminum flakes, or aluminum-coated glass fibers, are added to glass fiber composites.

TABLE 4.18
Thermal Conductivities of Various Composite Laminates

	Thermal Conductivity, W/m per °C (Btu/h ft per °F)		
	Unidirectional (0°)		
Material	**Longitudinal**	**Transverse**	**Quasi-Isotropic**
S-glass–epoxy	3.46 (2)	0.35 (0.2)	0.346 (0.2)
Kevlar 49–epoxy	1.73 (1)	0.173 (0.1)	0.173 (0.1)
Carbon–epoxy			
High modulus	48.44–60.55 (28–35)	0.865 (0.5)	10.38–20.76 (6–12)
Ultrahigh modulus	121.1–29.75 (70–75)	1.04 (0.6)	24.22–31.14 (14–18)
Boron–epoxy	1.73 (1)	1.04 (0.6)	1.384 (0.8)
Aluminum		138.4–216.25 (80–125)	
Steel		15.57–46.71 (9–27)	
Epoxy		0.346 (0.2)	

Source: Adapted from Freeman, W.T. and Kuebeler, G.C., *Composite Materials: Testing and Design* (*Third Conference*), *ASTM STP*, 546, 435, 1974.

4.5 ENVIRONMENTAL EFFECTS

The influence of environmental factors, such as elevated temperatures, high humidity, corrosive fluids, and ultraviolet (UV) rays, on the performance of polymer matrix composites is of concern in many applications. These environmental conditions may cause degradation in the mechanical and physical properties of a fiber-reinforced polymer because of one or more of the following reasons:

1. Physical and chemical degradation of the polymer matrix, for example, reduction in modulus due to increasing temperature, volumetric expansion due to moisture absorption, and scission or alteration of polymer molecules due to chemical attack or ultraviolet rays. However, it is important to note that different groups of polymers or even different molecular configurations within the same group of polymers would respond differently to the same environment.
2. Loss of adhesion or debonding at the fiber–matrix interface, which may be followed by diffusion of water or other fluids into this area. In turn, this may cause a reduction in fiber strength due to stress corrosion. Many experimental studies have shown that compatible coupling agents are capable of either slowing down or preventing the debonding process even under severe environmental conditions, such as exposure to boiling water.
3. Reduction in fiber strength and modulus. For a short-term or intermittent temperature rise up to 150°C–300°C, reduction in the properties of most commercial fibers is insignificant. However, depending on the fiber type, other environmental conditions may cause deterioration in fiber properties. For example, moisture is known to accelerate the static fatigue in glass fibers. Kevlar 49 fibers are capable of absorbing moisture from the environment, which reduces its tensile strength and modulus. The tensile strength of Kevlar 49 fibers is also reduced with direct exposure to ultraviolet rays.

In this section, we consider the effect of elevated temperature and high humidity on the performance of composite laminates containing polymer matrix.

4.5.1 Elevated Temperature

When a polymer specimen is tension-tested at elevated temperatures, its modulus and strength decrease with increasing temperature because of thermal softening. In a polymeric matrix composite, the matrix-dominated properties are more affected by increasing temperature than the fiber-dominated properties. For example, the longitudinal strength and modulus of a unidirectional 0° laminate remain virtually unaltered with increasing temperature, but its transverse and off-axis properties are significantly reduced as the temperature approaches the T_g of the polymer. For a randomly oriented discontinuous fiber composite, strength and modulus are reduced in all directions. Reductions in modulus as a function of increasing test temperature are shown for unidirectional continuous and randomly oriented discontinuous fiber laminates in Figures 4.86 and 4.87, respectively.

Thermal aging due to long-term exposure to elevated temperatures without load can cause deterioration in the properties of a polymer matrix composite. Kerr and Haskins [86] reported the effects of 100–50,000 h of thermal aging on the tensile strength of AS carbon fiber–epoxy and HTS carbon fiber–polyimide unidirectional and cross-ply laminates. For the AS carbon–epoxy systems, thermal aging at 121°C produced no degradation for the first 10,000 h. Matrix degradation began between 10,000 and 25,000 h and was severe after 50,000 h. After 5000 h, the matrix was severely embrittled. Longitudinal tensile strength was considerably reduced for aging times of 5000 h or longer. The HTS carbon–polyimide systems were aged at higher temperatures but showed less degradation than the AS carbon–epoxy systems.

Devine [87] reported the effects of thermal aging on the flexural strength retention in SMC-R laminates containing four different thermoset polyester resins and a vinyl ester resin. At 130°C, all SMC-R laminates retained >80% of their respective room temperature flexural strengths even after thermal aging for 12 months. At 180°C, all SMC-R laminates showed deterioration;

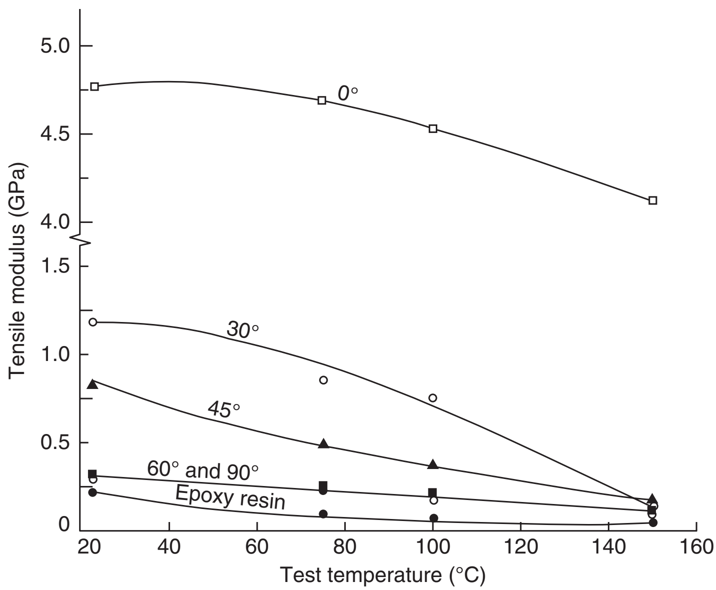

FIGURE 4.86 Effect of increasing test temperature on the static tensile modulus of unidirectional E-glass–epoxy laminates. (After Marom, G. and Broutman, L.J., *J. Adhes*., 12, 153, 1981.)

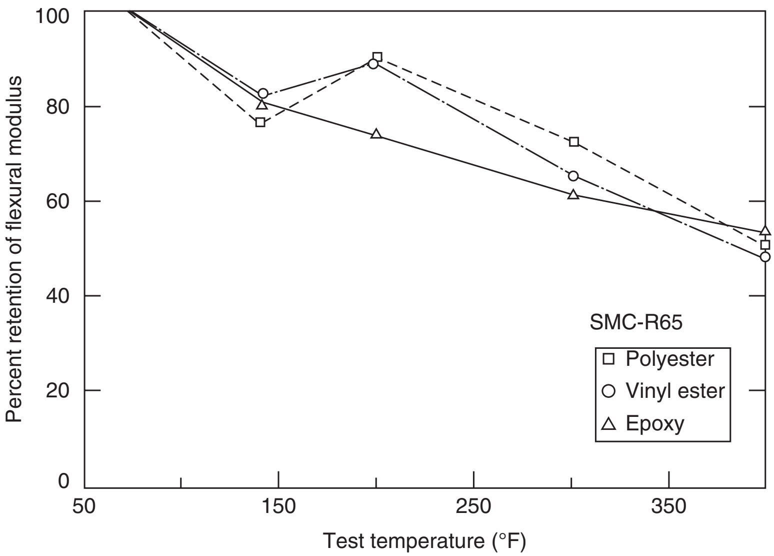

FIGURE 4.87 Effect of increasing test temperature on the static flexural modulus of E-glass-SMC-R65 laminates. (After Mallick, P.K., *Polym. Compos.*, 2, 18, 1981.)

however, vinyl ester laminates had higher strength retention than all polyester laminates.

The concern for the reduction in mechanical properties of thermoplastic matrix composites at elevated temperatures is more than the thermoset matrix composites, since the properties of thermoplastic polymers reduce significantly at or slightly above their glass transition temperatures. As in thermoset matrix composites, the effect of increasing temperature is more pronounced for matrix-dominated properties than for fiber-dominated properties (Figure 4.88).

4.5.2 Moisture

When exposed to humid air or water environments, many polymer matrix composites absorb moisture by instantaneous surface absorption followed by diffusion through the matrix. Analysis of moisture absorption data for epoxy and polyester matrix composites shows that the moisture concentration increases initially with time and approaches an equilibrium (saturation) level after several days of exposure to humid environment (Figure 4.89). The rate at which the composite laminate attains the equilibrium moisture concentration is determined by its thickness as well as the ambient temperature. On drying, the moisture concentration is continually reduced until the composite laminate returns to the original as-dry state. In general, the rate of desorption is higher than the rate of absorption, although for the purposes of analysis they are assumed to be equal.

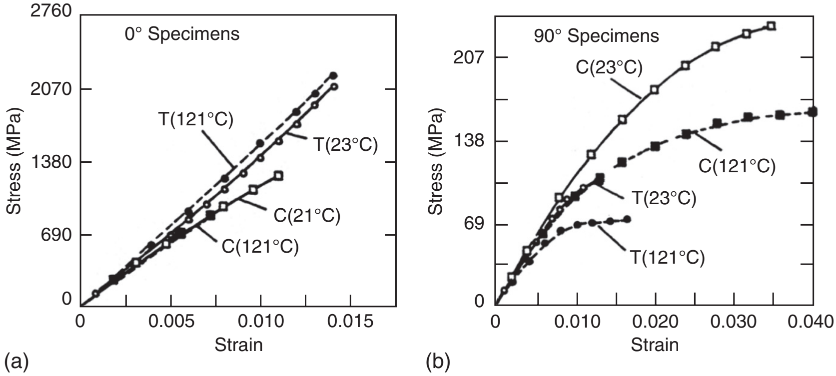

FIGURE 4.88 Tensile (T) and compressive (C) stress–strain diagrams of 0° and 90° carbon fiber-reinforced PEEK laminates at 23°C and 121°C. (After Fisher, J.M., Palazotto, A.N., and Sandhu, R.S., *J. Compos. Technol. Res.*, 13, 152, 1991.)

4.5.2.1 Moisture Concentration

The moisture concentration M, averaged over the thickness, of a composite laminate at any time during its exposure to humid environment at a given temperature can be calculated from the following equation [88]:

$$M = M_i + G(M_m - M_i), \tag{4.40}$$

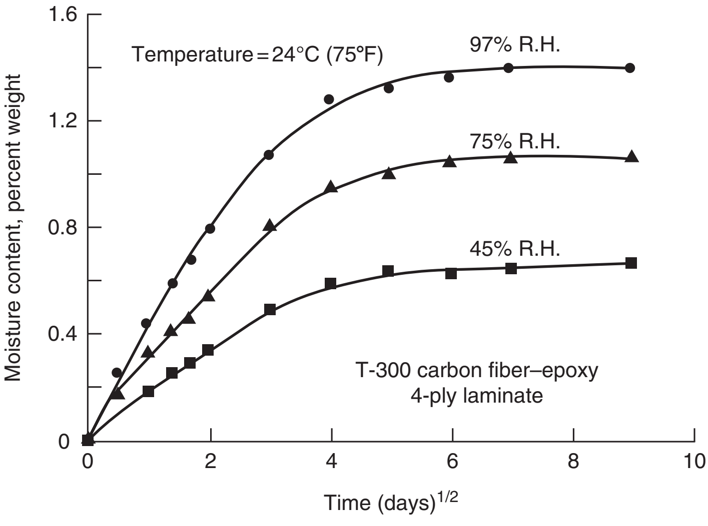

FIGURE 4.89 Moisture absorption in a carbon–epoxy laminate at 24°C (75°F). (After Shen, C.H. and Springer, G.S., *J. Compos. Mater.*, 10, 2, 1976.)

where

M_i = initial moisture concentration, which is equal to zero if the material is completely dried

M_m = equilibrium (maximum) moisture concentration in the saturated condition

G = time-dependent dimensionless parameter related to the diffusion coefficient of the material

For a material immersed in water, the equilibrium moisture concentration M_m is a constant. If the material is exposed to humid air, the equilibrium moisture concentration M_m increases with increasing relative humidity of the surrounding air (Table 4.19); however, it is found that M_m is relatively insensitive to the ambient temperature. For the humid air environment, M_m is expressed as

$$M_m = A(\mathrm{RH})^B, \tag{4.41}$$

where RH is the relative humidity (percent) of the surrounding air, and A and B are constants that depend primarily on the type of polymer; the exponent B has a value between 1 and 2.

Assuming a Fickian diffusion through the laminate thickness, the time-dependent parameter G can be approximated as

$$G \approx 1 - \frac{8}{\pi^2} \exp\left(-\frac{\pi^2 D_z t}{c^2}\right), \tag{4.42}$$

TABLE 4.19
Equilibrium Moisture Content in Various Composite Laminates

Material	Laminate	RH (%)	Temperature (°C)	M_m (%)
T-300 carbon–epoxy[a] (v_f = 68%)	Unidirectional (0°) and quasi-isotropic	50	23	0.35
		75	23	0.7875
		100	23	1.4
		Fully submerged in water	23	1.8
E-glass–polyester[b] (w_f = 50%)	SMC-R50	50	23	0.10
		100	23	1.35
E-glass–vinyl ester[b] (w_f = 50%)	SMC-R50	50	23	0.13
		100	23	0.63

[a] Adapted from C.H. Shen and G.S. Springer, *J. Composite Matls.*, 10, 2, 1976.

[b] Adapted from G.S. Springer, B.A. Sanders and R.W. Tung, *J. Composite Matls.*, 14, 213, 1980.

where

D_z = diffusion coefficient (mm^2/s) of the material in the direction normal to the surface (moisture diffusion is in the thickness direction)

c = laminate thickness h if both sides of the laminate are exposed to humid environment; for exposure on one side, $c = 2h$

t = time (s)

Equation 4.42 is valid at sufficiently large values of t. For shorter times, the average moisture concentration increases linearly with $t^{1/2}$, and the parameter G can be approximated as

$$G = 4\left(\frac{D_z t}{\pi c^2}\right)^{1/2}. \tag{4.43}$$

The diffusion coefficient D_z is related to the matrix diffusion coefficient D_m by the following equation:

$$D_z = D_{11}\cos^2\phi + D_{22}\sin^2\phi, \tag{4.44}$$

where

$$\left.\begin{aligned} D_{11} &= D_m(1 - v_f) \\ D_{12} &= D_m\left(1 - 2\sqrt{\frac{v_f}{\pi}}\right) \end{aligned}\right\} \text{Assuming fiber diffusivity } (D_f) \ll \text{matrix diffusivity } (D_m)$$

ϕ = fiber angle with the z direction ($\phi = 90°$ for fibers parallel to the laminate surface)

v_f = fiber volume fraction

Equations 4.40 through 4.44 can be used to estimate the moisture concentration in a polymer matrix composite. However, the following internal and external parameters may cause deviations from the calculated moisture concentrations.

Void content: The presence of voids has a dramatic effect on increasing the equilibrium moisture concentration as well as the diffusion coefficient.

Fiber type: Equation 4.44 assumes that the fiber diffusivity is negligible compared with the matrix diffusivity. This assumption is valid for glass, carbon, and boron fibers. However, Kevlar 49 fibers are capable of absorbing and diffusing significant amounts of moisture from the environment. As a result, Kevlar 49 fiber-reinforced composites absorb much more moisture than other composites.

Resin type: Moisture absorption in a resin depends on its chemical structure and the curing agent as well as the degree of cure. Analysis of the water absorption data of various epoxy resin compositions shows that the weight gain due to water absorption may differ by a factor of 10 or more between different resin chemical structures and by a factor of 3 or more for the same resin that has different curing formulations [90]. For many resin systems,

TABLE 4.20
Diffusion Coefficients for Absorption and Desorption in an Epoxy Resin at 100% Relative Humidity

Temperature (°C)	Diffusion Coefficient (10^{-8} mm^2/s) Absorption	Desorption
0.2	3	3
25	21	17
37	41	40
50	102	88
60	179	152
70	316	282
80	411	489
90	630	661

Source: After Wright, W.W., *Composites*, 12, 201, 1981.

the water absorption process may continue for a long time and equilibrium may not be attained for months or even years.

Temperature: Moisture diffusion in a polymer is an energy-activated process, and the diffusion coefficient depends strongly on the temperature (Table 4.20). In general, the temperature dependence can be predicted from an Arrhenius-type equation:

$$D_z = D_{z0} \exp\left(-\frac{E}{RT}\right), \tag{4.45}$$

where
E = activation energy (cal/g mol)
R = universal gas constant = 1.987 cal/(g mol K)
T = absolute temperature (K)
D_{z0} = a constant (mm^2/s)

Stress level: Gillat and Broutman [91] have shown that increasing the applied stress level on a T-300 carbon–epoxy cross-ply laminate produces higher diffusion coefficients but does not influence the equilibrium moisture content. Similar experiments by Marom and Broutman [92] show that the moisture absorption is a function of fiber orientation angle relative to the loading direction. The maximum effect is observed at $\theta = 90°$.

Microcracks: The moisture concentration in a laminate may exceed the equilibrium moisture concentration if microcracks develop in the material. Moisture absorption is accelerated owing to capillary action at the microcracks as well as exposed fiber–matrix interfaces at the laminate edges. On the other hand, there may be an "apparent" reduction in moisture concentration if there is a loss of material from leaching or cracking.

Thermal spikes: Diffusion characteristics of composite laminates may alter significantly if they are rapidly heated to high temperatures followed by rapid cooling to the ambient condition, a process known as thermal spiking. McKague et al. [93] have shown that the moisture absorption in specimens exposed to 75% relative humidity at 24°C and occasional (twice weekly) thermal spikes (rapid heating to 149°C followed by rapid cooling to 24°C) is twice that of specimens not exposed to spikes. Additionally, thermally spiked specimens exhibit a permanent change in their moisture absorption characteristics. The increased diffusion rate and higher moisture absorption are attributed to microcracks formed owing to stress gradients caused by thermal cycling and resin swelling. The service temperature in a spike environment should be limited to the glass transition temperature T_g of the resin, since spike temperatures above T_g cause much higher moisture absorption than those below T_g.

Reverse thermal effect: Adamson [94] has observed that cast-epoxy resins or epoxy-based laminates containing an equilibrium moisture concentration exhibit a rapid rate of moisture absorption when the ambient temperature is reduced. For example, an AS carbon fiber-reinforced epoxy laminate attained an equilibrium moisture concentration of 2.3 wt% after 140 days of exposure at 74°C. When the exposure temperature was reduced to 25°C, the equilibrium moisture concentration increased to 2.6% within 40 days. This inverse temperature dependence of moisture absorption is called the reverse thermal effect.

4.5.2.2 Physical Effects of Moisture Absorption

Moisture absorption produces volumetric changes (swelling) in the resin, which in turn cause dimensional changes in the material. Assuming that the swollen volume of the resin is equal to the volume of absorbed water, the resulting volume change can be computed from the following relationship:

$$\frac{\Delta V(t)}{V_0} = \frac{\rho_m}{\rho_w} M, \tag{4.46}$$

where

ρ_m = matrix density
ρ_w = water density ($\approx$1 kg/mm^3)
M = moisture content at time t

The corresponding dilatational (volumetric) strain in the resin is

$$\varepsilon_m = \frac{1}{3}\frac{\Delta V}{V_0} = \frac{1}{3}\frac{\rho_m}{\rho_w} M = \beta_m M, \tag{4.47}$$

where

$\beta_m = \frac{1}{3}\frac{\rho_m}{\rho_w}$

β_m is called the swelling coefficient

In practice, swelling is negligible until a threshold moisture concentration M_0 is exceeded. Therefore, the dilatational strain in the resin is

$$\begin{aligned}\varepsilon_m &= 0 \quad \text{for } M < M_0,\\ &= \beta_m(M - M_0) \quad \text{for } M > M_0\end{aligned} \tag{4.48}$$

The threshold moisture concentration M_0 represents the amount of water absorbed in the free volume as well as microvoids present in the resin. For a variety of cast-epoxy resins, the measured swelling coefficient ranges from 0.26 to 0.33 and the threshold moisture concentration is in the range of 0.3%–0.7% [95].

The dilatational strain in a unidirectional 0° composite laminate due to moisture absorption can be calculated as

$$\text{Longitudinal: } \varepsilon_{mL} = 0, \tag{4.49a}$$

$$\text{Transverse: } \varepsilon_{mT} = \beta_T(M - M_v), \tag{4.49b}$$

where

$\beta_T = (1 + \nu_m)\beta_m(\rho_m/\rho_c)$

ρ_c = composite density

ν_m = matrix Poisson's ratio

$M_v = v_v(\rho_w/\rho_c)$

v_v = void volume fraction

Another physical effect of moisture absorption is the reduction in glass transition temperature of the resin (Figure 4.90). Although the room-temperature performance of a resin may not change with a reduction in T_g, its elevated-temperature properties are severely affected. For example, the modulus of an epoxy resin at 150°C decreases from 2,070 MPa (300,000 psi) to 20.7 MPa (3,000 psi) as its T_g is reduced from 215°C to 127°C. Similar effects may be expected for the matrix-dominated properties of a polymer matrix composite.

Finally, the dilatational expansion of the matrix around the fiber reduces the residual compressive stresses at the fiber–matrix interface caused by curing shrinkage. As a result, the mechanical interlocking between the fiber and the matrix may be relieved.

4.5.2.3 Changes in Performance Due to Moisture and Temperature

From the available data on the effects of temperature and moisture content on the tensile strength and modulus of carbon and boron fiber-reinforced epoxy laminates [96,97], the following conclusions can be made.

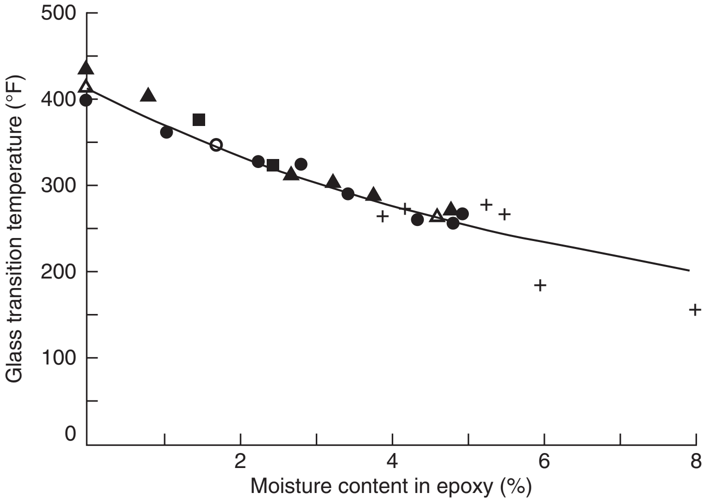

FIGURE 4.90 Variation of glass transition temperature of various epoxy matrices and their composites with moisture content. (After Shirrell, C.D., Halpin, J.C., and Browning, C.E., Moisture—an assessment of its impact on the design of resin based advanced composites, NASA Technical Report, NASA-44-TM-X-3377, April 1976.)

For 0° and $[0/\pm45/90]_S$ quasi-isotropic laminates, changes in temperature up to 107°C (225°F) have negligible effects on tensile strength and modulus values regardless of the moisture concentration in the material. Although the effect on modulus is negligible up to 177°C (350°F), there may be up to a 20% decrease in tensile strength as the temperature increases from 107°C (225°F) to 177°C (350°F).

For 0° and $[0/\pm45/90]_S$ laminates, the tensile strength and modulus are not affected by moisture absorption below 1% moisture concentration. Although the modulus is not affected by even higher moisture concentration, the tensile strength may decrease by as much as 20% for moisture concentrations above 1%.

For 90° laminates, increasing temperature and moisture concentration reduce both the tensile strength and the modulus by significant amounts. Depending on the temperature and moisture concentration, the reduction may range as high as 60%–90% of the room temperature properties under dry conditions.

The ILSS of composite laminates is also reduced by increasing moisture absorption. For example, short-beam shear tests of a unidirectional carbon fiber–epoxy show nearly a 10% reduction in ILSS at a moisture concentration of 1.2 wt% that was attained after 33 days of exposure to humid air of 95% relative humidity at 50°C. Immersion in boiling water reduced the ILSS by 35%

for the same exposure time [98]. Experiments by Gillat and Broutman [91] on cross-ply carbon fiber–epoxy show nearly a 25% reduction in ILSS as the moisture concentration increased by 1.5 wt%.

Jones et al. [99] reported the effect of moisture absorption on the tension–tension fatigue and flexural fatigue properties of $[0/90]_S$ cross-ply epoxy matrix composites reinforced with E-glass, HTS carbon, and Kevlar 49 fibers. Conditioning treatments included exposure to humid air (65% relative humidity) and immersion in boiling water. The fatigue resistance of carbon fiber–epoxy was found to be unaffected by the conditioning treatment. Exposure to humid air also did not affect the fatigue response of E-glass fiber–epoxy composites; however, immersion in boiling water reduced the fatigue strength by significant amounts, principally due to the damage incurred on the glass fibers by boiling water. On the other hand, the fatigue response of Kevlar 49–epoxy composites was improved owing to moisture absorption, although at high cycles there appears to be a rapid deterioration as indicated by the sharp downward curvature of the *S*–*N* curve (Figure 4.91).

Curtis and Moore [100] reported the effect of moisture absorption on the zero tension and zero compression fatigue performance of two matrix-dominated laminates, namely, $[(90/\pm30)_3]_S$ and $[0_2/-45_2/90_2/+45_2]_S$ layups of carbon fibers in an epoxy matrix. Conditioning was performed in humid air of 95% humidity at 70°C. Despite the matrix-dominated behavior of these laminates, moisture absorption had very little effect on their fatigue lives.

Chamis et al. [101] proposed the following empirical equation for estimating the hygrothermal effect on the matrix properties, which can subsequently be used in modifying the matrix-dominated properties of a unidirectional lamina:

$$\frac{P_{\mathrm{wT}}}{P_0} = \left(\frac{T_{\mathrm{gw}} - T}{T_{\mathrm{gd}} - T_0}\right)^{1/2}, \tag{4.50}$$

where

P_{wT} = matrix property at the use temperature T and moisture content M
P_0 = matrix property at a reference temperature T_0
T_{gd} = glass transition temperature in the dry condition
T_{gw} = glass transition temperature in the wet condition with a moisture content M

The glass transition temperature in the wet condition, T_{gw} is calculated using the following equation:

$$T_{\mathrm{gw}} = (0.005M^2 - 0.1M + 1)T_{\mathrm{gd}} \quad \text{for } M \leq 10\%. \tag{4.51}$$

Equations 4.50 and 4.51 have been used to estimate the hygrothermal effect on epoxy matrix composites, but need experimental validation for other polymer matrix systems.

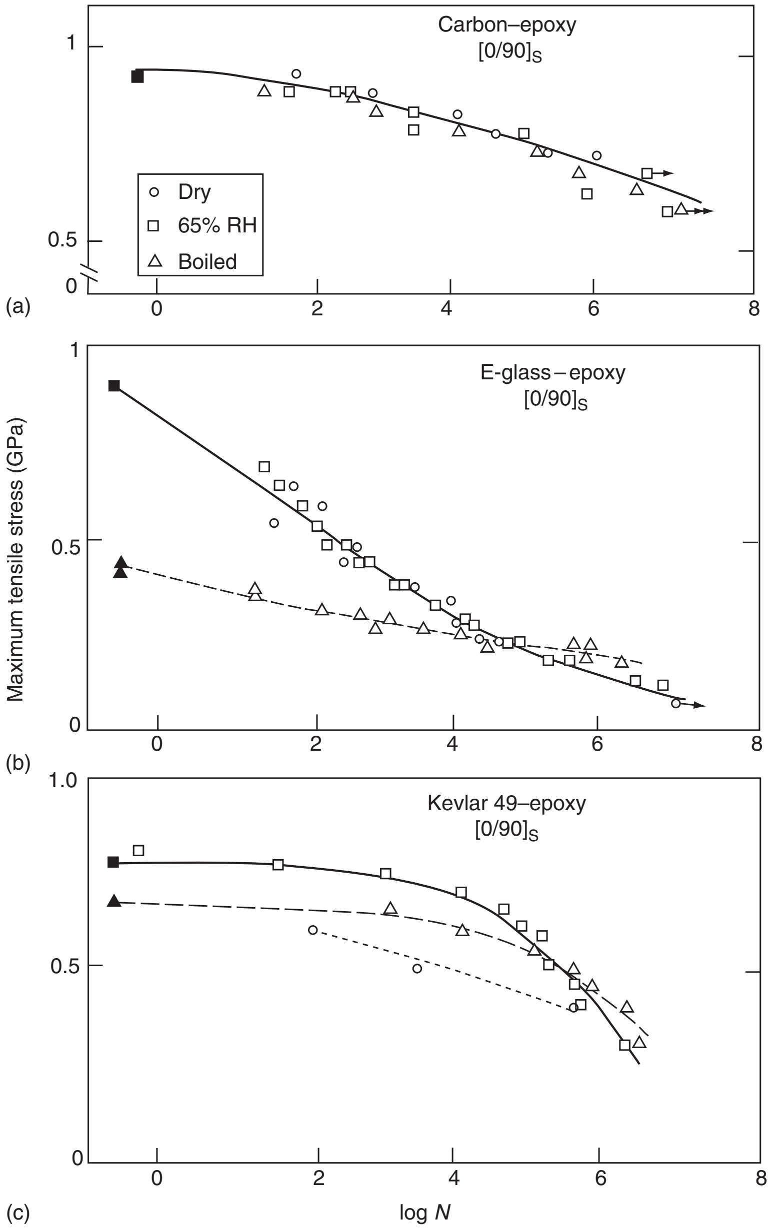

FIGURE 4.91 Effect of moisture absorption on the fatigue behavior of epoxy composites with (a) carbon, (b) E-glass, and (c) Kevlar 49. (After Jones, C.J., Dickson, R.F., Adam, T., Reiter, H., and Harris, B., *Composites*, 14, 288, 1983.)

EXAMPLE 4.3

The tensile strength and modulus of an epoxy matrix at 23°C and dry conditions are 100 MPa and 3.45 GPa, respectively. Estimate its tensile strength and modulus at 100°C and 0.5% moisture content. The glass transition temperature of this epoxy matrix in the dry condition is 215°C.

SOLUTION

Using Equation 4.51, estimate the glass transition temperature at 0.5% moisture content:

$$T_{gw} = [(0.005)(0.5)^2 - (0.1)(0.5) + 1](215)$$
$$= 204.5°C.$$

Now, using Equation 4.50, estimate P_{wT}:

$$P_{wT} = \left(\frac{204.5 - 100}{215 - 23}\right)^{1/2} P_0 = 0.738P_0.$$

Thus, the tensile strength and modulus of the epoxy matrix at 100°C and 0.5% moisture content are estimated as:

$$\sigma_{mu} = (0.738)(100 \text{ MPa}) = 73.8 \text{ MPa},$$
$$E_m = (0.738)(3.45 \text{ GPa}) = 2.546 \text{ GPa}.$$

These values can now be used to estimate the transverse modulus and strength of a unidirectional 0° composite using Equations 3.26 and 3.27, respectively.

4.6 LONG-TERM PROPERTIES

4.6.1 CREEP

Creep is defined as the increase in strain with time at a constant stress level. In polymers, creep occurs because of a combination of elastic deformation and viscous flow, commonly known as viscoelastic deformation. The resulting creep strain increases nonlinearly with increasing time (Figure 4.92). When the stress

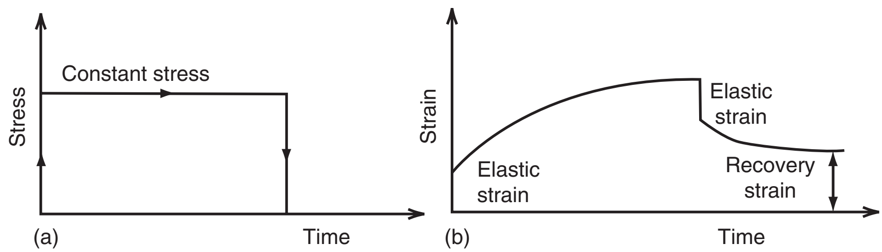

FIGURE 4.92 Schematic representation of creep strain and recovery strain in a polymer.

is released after a period of time, the elastic deformation is immediately recovered. The deformation caused by the viscous flow recovers slowly to an asymptotic value called recovery strain.

Creep strain in polymers and polymer matrix composites depends on the stress level and temperature. Many polymers can exhibit large creep strains at room temperature and at low stress levels. At elevated temperatures or high stress levels, the creep phenomenon becomes even more critical. In general, highly cross-linked thermoset polymers exhibit lower creep strains than thermoplastic polymers. With the exception of Kevlar 49 fibers, commercial reinforcing fibers, such as glass, carbon, and boron, do not creep [102].

4.6.1.1 Creep Data

Under uniaxial stress, the creep behavior of a polymer or a polymer matrix composite is commonly represented by creep compliance, defined as

$$\text{Creep compliance} = D(t) = \frac{\varepsilon(t)}{\sigma}, \tag{4.52}$$

where
σ is the constant stress level in a creep experiment
$\varepsilon(t)$ is the strain measured as a function of time

Figure 4.93 shows typical creep curves for an SMC-R25 laminate at various stress levels. Creep compliances are determined from the slopes of these curves. In general, creep compliance increases with time, stress level, and temperature. For unidirectional fiber-reinforced polymers, it is also a function of fiber orientation angle θ. For $\theta = 0°$ creep compliance is nearly constant, which indicates that creep in the longitudinal direction of a unidirectional 0° laminate is negligible. However, at other fiber orientation angles creep strain can be quite significant.

Fiber orientation angle also influences the temperature dependence of creep compliance. If the fibers are in the loading direction, creep in the composite is governed by the creep in fibers. Thus, with the exception of Kevlar 49 fibers, little temperature dependence is expected in the fiber direction. For other fiber orientations, creep in the matrix becomes the controlling factor. As a result, creep compliance for off-axis laminates increases with increasing temperature (Table 4.21). Creep in SMC-R laminates [103] containing randomly oriented discontinuous fibers is also largely controlled by the matrix creep.

Creep in multidirectional laminates depends on the laminate construction. For example, room temperature creep strains of [±45] and [90/±45] laminates are nearly an order of magnitude different (Figure 4.94), even though the static mechanical properties of these two laminates are similar. The addition of 90° layers to a ±45° construction tends to restrain the rotational tendency of ±45° fibers toward the loading direction and reduces the creep strain significantly.

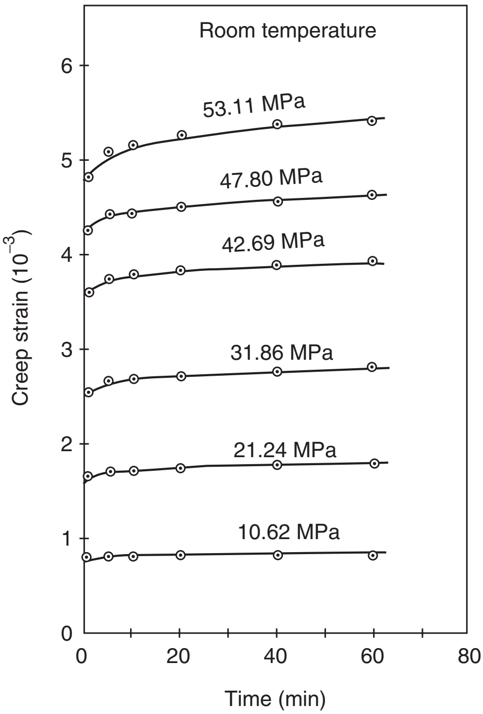

FIGURE 4.93 Tensile creep curves for SMC-R25 polyester laminates. (After Cartner, J.S., Griffith, W.I., and Brinson, H.F., in *Composite Materials in the Automotive Industry*, S.V. Kulkarni, C.H. Zweben, and R.B. Pipes, eds., American Society of Mechanical Engineers, New York, 1978.)

4.6.1.2 Long-Term Creep Behavior

Creep data for a material are generated in the laboratory by conducting either a tensile creep test or a flexural creep test over a period of a few hours to a few hundred hours. Long-term creep behavior of a polymer composite can be predicted from such short-term creep data by the time–temperature superposition method.

The modulus of a polymer at time t and a reference temperature T_0 can be related to its modulus at time t_1 and temperature T_1 by the following equation:

$$E(t,T_0) = \frac{\rho_1 T_1}{\rho_0 T_0}\ E(t_1,T_1), \tag{4.53}$$

where ρ_1 and ρ_0 are the densities of the polymer at absolute temperatures T_1 and T_0, respectively.

$$t = \left(a_T|_{\text{at } T=T_1}\right) t_1 \tag{4.54}$$

TABLE 4.21
Creep Compliance[a] of Unidirectional E-Glass–Epoxy Laminates

		Fiber Orientation Angle			
Temperature	**Property**	**30°**	**45°**	**60°**	**90°**
28°C	Tensile strength (MPa)	278	186.4	88.8	55.2
	1 h compliance (10^{-6} per MPa)	0.0883	0.2065	0.3346	0.5123
	10 h compliance (10^{-6} per MPa)	0.1300	0.3356	0.6295	1.4390
75°C	Tensile strength (MPa)	230	162.8	74.8	43.2
	1 h compliance (10^{-6} per MPa)	0.1217	0.2511	0.4342	0.6689
	10 h compliance (10^{-6} per MPa)	0.1461	0.3841	0.6539	1.5377
100°C	Tensile strength (MPa)	206	134.4	67.7	40.2
	1 h compliance (10^{-6} per MPa)	0.1460	0.3586	0.6931	0.7728
	10 h compliance (10^{-6} per MPa)	0.1751	0.5739	1.2084	1.9031

Source: Sturgeon, J.B., in *Creep of Engineering Materials*, C.D. Pomeroy, ed., Mechanical Engineering Publishing Ltd., London, 1978.

[a] All compliance values are at stress levels equal to 40% of the tensile strength at the corresponding temperature.

where a_T is the *horizontal shift factor*. For most solids, the variation of density with temperature is negligible so that $\rho_1 = \rho_0$. The horizontal shift factor a_T represents the distance along the time scale over which the modulus value at (t_1, T_1) is shifted to create an equivalent response at the reference temperature T_0. Note that a_T is a function of temperature and is determined from short-term creep test data.

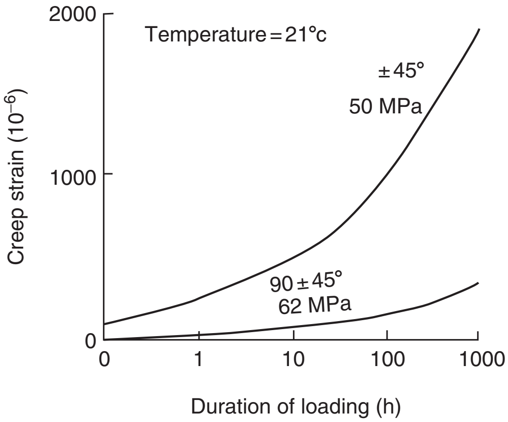

FIGURE 4.94 Comparison of creep curves for $[\pm 45]_S$ and $[90/\pm 45]_S$ laminates. (After Sturgeon, J.B., in *Creep of Engineering Materials*, C.D. Pomeroy, ed., Mechanical Engineering Publishing Ltd., London, 1978.)

The procedure for using the time–temperature superposition method is given as follows.

1. Perform short-term (15 min–1 h) creep tests at various temperatures.
2. Plot creep modulus (or compliance) vs. log (time) for these experiments (Figure 4.95).
3. Select a reference temperature from among the test temperatures used in Step 1.
4. Displace the modulus curves at temperatures other than T_0 horizontally and vertically to match these curves with the modulus curve at T_0.

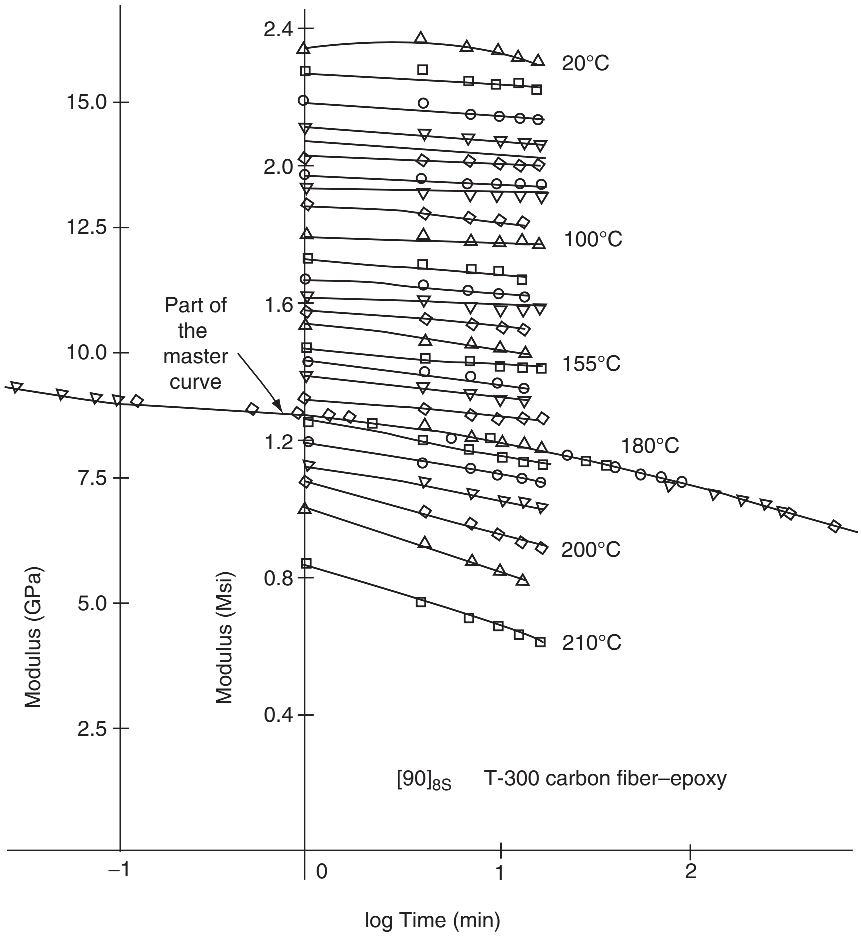

FIGURE 4.95 Creep compliance curves and a portion of the master curve for a T-300 carbon–epoxy laminate. (After Yeow, Y.T., Morris, D.H., and Brinson, H.F., *Composite Materials: Testing and Design* (*Fifth Conference*), *ASTM STP*, 674, 263, 1979.)

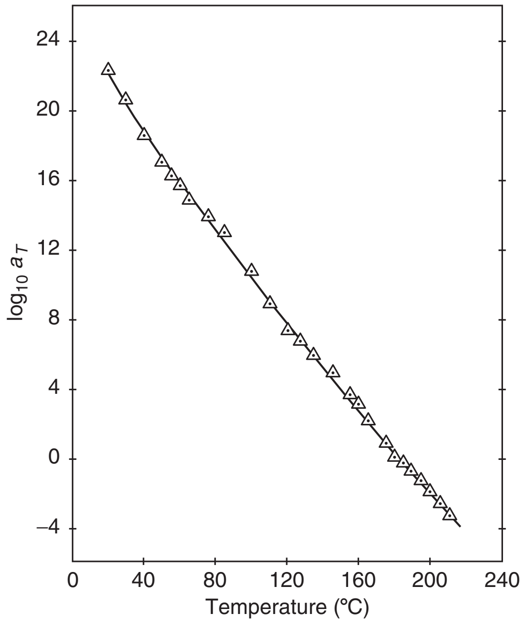

FIGURE 4.96 Shift factor a_T vs. temperature for the time–temperature superposition used in Figure 4.95. (After Yeow, Y.T., Morris, D.H., and Brinson, H.F., *Composite Materials: Testing and Design* (*Fifth Conference*), *ASTM STP*, 674, 263, 1979.)

The modulus curves below the reference temperature are shifted to the left; those above the reference temperatures are shifted to the right. The modulus curve thus obtained is called the *master curve* at the selected reference temperature and may extend over several decades of time (Figure 4.95).

5. Plot the horizontal displacements (which are equal to log a_T) as a function of the corresponding temperature. This shift factor curve (Figure 4.96) can now be used to determine the value of a_T at any other temperature within the range of test temperatures used.
6. The master curve at any temperature within the range of test temperatures used can be determined by multiplying the reference master curve with the appropriate a_T value obtained from the shift factor curve.

The time–temperature superposition method described earlier has been used by Yeow et al. [104] to generate master curves for T-300 carbon fiber–epoxy composites.

4.6.1.3 Schapery Creep and Recovery Equations

For the case of uniaxial loading at a constant temperature, Schapery and his coworker [105] have developed the following constitutive equation relating creep strain to the applied stress σ_0:

$$\varepsilon(t) = \left[g_0 D(0) + C\frac{g_1 g_2 t^n}{a_\sigma^n}\right]\sigma_0, \tag{4.55}$$

where

$D(0)$ = initial compliance
g_0, g_1, g_2, a_σ = stress-dependent constants
C, n = constants (independent of stress level)

During recovery after $t > t_1$, the recovery strain ε_r is

$$\varepsilon_r(t) = \frac{\Delta\varepsilon_1}{g_1}[(1 + a_\sigma\lambda)^n - (a_\sigma\lambda)^n], \tag{4.56}$$

where

$$\Delta\varepsilon_1 = \frac{g_1 g_2 C t_1^n}{a_\sigma^n}\sigma_0$$

$$\lambda = \frac{t - t_1}{t_1}$$

where t_1 is the time at which the stress is released. Detailed derivations of Equations 4.55 and 4.56 as well as the assumptions involved are given in Ref. [105].

At low stress levels, the constants g_0, g_1, g_2, and a_σ are equal to unity. Creep data obtained at low stress levels are used to determine the remaining three constants $D(0)$, C, and n. At high stress levels, the constants $g_0 \neq g_1 \neq g_2 \neq a_\sigma \neq 1$; however, the constants $D(0)$, C, and n do not change.

Determination of g_0, g_1, g_2, and a_σ requires creep and creep recovery tests at high stress levels. Lou and Schapery [105] have presented a graphical technique to reduce the high-stress creep data to determine these constants. Computer-based routines have been developed by Brinson and his coworkers and are described in Ref. [104]. Tuttle and Brinson [106] have also presented a scheme for predicting the long-term creep behavior of a general laminate. In this scheme, the lamination theory (see Chapter 3) and the Schapery theory are combined to predict the long-term creep compliance of the general laminate from the long-term creep compliances of individual laminas.

4.6.2 Stress Rupture

Stress rupture is defined as the failure of a material under sustained constant load. It is usually performed by applying a constant tensile stress to a specimen until it fractures completely. The time at which the fracture occurs is termed the lifetime or stress rupture time. The objective of this test is to determine a range of applied stresses and lifetimes within which the material can be considered "safe" in long-term static load applications.

The data obtained from stress rupture tests are plotted with the applied stress on a linear scale along the ordinate and the lifetime on a logarithmic scale along the abscissa. The functional relationship between the applied stress level and lifetime [107] is often represented as

$$\frac{\sigma}{\sigma_U} = A - B \log t \tag{4.57}$$

where σ_U is the static tensile strength, and A and B are constants. Since the stress-rupture data show a wide range of scatter, the constants are determined by the linear regression method.

Glass, Kevlar 49, and boron fibers and their composites exhibit failure by stress rupture. Carbon fibers, on the other hand, are relatively less prone to stress rupture failure. Chiao and his coworkers [108,109] have gathered the most extensive stress rupture data on epoxy-impregnated S-glass and Kevlar 49 fiber strands. For both materials, the lifetime at a stress level varied over a wide range. However, the rate of degradation under sustained tensile load was lower in Kevlar 49 strands than in S-glass strands. The data were analyzed using a two-parameter Weibull distribution in which the Weibull parameters α and σ_0 were the functions of both stress level σ and test temperature T. An example of the maximum likelihood estimates of lifetimes for Kevlar 49 strands is shown in Figure 4.97. To illustrate the use of this figure, consider the first percentile

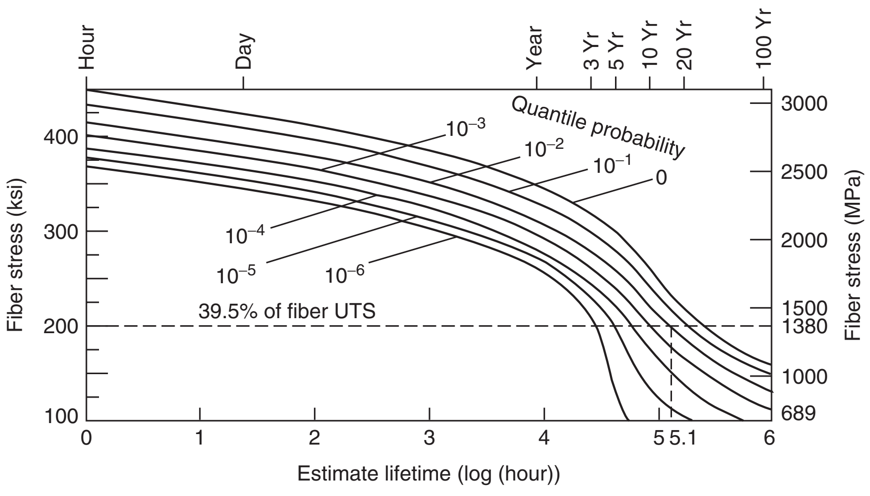

FIGURE 4.97 Maximum likelihood estimates of lifetimes for Kevlar 49–epoxy strands (under ambient conditions with ultraviolet light) for quantile probabilities. (After Glaser, R.E., Moore, R.L., and Chiao, T.T., *Compos. Technol. Rev.*, 6, 26, 1984.)

lifetime estimate of Kevlar 49 strands at 1380 MPa (200 ksi). Corresponding to the first percentile (10^{-2}) curve, $\log t \cong 5.1$, which gives a maximum likelihood estimate for the lifetime as $10^{5.1} = 126{,}000$ h = 14.4 years.

4.7 FRACTURE BEHAVIOR AND DAMAGE TOLERANCE

The fracture behavior of materials is concerned with the initiation and growth of critical cracks that may cause premature failure in a structure. In fiber-reinforced composite materials, such cracks may originate at manufacturing defects, such as microvoids, matrix microcracks, and ply overlaps, or at localized damages caused by in-service loadings, such as subsurface delaminations due to low-energy impacts and hole-edge delaminations due to static or fatigue loads. The resistance to the growth of cracks that originate at the localized damage sites is frequently referred to as the damage tolerance of the material.

4.7.1 Crack Growth Resistance

Many investigators [110–112] have used the linear elastic fracture mechanics (LEFM) approach for studying the crack growth resistance of fiber-reinforced composite materials. The LEFM approach, originally developed for metallic materials, is valid for crack growth with little or no plastic deformation at the crack tip. It uses the concept of stress intensity factor K_I, which is defined as

$$K_I = \sigma_o \sqrt{\pi a}\, Y, \tag{4.58}$$

where

K_I = Mode I stress intensity factor (Mode I refers to the opening mode of crack propagation due to an applied tensile stress normal to the crack plane)
σ_o = applied stress
a = crack length
Y = geometric function that depends on the crack length, crack location, and mode of loading

Equation 4.58 shows that the stress intensity factor increases with both applied stress and crack length. An existing crack in a material may propagate rapidly in an unstable manner (i.e., with little or no plastic deformation), when the K_I value reaches a critical level. The critical stress intensity factor, K_{Ic}, also called the fracture toughness, indicates the resistance of the material to unstable crack growth.

The critical stress intensity factor of metals is determined by standard test methods, such as ASTM E399. No such standard test method is currently available for fiber-reinforced composite materials. Most investigators have

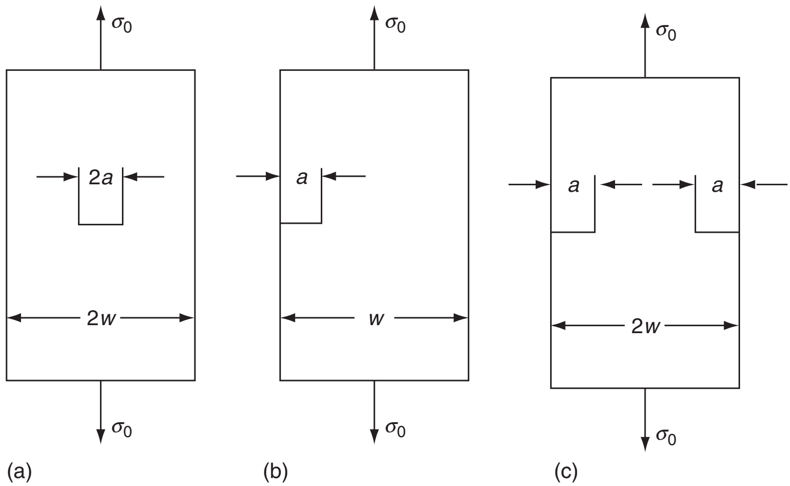

FIGURE 4.98 Notched specimens for determining the fracture toughness of a material: (a) center notched, (b) single-edge notched, and (c) double-edge notched.

used static tensile testing of prenotched straight-sided specimens to experimentally determine the stress intensity factor of fiber-reinforced composite laminates. Three types of specimens, namely, center-notched (CN), single-edge notched (SEN), and double-edge notched (DEN) specimens, are commonly used (Figure 4.98). Load vs. crack opening displacement records (Figure 4.99) obtained in these tests are initially linear. However, they become increasingly nonlinear or even discontinuous as irreversible subcritical damages appear in

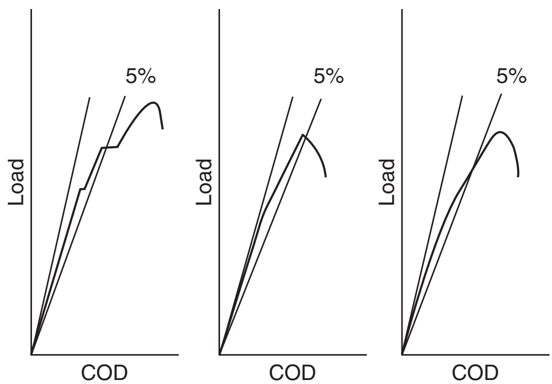

FIGURE 4.99 Typical load vs. crack opening displacement (COD) records obtained in tension testing of center-notched specimens. (After Harris, C.E. and Morris, D.H., *J. Compos. Technol. Res*., 7, 77, 1985.)

the vicinity of the notch tip. Since the load–displacement curve deviates from linearity, it becomes difficult to determine the load at which crack growth begins in an unstable manner. The critical stress intensity factor calculated on the basis of the maximum load tends to depend on the notch size, laminate thickness, and laminate stacking sequence. Instead of using the maximum load, Harris and Morris [110] calculated the stress intensity factor on the basis of the load where a line drawn through the origin with 95% of the initial slope (i.e., 5% offset from the initial slope) intercepts the load–displacement curve. Physically, this stress intensity factor, denoted as K_5, has been associated with the onset of significant notch tip damage. Harris and Morris found the K_5 value to be relatively insensitive to the geometric variables, such as notch length, laminate thickness, and laminate stacking sequence (Table 4.22), and called it the fracture toughness of the composite material.

TABLE 4.22
Fracture Toughness of T-300 Carbon Fiber–Epoxy Laminates

	Fracture Toughness, K_5 Values	
Laminate Type	**(MPa m$^{1/2}$)**	**(ksi in.$^{1/2}$)**
$[0/90/\pm45]_S$	37.0	33.7
$[0/\pm45/90]_S$	33.5	30.5
$[\pm45/0/90]_S$	31.4	28.6
$[0/\pm45/90]_{8S}$	29.8	27.1
$[0/\pm45/90]_{15S}$	29.9	27.2
$[\pm45/0]_S$	32.3	29.4
$[0/\pm45]_S$	32.0	29.1
$[0/\pm45]_{10S}$	32.2	29.3
$[0/\pm45]_{20S}$	31.6	28.8
$[45/0/-45]_S$	27.5	25.0
$[0/90]_S$	27.8	25.3
$[0/90]_{16S}$	28.7	26.1
$[0/90]_{30S}$	26.6	24.2
$[\pm30/90]_S$	35.7	32.5
$[90/\pm30]_S$	36.4	33.1
$[30/90/-30]_S$	37.6	34.2
$[90/\pm30]_{16S}$	28.2	25.7
$[60/0/-60]_S$	26.4	24.0
$[0/\pm60]_S$	33.8	30.8
$[\pm60/0]_S$	35.9	32.7
$[0/\pm60]_S$	27.4	24.9

Source: Adapted from Harris, C.E. and Morris, D.H., *J. Compos. Technol. Res.*, 7, 77, 1985.

Harris and Morris [110,113] have also observed that the fracture process in continuous fiber laminates depends on the laminate type and laminate thickness. For example, in thin $[0/\pm45]_{nS}$ laminates, massive delaminations at the crack tip create uncoupling between the $+45°$ and $-45°$ plies, which is followed by an immediate failure of the laminate. The nonlinearity in the load–displacement diagram of this laminate ensues at or near the maximum load. As the laminate thickness increases, the thickness constraint provided by the outer layers prevents ply delaminations at the interior layers and the notched laminate strength is increased. In contrast, thin $[0/\pm45/90]_{nS}$ laminates develop minor delaminations as well as matrix microcracks at the crack tip at lower than the maximum load; however, the damage developed at the crack tip tends to relieve the stress concentration in its vicinity. As a result, the load–displacement diagram for $[0/\pm45/90]_{nS}$ laminates is more nonlinear and their notched laminate strength is also higher than that of $[0/\pm45]_{nS}$ laminates. With increasing thickness, the size of the crack tip damage in $[0/\pm45/90]_{nS}$ decreases and there is less stress relief in the crack tip region, which in turn lowers the value of their notched tensile strength.

In laminates containing randomly oriented fibers, crack tip damage contains matrix microcracks, fiber–matrix interfacial debonding, fiber breakage, and so on. This damage may start accumulating at load levels as low as 50%–60% of the maximum load observed in a fracture toughness test. Thus the load–displacement diagrams are also nonlinear for these laminates. From the load–displacement records for various initial crack lengths, Gaggar and Broutman [112] developed a crack growth resistance curve similar to that given in Figure 4.100. This curve can be used to predict the stress intensity factor at the point of unstable crack growth.

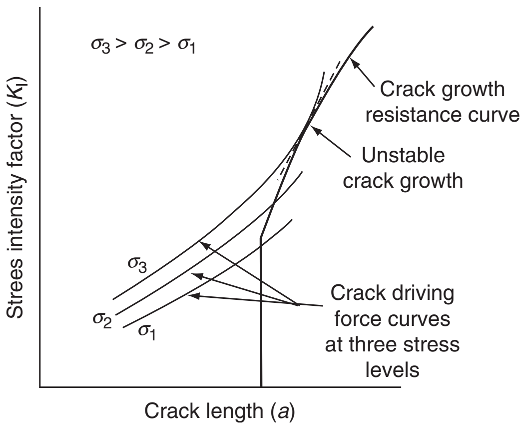

FIGURE 4.100 Crack growth resistance curve of a random fiber laminate. (After Gaggar, S.K. and Broutman, L.J., *J. Compos. Mater*., 9, 216, 1975.)

4.7.2 Delamination Growth Resistance

Interply delamination is considered the most critical failure mode limiting the long-term fatigue life of certain composite laminates [114]. In general, delamination develops at the free edges of a laminate where adverse interlaminar stresses may exist owing to its particular stacking sequence. Once developed, the delaminated areas may grow steadily with increasing number of cycles, which in turn reduces the effective modulus of the laminate. The presence of delamination also causes a redistribution of stresses within the laminate, which may influence the initiation of fiber breakage in the primary load-bearing plies and reduce the fatigue life of the laminate. In recognition of this problem, a number of test methods [115] have been developed to measure the interlaminar fracture toughness of composite laminates.

The interlaminar fracture toughness, measured in terms of the critical strain energy release rate, is defined as the amount of strain energy released in propagating delamination by a unit length. This LEFM parameter is frequently used for comparing the resistance of various resin systems against the growth of delamination failure.

Delamination may occur in Mode I (opening mode or tensile mode of crack propagation), Mode II (sliding mode or in-plane shear mode of crack propagation), Mode III (tearing mode or antiplane shear mode of crack propagation), or a combination of these modes. The test methods used for determining the critical strain energy release rate in Mode I and Mode II delaminations are briefly described here. In Mode I, crack propagation occurs as the crack surfaces pull apart due to a normal stress perpendicular to the crack plane. In Mode II, crack propagation occurs as the crack surfaces slide over each other due to a shear stress parallel to the crack plane. The compliance method is used in the calculation of the strain energy release rate for each mode, which is related to the specimen compliance by the following equation:

$$G_{\mathrm{I}} \text{ or } G_{\mathrm{II}} = \frac{P^2}{2w}\frac{\mathrm{d}C}{\mathrm{d}a}, \tag{4.59}$$

where

P = applied load
w = specimen width
a = crack length (measured by a traveling microscope during the test)
C = specimen compliance (slope of the load–displacement curve for each crack length) (see Figure 4.102)
$\frac{\mathrm{d}C}{\mathrm{d}a}$ = slope of the compliance vs. crack length curve

The interlaminar fracture toughness, G_{Ic} in Mode I and G_{IIc} in Mode II, are calculated using the critical load P_{c} and $\frac{\mathrm{d}C}{\mathrm{d}a}$ corresponding to the crack length at the onset of delamination propagation.

4.7.2.1 Mode I Delamination

Two commonly used Mode I interlaminar fracture energy tests are the double-cantilever beam (DCB) test and the edge delamination tension (EDT) test.

DCB test: The DCB test is used for determining the strain energy release rate G_I for delamination growth under Mode I loading. It commonly uses a straight-sided 0° unidirectional specimen (Figure 4.101) in which an initial crack (delamination) is created by inserting a thin Teflon film (typically 0.013 mm thick) at the midplane before molding the laminate. Hinged metal tabs are bonded at the delaminated end of the specimen. Load is applied through the metal tabs until the initial crack grows slowly by a predetermined length. The specimen is unloaded and then reloaded until the new crack in the specimen grows slowly by another predetermined length. This process is repeated several times with the same specimen to obtain a series of load–displacement records, as shown in Figure 4.102. For each crack length, a specimen compliance value is calculated using the slope of the loading portion of the corresponding load–displacement record. A typical compliance vs. crack length curve is shown in Figure 4.103.

EDT test: The EDT test uses a straight-sided 11-ply $[(\pm 30)_2/90/\overline{90}]_S$ laminate that exhibits free-edge delaminations at both $-30°/90°$ interfaces under a tensile load. It involves determining the laminate stiffness E_{LAM} and

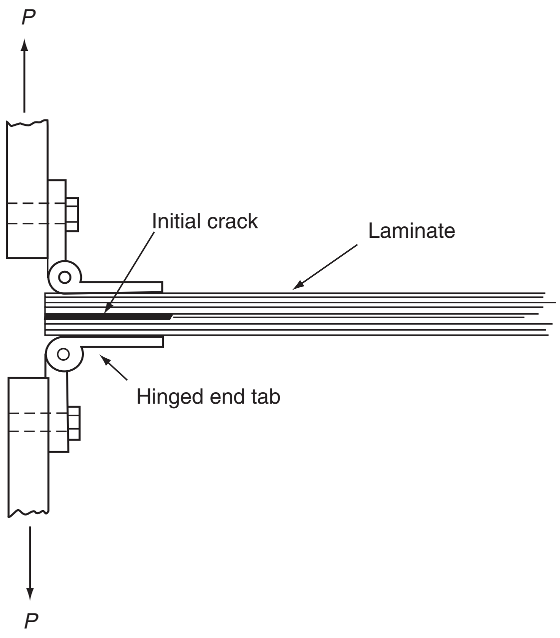

FIGURE 4.101 A double-cantilever beam (DCB) specimen.

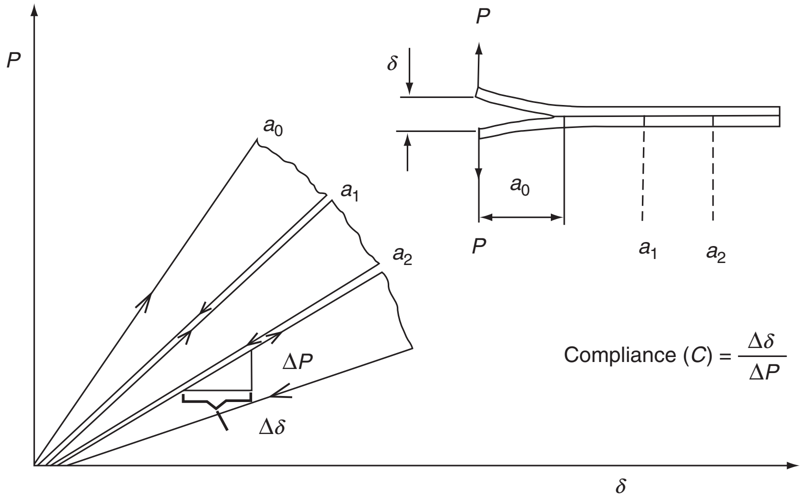

FIGURE 4.102 Typical load–displacement records obtained in a DCB test.

the normal strain ε_c at the onset of delamination from the stress–strain diagram (Figure 4.104) obtained in a static tension test of the $[(\pm 30)_2/90/\overline{90}]_S$ laminate. The critical strain energy release rate at the onset of delamination is then calculated using the following equation [116]:

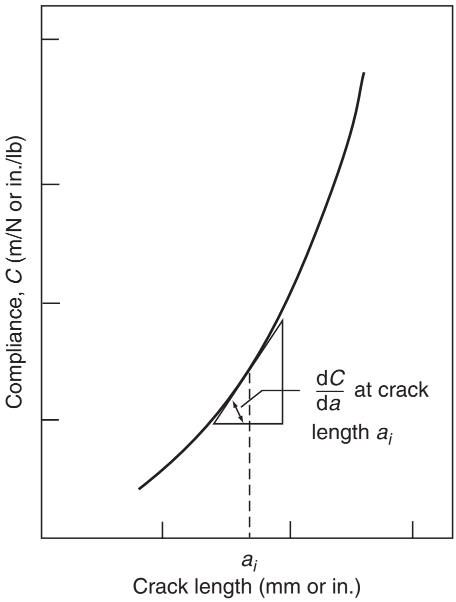

FIGURE 4.103 Schematic representation of compliance vs. crack length in a DCB test.

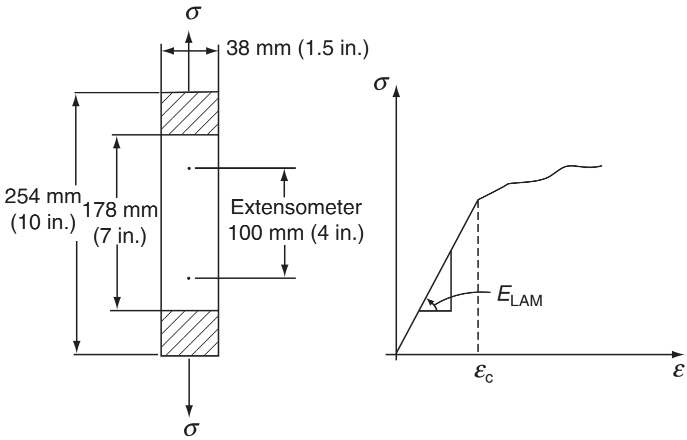

FIGURE 4.104 An edge delamination tension (EDT) test.

$$G_{\mathrm{Ic}} = \frac{\varepsilon_{\mathrm{c}}^2 t}{2}(E_{\mathrm{LAM}} - E^*), \tag{4.60}$$

where

h = specimen thickness
ε_{c} = strain at the onset of delamination
E_{LAM} = initial laminate stiffness
E^* = $[8E_{(30)} + \, + \, 3E_{(90)}]/11$

The E^* term in Equation 4.60 represents a simple rule of mixture calculation for the laminate stiffness after complete delamination has taken place at both $-30°/90°$ interfaces.

Both DCB and EDT tests are useful in qualitatively ranking various matrix materials for their role in delamination growth resistance of a laminate. Both tests produce comparable results (Figure 4.105). In general, the delamination growth resistance increases with increasing fracture toughness of the matrix; however, improving the fracture toughness of a matrix may not translate into an equivalent increase in the delamination growth of a laminate.

4.7.2.2 Mode II Delamination

End notched flexure tests are used to determine the interlaminar fracture toughness in Mode II delamination of [0] unidirectional laminates. There are two types of end notched flexure tests: (a) 3-point or 3-ENF test and (b) 4-point or 4-ENF test. The specimen and loading configurations for these two tests are shown in Figure 4.106. In both specimens, a starter crack is created at one end of the specimen by placing a thin Teflon film (typically 0.013 mm thick) at the

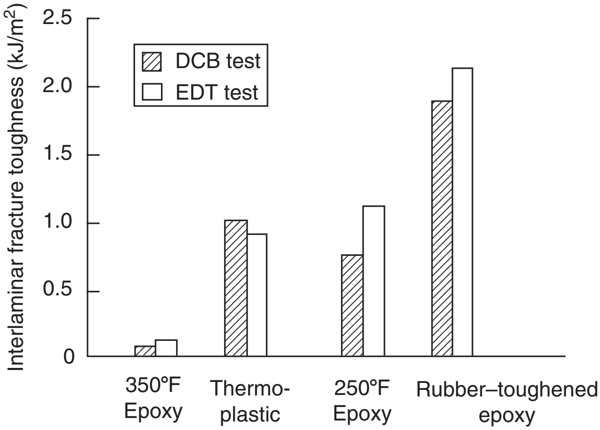

FIGURE 4.105 Comparison of the interlaminar fracture toughness of various resin systems. (After O'Brien, T.K., *Tough Composite Materials: Recent Developments*, Noyes Publications, Park Ridge, NJ, 1985.)

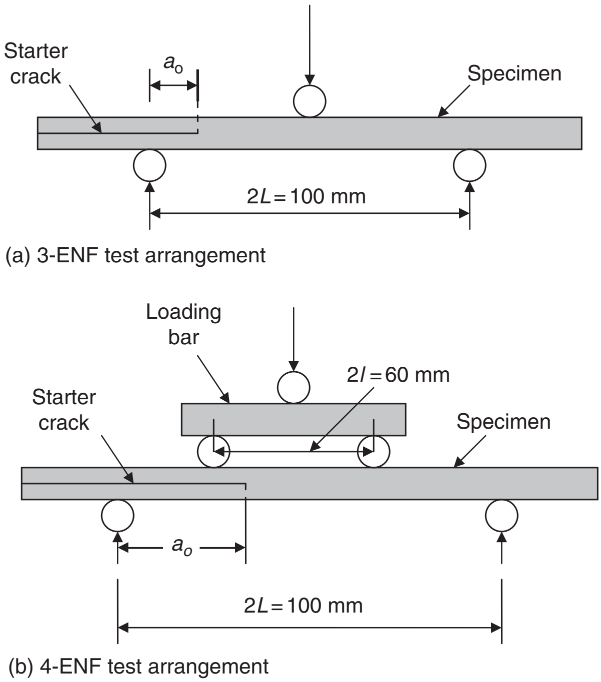

FIGURE 4.106 Schematic of the (a) 3-ENF and (b) 4-ENF specimens and tests.

midplane of the laminate before molding the laminate. The test is conducted at a constant displacement rate of the loading point and the crack growth is monitored. The load–displacement diagram is also recorded during the test.

In the 3-ENF test, it is difficult to obtain stable crack growth, and therefore, multiple specimens with different initial crack lengths are required to plot the compliance vs. crack length curve. On the other hand, the 4-ENF test produces a stable crack growth, and therefore, one specimen is sufficient to determine the Mode II strain energy release rate. In the 4-ENF test, the specimen is unloaded after every 2–3 mm stable crack growth and then reloaded until the new crack grows slowly by another 2–3 mm. As with the DCB specimen, the specimen compliance, C, is determined from the slope of the load–displacement curve corresponding to each new crack length. From the compliance vs. crack length curve $\mathrm{d}c/\mathrm{d}a$ is calculated, which is then used in Equation 4.59 for calculating G_{IIc}. Schuecker and Davidson [117] have shown that if crack length and compliance are measured accurately, the 3-ENF and 4-ENF tests yield similar G_{IIc}.

4.7.3 Methods of Improving Damage Tolerance

Damage tolerance of laminated composites is improved if the initiation and growth of delamination can be either prevented or delayed. Efforts to control delamination have focused on both improving the interlaminar fracture toughness and reducing the interlaminar stresses by means of laminate tailoring. Material and structural parameters that influence the damage tolerance are matrix toughness, fiber–matrix interfacial strength, fiber orientation, stacking sequence, laminate thickness, and support conditions. Some of these parameters have been studied by many investigators and are discussed in the following section.

4.7.3.1 Matrix Toughness

The fracture toughness of epoxy resins commonly used in the aerospace industry is 100 $\mathrm{J/m^2}$ or less. Laminates using these resins have an interlaminar (Mode I delamination) fracture toughness in the range of 100–200 $\mathrm{J/m^2}$. Increasing the fracture toughness of epoxy resins has been shown to increase the interlaminar fracture toughness of the composite. However, the relative increase in the interlaminar fracture toughness of the laminate is not as high as that of the resin itself.

The fracture toughness of an epoxy resin can be increased by adding elastomers (e.g., CTBN), reducing cross-link density, increasing the resin chain flexibility between cross-links, or a combination of all three (Table 4.23). Addition of rigid thermoplastic resins also improves its fracture toughness. Another alternative is to use a thermoplastic matrix, such as PEEK, PPS, PAI, and so on, which has a fracture toughness value in the range of 1000 $\mathrm{J/m^2}$, 10-fold higher than that of conventional epoxy resins.

TABLE 4.23
Mode I Interlaminar Fracture Toughness as Influenced by the Matrix Composition

General Feature of the Base Resin	Matrix Properties: Tensile Strain-to-Failure (%)	Matrix Properties: G_{Ic} (J/m^2)	Composite Properties[a]: v_f (%)	Composite Properties[a]: Transverse Tensile Strain-to-Failure (%)	Composite Properties[a]: G_{Ic} (J/m^2)
Rigid TGMDA/DDS epoxy	1.34	70	76	0.632	190
Moderately cross-linked with rigid backbone between cross-links	1.96	167	54	0.699	335
Same as above plus CTBN rubber particles	3.10	730	60	0.580	1015
			69		520
			71		615
Epoxy with low cross-link density and soft backbone between cross-links	3.24	460	58	0.538	455
Same as above plus CTBN rubber particles	18.00	5000	57	0.538	1730

Source: Adapted from Jordan, W.M., Bradley, W.L., and Moulton, R.J., *J. Compos. Mater.*, 23, 923, 1989.

[a] 0° Unidirectional carbon fiber-reinforced epoxy composites.

4.7.3.2 Interleaving

A second approach of enhancing the interlaminar fracture toughness is to add a thin layer of tough, ductile polymer or adhesive between each consecutive plies in the laminate [118] (Figure 4.107). Although the resin-rich interleaves increase the interlaminar fracture toughness, fiber-dominated properties, such as tensile

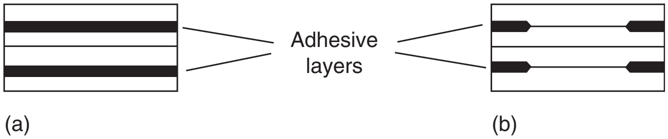

FIGURE 4.107 Interleaving with adhesive layers (a) along the whole laminate width and (b) along the free edges only.

strength and modulus, may decrease due to a reduction in overall fiber volume fraction.

4.7.3.3 Stacking Sequence

High interlaminar normal and shear stresses at the free edges of a laminate are created due to mismatch of Poisson's ratios and coefficients of mutual influence between adjacent layers. Changing the ply stacking sequence may change the interlaminar normal stress from tensile to compressive so that opening mode delamination can be suppressed. However, the growth of delamination may require the presence of an interrupted load path. For example, Lee and Chan [119] used discrete 90° plies at the midplanes of $[30/-30_2/30]_S$ and $[\pm 35/0]_S$ laminates to reduce delamination in these laminates. Delamination was arrested at the boundaries of these discrete plies.

4.7.3.4 Interply Hybridization

This can also be used to reduce the mismatch of Poisson's ratios and coefficients of mutual influence between consecutive layers, and thus reduce the possibility of interply edge delamination. For example, replacing the 90° carbon fiber–epoxy plies in $[\pm 45/0_2/90_2]_S$ AS-4 carbon fiber–epoxy laminates with 90° E-glass fiber–epoxy plies increases the stress level for the onset of edge delamination (due to interlaminar normal stress, σ_{zz}) from 324 to 655 MPa. The ultimate tensile strength is not affected, since it is controlled mainly by the 0° plies, which are carbon fiber–epoxy for both laminates [120].

4.7.3.5 Through-the-Thickness Reinforcement

Resistance to interlaminar delamination can be improved by means of through-the-thickness reinforcement that can be in the form of stitches, metallic wires and pins, or three-dimensional fabric structures.

Mignery et al. [121] used fine Kevlar thread to stitch the layers in $[\pm 30/0]_S$, $[\pm 30/90]_S$, and $[\pm 45/0_2/90]_S$ AS-4 carbon fiber–epoxy laminates. Stitches parallel to the 0° direction were added after layup with an industrial sewing machine at a distance of 1.3–2.5 mm from the free edges in 32 mm wide test specimens. Although stitching did not prevent the occurrence of free-edge delamination in uniaxial tensile tests, it substantially reduced the rate of delamination growth into the interior of the latter two laminates. No visible edge delamination occurred in either unstitched or stitched $[\pm 30/0]_S$ laminates before complete fracture.

Figure 4.108 shows the construction of a three-dimensional composite containing alternate 0/90 layers in the laminate plane (xy plane) and vertical through-the-thickness fibers interlocked with the in-plane layers. Gillespie and his coworkers [122] reported a 10-fold increase in the Mode I interlaminar

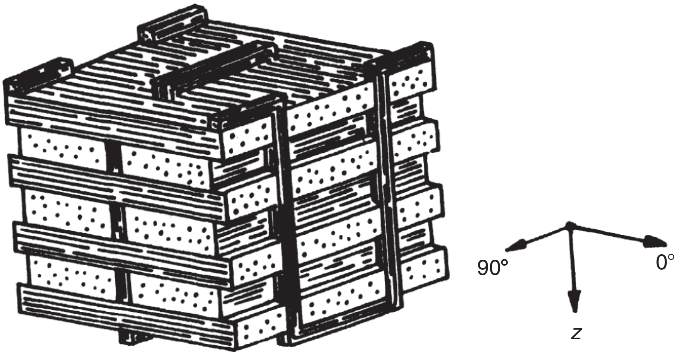

FIGURE 4.108 Construction of a three-dimensional laminate.

fracture toughness of such three-dimensional composites over the two-dimensional 0/90 laminates; however, the in-plane stiffness properties are decreased.

4.7.3.6 Ply Termination

High interlaminar stresses created by mismatching plies in a narrow region near the free edge are reduced if they are terminated away from the free edge. Chan and Ochoa [123] tension tested $[\pm 35/0/09]_S$ laminates in which the 90° layers were terminated at ~3.2 mm away from the free edges of the tension specimen and found no edge delamination up to the point of laminate failure. The ultimate tensile strength of the laminate with 90° ply terminations was 36% higher than the baseline laminate without ply termination. In the baseline laminate, free-edge delamination between the central 90° layers was observed at 49% of the ultimate load.

4.7.3.7 Edge Modification

Sun and Chu [124] introduced a series of narrow and shallow (1.6–3.2 mm deep) notches (Figure 4.109) along the laminate edges and observed a significant

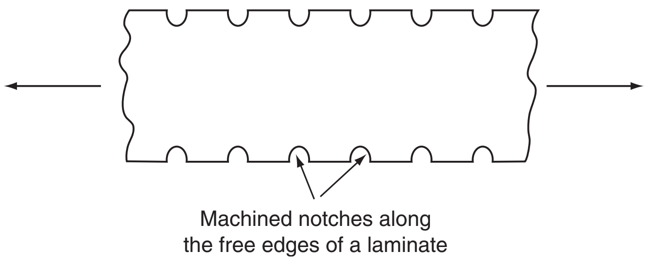

FIGURE 4.109 Edge notched laminate.

increase (25% or higher) in tensile failure load for laminates that are prone to interlaminar shear failure. Delamination was either eliminated or delayed in laminates that are prone to opening mode delamination, but there was no improvement in tensile failure load. The presence of notches disrupts the load path near the free edges and reduces the interlaminar stresses. However, they also introduce high in-plane stress concentration. Thus, suppression of delamination by edge notching may require proper selection of notch size and spacing.

REFERENCES

1. N.J. Pagano and J.C. Halpin, Influence of end constraint in the testing of anisotropic bodies, *J. Compos. Mater., 2*:18 (1968).
2. R.R. Rizzo, More on the influence of end constraints on off-axis tensile tests, *J. Compos. Mater., 3*:202 (1969).
3. B.E. Kaminski, Effects of specimen geometry on the strength of composite materials, *Analysis of the Test Methods for High Modulus Fibers and Composites, ASTM STP, 521*:181 (1973).
4. M.R. Piggott and B. Harris, Compression strength of carbon, glass and Kevlar 49 fibre reinforced polyester resins, *J. Mater. Sci., 15*:2523 (1980).
5. C.D. Shirrell, Variability in static strengths of sheet molding compounds (SMC), *Polym. Compos., 4*:172 (1983).
6. H.T. Hahn and S.W. Tsai, On the behavior of composite laminates after initial failure, *J. Compos. Mater., 8*:288 (1974).
7. P.A. Lagace, Nonlinear stress–strain behavior of graphite/epoxy laminates, *AIAA J., 23*:1583 (1985).
8. J.E. Masters and K.L. Reifsnider, An investigation of cumulative damage development in quasi-isotropic graphite/epoxy laminates, *Damage in Composite Materials, ASTM STP, 775*:40 (1982).
9. T. Watanabe and M. Yasuda, Fracture behavior of sheet molding compounds. Part 1: Under tensile load, *Composites, 13*:54 (1982).
10. J. Aveston and A. Kelly, Tensile first cracking strain and strength of hybrid composites and laminates, *Phil. Trans. R. Soc. Lond., A, 294*:519 (1980).
11. P.W. Manders and M.G. Bader, The strength of hybrid glass/carbon fiber composites. Part 1: Failure strain enhancement and failure mode, *J. Mater. Sci., 16*:2233 (1981).
12. J.M. Whitney, I.M. Daniel, and R.B. Pipes, *Experimental Mechanics of Fiber Reinforced Composite Materials*, Society for Experimental Mechanics, Brookfield Center, CT (1984).
13. C. Zweben, W.S. smith, and M.M. Wardle, Test methods for fiber tensile strength, composite flexural modulus, and properties of fabric-reinforced laminates, *Composite Materials: Testing and Design* (*Fifth Conference*), *ASTM STP, 674*:228 (1979).
14. R.E. Bullock, Strength ratios of composite materials in flexure and in tension, *J. Compos. Mater., 8*:200 (1974).
15. J.M. Whitney and M. Knight, The relationship between tensile strength and flexure strength in fiber-reinforced composites, *Exp. Mech., 20*:211 (1980).

16. Y.T. Yeow and H.F. Brinson, A comparison of simple shear characterization methods for composite laminates, *Composites, 9*:49 (1978).
17. C.C. Chiao, R.L. Moore, and T.T. Chiao, Measurement of shear properties of fibre composites. Part 1: Evaluation of test methods, *Composites, 8*:161 (1977).
18. C.C. Chamis and J.J. Sinclair, Ten-deg off-axis test for shear properties in fiber composites, *Exp. Mech., 17*:339 (1977).
19. D.E. Walrath and D.F. Adams, The Iosipescu shear test as applied to composite materials, *Exp. Mech., 23*:105 (1983).
20. D.W. Wilson, Evaluation of V-notched beam shear test through an interlaboratory study, *J. Compos. Technol. Res., 12*:131 (1990).
21. J.M. Whitney, D.L. Stansberger, and H.B. Howell, Analysis of the rail shear test—applications and limitations, *J. Compos. Mater., 5*:24 (1971).
22. R. Garcia, T.A. Weisshaar, and R.R. McWithey, An experimental and analytical investigation of the rail shear-test method as applied to composite materials, *Exp. Mech., 20*:273 (1980).
23. B.K. Daniels, N.K. Harakas, and R.C. Jackson, Short beam shear tests of graphite fiber composites, *Fibre Sci. Technol., 3*:187 (1971).
24. W.W. Stinchcomb, E.G. Henneke, and H.L. Price, Use of the short-beam shear test for quality control of graphite-polyimide laminates, *Reproducibility and Accuracy of Mechanical Tests, ASTM STP, 626*:96 (1977).
25. C.A. Berg, T. Tirosh, and M. Israeli, Analysis of the short beam bending of fiber reinforced composites, *Composite Materials: Testing and Design* (*Second Conference*), *ASTM STP, 497*:206 (1972).
26. L.L. Lorenzo and H.T. Hahn, Fatigue failure mechanisms in unidirectional composites, *Composite Materials—Fatigue and Fracture, ASTM STP, 907*: 210 (1986).
27. H.T. Hahn and R.Y. Kim, Fatigue behavior of composite laminates, *J. Compos. Mater., 10*:156 (1976).
28. B.D. Agarwal and J.W. Dally, Prediction of low-cycle fatigue behavior of GFRP: an experimental approach, *J. Mater. Sci., 10*:193 (1975).
29. H.T. Hahn and R.Y. Kim, Proof testing of composite materials, *J. Compos. Mater., 9*:297 (1975).
30. D.A. Riegner and B.A. Sanders, A characterization study of automotive continuous and random glass fiber composites, *Proceedings National Technical Conference*, Society of Plastics Engineers, November (1979).
31. R.A. Heimbuch and B.A. Sanders, Mechanical properties of automotive chopped fiber reinforced plastics, *Composite Materials in the Automobile Industry*, ASME, New York (1978).
32. P.K. Mallick, Fatigue characteristics of high glass content sheet molding compound (SMC) materials, *Polym. Compos., 2*:18 (1981).
33. R.B. Pipes, Interlaminar shear fatigue characteristics of fiber reinforced composite materials, *Composite Materials: Testing and Design* (*Third Conference*), *ASTM STP, 546*:419 (1974).
34. C.K.H. Dharan, Interlaminar shear fatigue of pultruded graphite fibre–polyester composites, *J. Mater. Sci., 13*:1243 (1978).
35. M.J. Owen and S. Morris, Some interlaminar-shear fatigue properties of carbon-fibre-reinforced plastics, *Plast. Polym., 4*:209 (1972).

36. D.W. Wilson, Characterization of the interlaminar shear fatigue properties of SMC-R50, Technical Report No. 80–05, Center for Composite Materials, University of Delaware, Newark, DE (1980).
37. D.C. Phillips and J.M. Scott, The shear fatigue of unidirectional fibre composites, *Composites, 8*:233 (1977).
38. J.D. Conners, J.F. Mandell, and F.J. McGarry, Compressive fatigue in glass and graphite reinforced composites, *Proceedings 34th Annual Technical Conference*, Society of the Plastics Industry (1979).
39. Z. Hashin and A. Rotem, A fatigue failure criterion for fiber reinforced materials, *J. Compos. Mater., 7*:448 (1973).
40. K.H. Boller, Fatigue characteristics of RP laminates subjected to axial loading, *Mod. Plast., 41*:145 (1964).
41. J.W. Davis, J.A. McCarthy, and J.N. Schrub, The fatigue resistance of reinforced plastics, *Materials in Design Engineering*, p. 87 (1964).
42. M.J. Owen and R.G. Rose, Polyester flexibility versus fatigue behavior of RP, *Mod. Plast., 47*:130 (1970).
43. T. Tanimoto and S. Amijima, Progressive nature of fatigue damage of glass fiber reinforced plastics, *J. Compos. Mater., 9* (1975).
44. C.K.H. Dharan, Fatigue failure in graphite fibre and glass fibre-polymer composites, *J. Mater. Sci., 10*:1665 (1975).
45. K.H. Boller, Effect of tensile mean stresses on fatigue properties of plastic laminates reinforced with unwoven glass fibers, U.S. Air Force Materials Laboratory, Report No. ML-TDR-64–86, June (1964).
46. S.V. Ramani and D.P. Williams, Axial fatigue of $[0/\pm 30]_{6S}$ graphite/epoxy, *Failure Mode in Composites III*, AIME, p. 115 (1976).
47. T.R. Smith and M.J. Owen, Fatigue properties of RP, *Mod. Plast., 46*:124 (1969).
48. J.W. Dally and L.J. Broutman, Frequency effects on the fatigue of glass reinforced plastics, *J. Compos. Mater., 1*:424 (1967).
49. J.F. Mandell and U. Meier, Effects of stress ratio, frequency, and loading time on the tensile fatigue of glass-reinforced epoxy, *Long-Term Behavior of Composites, ASTM STP, 813*:55 (1983).
50. C.T. Sun and W.S. Chan, Frequency effect on the fatigue life of a laminated composite, *Composite Materials, Testing and Design* (*Fifth Conference*), *ASTM STP, 674*:418 (1979).
51. C.R. Saff, Effect of load frequency and lay-up on fatigue life of composites, *Long-Term Behavior of Composites, ASTM STP, 813*:78 (1983).
52. K.L. Reifsnider, W.W. Stinchcomb, and T.K. O'Brien, Frequency effects on a stiffness-based fatigue failure criterion in flawed composite specimens, *Fatigue of Filamentary Composite Materials, ASTM STP, 636*: 171 (1977).
53. J.H. Underwood and D.P. Kendall, Fatigue damage in notched glass–epoxy sheet, *Proceedings International Conference on Composite Materials*, Vol. 2, AIME, p. 1122 (1975).
54. C.K.H. Dharan, Fatigue failure mechanisms in a unidirectionally reinforced composite material, *Fatigue of Composite Materials, ASTM STP, 569*:171 (1975).
55. H.C. Kim and L.J. Ebert, Axial fatigue failure sequence and mechanisms in unidirectional fiberglass composites, *J. Compos. Mater., 12*:139 (1978).
56. R. Talreja, Fatigue of composite materials: damage mechanisms and fatigue-life diagrams, *Proc. R. Soc. Lond., A, 378*:461 (1981).

57. L.J. Broutman and S. Sahu, Progressive damage of a glass reinforced plastic during fatigue, *Proceedings 20th Annual Technical Conference*, Society of the Plastics Industry (1969).
58. K. Reifsnider, K. Schultz, and J.C. Duke, Long-term fatigue behavior of composite materials, *Long-Term Behavior of Composites, ASTM STP, 813*:136 (1983).
59. S.S. Wang and E.S.M. Chim, Fatigue damage and degradation in random short-fiber SMC composite, *J. Compos. Mater., 17*:114 (1983).
60. T.R. Smith and M.J. Owen, Progressive nature of fatigue damage in RP, *Mod. Plast., 46*:128 (1969).
61. P.K. Mallick, A fatigue failure warning method for fiber reinforced composite structures, *Failure Prevention and Reliability—1983* (G. Kurajian, ed.), ASME, New York (1983).
62. H.W. Whitworth, Cumulative damage in composites, *ASME J. Eng. Mater. Technol., 112*:358 (1990).
63. L.J. Broutman and S. Sahu, A new theory to predict cumulative fatigue damage in fiberglass reinforced plastics, *Composite Materials: Testing and Design* (*Second Conference*), *ASTM STP, 497*:170 (1972).
64. J.N. Yang, Fatigue and residual strength degradation for graphite/epoxy composites under tension–compression cyclic loadings, *J. Compos. Mater., 12*:19 (1978).
65. M.G. Bader and R.M. Ellis, The effect of notches and specimen geometry on the pendulum impact strength of uniaxial CFRP, *Composites, 6*:253 (1974).
66. R.H. Toland, Failure modes in impact-loaded composite materials, *Symposium on Failure Modes in Composites*, AIME Spring Meeting, May (1972).
67. P.K. Mallick and L.J. Broutman, Static and impact properties of laminated hybrid composites, *J. Test. Eval., 5*:190 (1977).
68. J.L. Perry and D.F. Adams, Charpy impact experiments on graphite/epoxy hybrid composites, *Composites, 7*:166 (1975).
69. N.L. Hancox, Izod impact testing of carbon-fibre-reinforced plastics, *Composites, 3*:41 (1971).
70. M.G. Bader, J.E. Bailey, and I. Bell, The effect of fibre–matrix interface strength on the impact and fracture properties of carbon-fibre-reinforced epoxy resin composites, *J. Phys. D: Appl. Phys., 6*:572 (1973).
71. P. Yeung and L.J. Broutman, The effect of glass-resin interface strength on the impact strength of fiber reinforced plastics, *Polym. Eng. Sci., 18*:62 (1978).
72. P.K. Mallick and L.J. Broutman, Impact properties of laminated angle ply composites, *Eng. Fracture Mech., 8*:631 (1976).
73. G.R. Sidey and F.J. Bradshaw, Some investigations on carbon-fibre-reinforced plastics under impact loading, and measurements of fracture energies, *Carbon Fibres: Their Composites and Applications*, Plastics Institute, London, p. 208 (1971).
74. M.D. Rhodes, J.G. Williams, and J.H. Starnes, Jr., Low-velocity impact damage in graphite-fiber reinforced epoxy laminates, *Proceedings 34th Annual Technical Conference*, Society of the Plastics Industry (1979).
75. R.L. Ramkumar, Effect of low-velocity impact damage on the fatigue behavior of graphite/epoxy laminates, *Long-Term Behavior of Composites, ASTM STP, 813*:116 (1983).
76. J. Morton and E.W. Godwin, Impact response of tough carbon fibre composites, *Compos. Struct., 13*:1 (1989).

77. G.E. Husman, J.M. Whitney, and J.C. Halpin, Residual strength characterization of laminated composites subjected to impact loading, *Foreign Object Impact Damage to Composites, ASTM STP, 568*:92 (1975).
78. G. Kretsis and F.L. Matthews, The strength of bolted joints in glass fibre/epoxy laminates, *Composites, 16*:92 (1985).
79. P.K. Mallick and R.E. Little, Pin bearing strength of fiber reinforced composite laminates, *Proceedings Advanced Composites*, American Society for Metals (1985).
80. T.A. Collings, The strength of bolted joints in multi-directional cfrp laminates, *Composites, 8*:43 (1977).
81. W.J. Quinn and F.L. Matthews, The effect of stacking sequence on the pin-bearing strength in glass fibre reinforced plastic, *J. Compos. Mater., 11*:139 (1977).
82. S. Nilsson, Increasing strength of graphite/epoxy bolted joints by introducing an adhesively bonded metallic insert, *J. Compos. Mater., 23*:641 (1989).
83. J.H. Stockdale and F.L. Matthews, The effect of clamping pressure on bolt bearing loads in glass fibre-reinforced plastics, *Composites, 7*:34 (1976).
84. J.R. Strife and K.M. Prewo, The thermal expansion behavior of unidirectional and bidirectional Kevlar/epoxy composites, *J. Compos. Mater., 13*:264 (1979).
85. S.F.H. Parker, M. Chandra, B. Yates, M. Dootson, and B.J. Walters, The influence of distribution between fibre orientations upon the thermal expansion characteristics of carbon fibre-reinforced plastics, *Composites, 12*:281 (1981).
86. J.R. Kerr and J.F. Haskins, Effects of 50,000 h of thermal aging on graphite/epoxy and graphite/polyimide composites, *AIAA J., 22*:96 (1982).
87. F.E. Devine, Polyester moulding materials in automotive underbonnet environments, *Composites, 14*:353 (1983).
88. C.H. Shen and G.S. Springer, Moisture absorption and desorption of composite materials, *J. Compos. Mater., 10*:2 (1976).
89. G.S. Springer, B.A. Sanders, and R.W. Tung, Environmental effects on glass fiber reinforced polyester and vinyl ester composites, *J. Compos. Mater., 14*:213 (1980).
90. W.W. Wright, The effect of diffusion of water into epoxy resins and their carbon-fibre reinforced composites, *Composites, 12*:201 (1981).
91. O. Gillat and L.J. Broutman, Effect of an external stress on moisture diffusion and degradation in a graphite-reinforced epoxy laminate, *Advanced Composite Materials—Environmental Effects, ASTM STP, 658*:61 (1978).
92. G. Marom and L.J. Broutman, Moisture in epoxy resin composites, *J. Adhes., 12*:153 (1981).
93. E.L. McKague, Jr., J.E. Halkias, and J.D. Reynolds, Moisture in composites: the effect of supersonic service on diffusion, *J. Compos. Mater., 9*:2 (1975).
94. M.J. Adamson, A conceptual model of the thermal-spike mechanism in graphite/epoxy laminates, *Long-Term Behavior of Composites, ASTM STP, 813*:179 (1983).
95. H.T. Hahn, Hygrothermal damage in graphite/epoxy laminates, *J. Eng. Mater. Technol., 109*:1 (1987).
96. C.H. Shen and G.S. Springer, Effects of moisture and temperature on the tensile strength of composite materials, *J. Compos. Mater., 11*:2 (1977).
97. C.H. Shen and G.S. Springer, Environmental effects on the elastic moduli of composite materials, *J. Compos. Mater., 11*:250 (1977).
98. O.K. Joshi, The effect of moisture on the shear properties of carbon fibre composites, *Composites, 14*:196 (1983).
99. C.J. Jones, R.F. Dickson, T. Adam, H. Reiter, and B. Harris, Environmental fatigue of reinforced plastics, *Composites, 14*:288 (1983).

100. P.T. Curtis and B.B. Moore, The effects of environmental exposure on the fatigue behavior of CFRP laminates, *Composites, 14*:294 (1983).
101. C.C. Chamis, R.R. Lark, and J.H. Sinclair, Integrated theory for predicting the hygrothermomechanical response of advanced composite structural components, *Advanced Composite Material—Environmental Effects, ASTM STP, 658*:160 (1978).
102. J.B. Sturgeon, Creep of fibre reinforced thermosetting resins, *Creep of Engineering Materials* (C.D. Pomeroy, ed.), Mechanical Engineering Publishing Ltd., London (1978).
103. J.S. Cartner, W.I. Griffith, and H.F. Brinson, The viscoelastic behavior of composite materials for automotive applications, *Composite Materials in the Automotive Industry* (S.V. Kulkarni, C.H. Zweben, and R.B. Pipes, eds.), American Society of Mechanical Engineers, New York (1978).
104. Y.T. Yeow, D.H. Morris, and H.F. Brinson, Time–temperature behavior of a unidirectional graphite/epoxy composite, *Composite Materials: Testing and Design* (*Fifth Conference*), *ASTM STP, 674*:263 (1979).
105. Y.C. Lou and R.A. Schapery, Viscoelastic characterization of a non-linear fiber-reinforced plastic, *J. Compos. Mater., 5*:208 (1971).
106. M.E. Tuttle and H.F. Brinson, Prediction of the long-term creep compliance of general composite laminates, *Exp. Mech., 26*:89 (1986).
107. M.G. Phillips, Prediction of long-term stress-rupture life for glass fibre-reinforced polyester composites in air and in aqueous environments, *Composites, 14*:270 (1983).
108. R.E. Glaser, R.L. Moore, and T.T. Chiao, Life estimation of an S-glass/epoxy composite under sustained tensile loading, *Compos. Technol. Rev., 5*:21 (1983).
109. R.E. Glaser, R.L. Moore, and T.T. Chiao, Life estimation of aramid/epoxy composites under sustained tension, *Compos. Technol. Rev., 6*:26 (1984).
110. C.E. Harris and D.H. Morris, A damage tolerant design parameter for graphite/epoxy laminated composites, *J. Compos. Technol. Res., 7*:77 (1985).
111. J.F. Mandell, S.S. Wang, and F.J. McGarry, The extension of crack tip damage zones in fiber reinforced plastic laminates, *J. Compos. Mater., 9*:266 (1975).
112. S.K. Gaggar and L.J. Broutman, Crack growth resistance of random fiber composites, *J. Compos. Mater., 9*:216 (1975).
113. C.E. Harris and D.H. Morris, Role of delamination and damage development on the strength of thick notched laminates, *Delamination and Debonding of Materials, ASTM STP, 876*:424 (1985).
114. D.J. Wilkins, J.R. Eisenmann, R.A. Camin, W.S. Margolis, and R.A. Benson, Characterizing delamination growth in graphite–epoxy, *Damage in Composite Materials, ASTM STP, 775*:168 (1980).
115. D.F. Adams, L.A. Carlsson, and R.B. Pipes, *Experimental Characterization of Advanced Composite Materials*, 3rd Ed., CRC Press, Boca Raton, FL (2003).
116. T.K. O'Brien, Characterization of delamination onset and growth in a composite laminate, *Damage in Composite Materials, ASTM STP, 775*:140 (1982).
117. C. Schuecker and B.D. Davidson, Evaluation of the accuracy of the four-point end-notched flexure test for mode II delamination toughness determination, *Compos. Sci. Tech., 60*:2137 (2000).
118. O. Ishai, H. Rosenthal, N. Sela, and E. Drukker, Effect of selective adhesive interleaving on interlaminar fracture toughness of graphite/epoxy composite laminates, *Composites*, *19*:49 (1988).
119. E.W.Y. Lee and W.S. Chan, Delamination arrestment by discretizing the critical ply in a laminate, AIAA Paper No. 89-1403, *Amer. Inst. Aero. Astro*., 1989.

120. C.T. Sun, Intelligent tailoring of composite laminates, *Carbon*, *27*:679 (1989).
121. L.A. Mignery, T.M. Tan, and C.T. Sun, The use of stitching to suppress delamination in laminated composites, *Delamination and Debonding, ASTM STP, 876*:371 (1985).
122. J.H. Byun, J.W. Gillespie, and T.W. Chou, Mode I delamination of a three-dimensional fabric composite, *J. Compos. Mater., 24*:497 (1990).
123. W.S. Chan and O.O. Ochoa, Suppression of edge delamination by terminating a critical ply near edges in composite laminates, *Key Engineering Materials Series*, Vol. 37, Transtech Publications, p. 285 (1989).
124. C.T. Sun and G.D. Chu, Reducing free edge effect on laminate strength by edge modification, *J. Compos. Mater., 25*:142 (1991).

PROBLEMS

P4.1. The load–strain data obtained in a tension test of a unidirectional carbon fiber–epoxy composite are given in the following table. Specimen dimensions are length = 254 mm, width = 12.7 mm, and thickness = 1.4 mm.

1. Determine the tensile modulus and Poisson's ratio for each fiber orientation
2. Using Equation 3.45, determine the shear modulus, G_{12} of this material and then verify the validity of Equation 3.46 for the 45° orientation

	Load (*N*)			**Transverse Strain, %**		
Axial Strain, %	**0°**	**45°**	**90°**	**0°**	**45°**	**90°**
0.05	2130	130	67	−0.012	−0.00113	−0.0004
0.10	4270	255	134	−0.027	−0.0021	−0.001
0.15	6400	360	204	−0.041	−0.0029	−0.0014
0.20	8620	485	333	−0.054	−0.0038	−0.0019
0.25	—	565	396	—	−0.0048	−0.0025

P4.2. The following tensile modulus (E_{xx}) values were calculated from the tensile stress–strain diagrams of 30° carbon fiber–epoxy off-axis specimens:

L/w	**E_{xx}(10^6 psi)**
2	2.96
4	2.71
8	2.55

Using the following material properties, calculate the corrected tensile modulus values at each L/w and compare them with the theoretical modulus: $E_{11} = 20 \times 10^6$ psi, $E_{22} = 1 \times 10^6$ psi, $\nu_{12} = 0.25$, and $G_{12} = 0.6 \times 10^6$ psi.

P4.3. The following longitudinal tensile strength data (in MPa) were obtained for a $[0/\pm45/90]_S$ E-glass fiber–epoxy laminate: 520.25, 470.27, 457.60, 541.18, 566.35, 489.82, 524.55, 557.87, 490.00, 498.99, 496.95, 510.84, and 558.76.

(a) Determine the average tensile strength, the standard deviation, and coefficient of variation

(b) Determine the Weibull parameters for the given strength distribution

(c) Using the Weibull parameters in (b), determine the mean strength for the material

P4.4. The tensile stress–strain diagram for a $[(0/90)_2/0/\overline{90}]_S$ E-glass fiber–epoxy laminate is shown in the figure. Determine the initial modulus, the stress at the knee point, the secondary modulus, and the failure strength for the laminate. Compare these experimental values with the theoretical estimates.

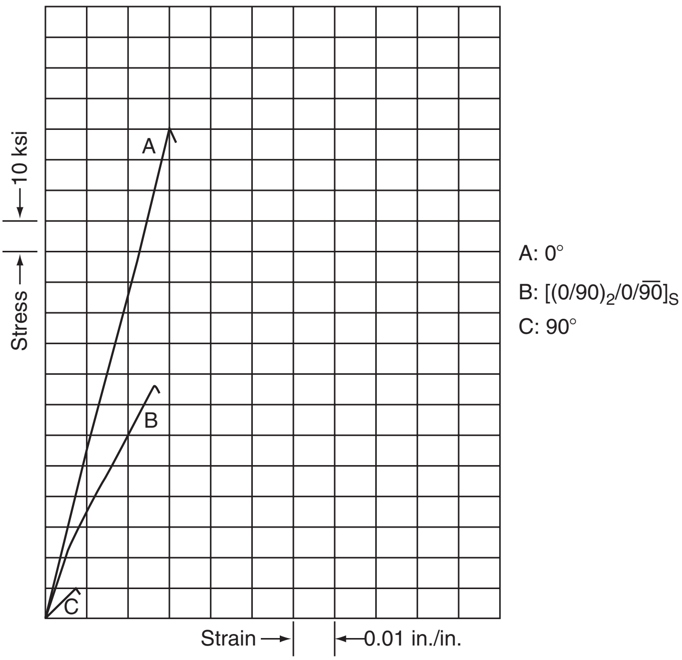

P4.5. Tensile stress–strain diagram of a $[0/90_4]_S$ AS-4 carbon fiber–epoxy laminate is shown in the figure. The longitudinal modulus and transverse modulus of a 0° unidirectional laminate of the same material are 142 and 10.3 GPa, respectively.

1. Determine the initial axial modulus of the $[0/90_4]_S$ laminate and compare it with the theoretical value. How would this value change if the 90° layers are at the outside or the laminate construction is changed to $[0_2/90_3]_S$?
2. The knee in the stress–strain diagram is at a strain of 0.005 mm/mm. However, the ultimate longitudinal and transverse strains of the 0° unidirectional laminate are at 0.0146 and 0.006 mm/mm, respectively. Explain what might have caused a lower strain at the knee
3. Describe the reason for the nonlinear portion of the stress–strain diagram

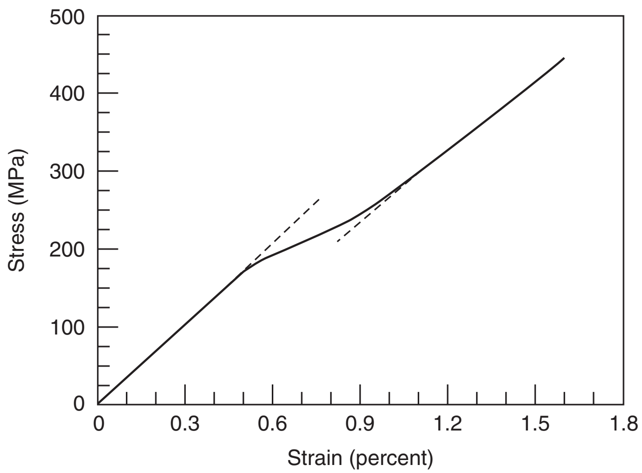

P4.6. The longitudinal compressive strength of a unidirectional 0° carbon fiber–epoxy laminate is estimated as 190 ksi. Using the Euler buckling formula for homogeneous materials, design the minimum thickness of a Celanese compression specimen that will be required to avoid lateral buckling.

P4.7. The following compressive strength data were obtained for a 0° unidirectional surface-treated high-strength carbon fiber–epoxy composite tested in the longitudinal (fiber) direction.* The composite specimens failed by shear cracks at 45° to the axis of loading.

* N.L. Hancox, The compression strength of unidirectional carbon fibre reinforced plastic, *J. Mater. Sci., 10*:234 (1975).

v_f (%)	σ_{LCU} (MPa)
10	325
20	525
30	712
40	915
50	1100
60	1250
70	1750

Plot the data and verify that the compressive strength is linear with v_f. Assuming that the rule of mixture applies, determine the longitudinal compressive strength of the carbon fiber. How may the compressive strength and failure mode of the composite be affected by matrix strength and fiber surface treatment?

P4.8. The following tensile stress–strain values were obtained in uniaxial tensile testing of a $[\pm 45]_S$ laminate:

σ_{xx} (MPa)	ε_{xx} (mm/mm)	ε_{yy} (mm/mm)
27.5	0.001	−0.00083
54.4	0.002	−0.00170
82.7	0.003	−0.00250
96.5	0.004	−0.00340
115.7	0.005	−0.00700
132.5	0.006	−0.00811
161.0	0.007	−0.00905
214.0	0.014	−0.01242

Plot the data and determine the E_{xx} and ν_{xy} of the laminate. In addition, reduce the data to plot τ_{12} vs. γ_{12} for the material and determine G_{12}.

P4.9. Using the stress and strain transformation Equations 3.30 and 3.31, verify Equations 4.16 and 4.17 for the 10° off-axis test shown in Figure 4.28.

P4.10. The following table* gives the stress–strain data for $[0/90/\pm 45]_S$ and $[0/90]_{2S}$ AS-4 carbon fiber–epoxy laminates obtained in a three-rail shear test. Plot the data and determine the shear modulus for each laminate. Compare these values with those predicted by the lamination

* S. Tan and R. Kim, Fracture of composite laminates containing cracks due to shear loading, *Exp. Mech., 28*:364 (1988).

theory based on the following material properties: $E_{11} = 143.92$ GPa, $E_{22} = 11.86$ GPa, $G_{12} = 6.68$ GPa, and $\nu_{12} = 0.326$.

	Shear Stress (MPa)	
Shear Strain (%)	**$[0/90/\pm45]_S$**	**$[0/90]_{2S}$**
0.2	40	13.6
0.4	91	24.5
0.6	128.6	37
0.8	155	47.3
1.0	178	54.5
1.2	208	62
1.4	232	65.4
1.6	260	70

P4.11. The following figure shows the schematic of an asymmetric four-point bend (AFPB) test developed for measuring the shear properties of composite laminates. As in the Iosipescu shear test, it uses a V-notched beam specimen. Derive an expression for the shear stress at the center of the specimen and compare it with that in the Iosipescu shear test.

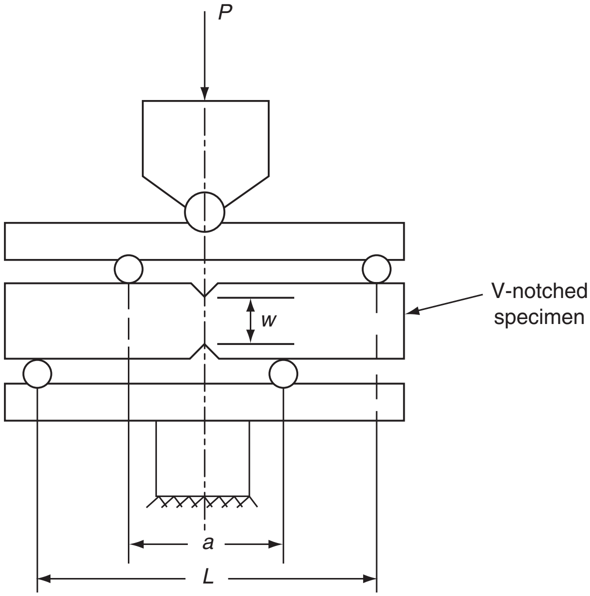

P4.12. Torsion of a thin-walled tube is considered the best method of creating a pure shear stress state in a material. Describe some of the practical problems that may arise in the torsion test of a laminated composite tube.

P4.13. Using Equation 4.12, develop a correction factor for the modulus measurements in a three-point flexure test with a small span–thickness ratio and plot the ratio of corrected modulus and measured modulus as a function of the span–thickness ratio.

P4.14. Using the homogeneous beam theory, develop equations for flexural strength and modulus calculations from the load–deflection diagram in a four-point static flexure test.

P4.15. Using the lamination theory, develop the flexural load–deflection diagram (up to the point of first failure) of a sandwich hybrid beam containing 0° T-300 carbon fiber-reinforced epoxy in the two outer layers and 0° E-glass fiber-reinforced epoxy in the core. Describe the failure mode expected in flexural loading of such a beam.

P4.16. Unidirectional 0° Kevlar 49 composites exhibit a linear stress–strain curve in a longitudinal tension test; however, their longitudinal compressive stress–strain curve is similar to that of an elastic, perfectly plastic metal (see the figure). Furthermore, the compressive proportional limit for a Kevlar 49 composite is lower than its tensile strength. Explain how these two behaviors may affect the stress distribution across the thickness of a unidirectional Kevlar 49 composite beam as the transversely applied load on the beam is increased. Estimate the transverse load at which the flexural load–deflection diagram of a Kevlar 49 beam becomes nonlinear. (*Hint*: Assume that the strain distribution through the thickness of the beam remains linear at all load levels.)

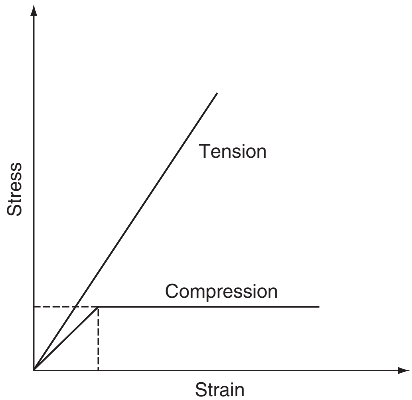

P4.17. The flexural strength of a unidirectional 0° E-glass–vinyl ester beam is 95 ksi, and the estimated ILSS for the material is 6 ksi. Determine the maximum span–thickness ratio for a short-beam shear specimen in which interlaminar shear failure is expected.

P4.18. Some investigators have proposed using a four-point flexure test for ILSS measurements. Using the homogeneous beam theory, develop equations for ILSS in a four-point flexure test and discuss the merits of such a test over a three-point short-beam shear test.

P4.19. Using Table 4.8, compare the fatigue strengths of T-300 carbon–epoxy and E-glass–epoxy composites at 10^4 and 10^7 cycles.

P4.20. The Weibull parameters for the tension–tension fatigue life distribution of a $[0/90/\pm45]_S$ T-300 carbon fiber–epoxy composite are as follows: at $\sigma_{max} = 340$ MPa, $L_0 = 1{,}000{,}000$, and $\alpha_f = 1.6$. At $\sigma_{max} = 410$ MPa, $L_0 = 40{,}000$, and $\alpha_f = 1.7$.

1. Determine the mean fatigue lives at 340 and 410 MPa
2. What is the expected probability of surviving 50,000 cycles at 410 MPa?

P4.21. Fatigue lives (numbers of cycles to failure) of twelve 0° Kevlar 49 fiber-reinforced composite specimens in tension–tension cycling at 90% UTS, $R = 0.1$, 0.5 Hz frequency, and 23°C are reported as 1,585; 25; 44,160; 28,240; 74,140; 47; 339,689; 50,807; 320,415; 865; 5,805; and 4,930. Plot the Weibull distribution curve for these fatigue lives and determine the Weibull parameters for this distribution.

P4.22. For the major portion of the fatigue life of a composite laminate, the instantaneous modulus can be modeled as

$$E = E_0(1 - c\ \log N)$$

where
E_0 = initial modulus at $N = 1$
N = number of fatigue cycles
c = an experimentally determined damage-controlling factor

Using this model, determine the number of cycles that a simply supported centrally loaded beam can endure before its deflection becomes 50% higher than its initial value.

P4.23. For the quasi-isotropic laminate described in Example 4.2, suppose the loading sequence is 10,000 cycles at 437 MPa followed by cycling to failure at 382 MPa. Estimate the total life expected in this high–low stress sequence using (a) the Whitworth model and (b) the Miner's rule.

P4.24. The mean fatigue lives of $[0/90]_S$ E-glass fiber–epoxy laminates at maximum stress levels of 56,000 and 35,000 psi are 1,500 and 172,000, respectively. The static tensile strength of this material is 65,000 psi.

1. Determine the residual static strength of this material after 50% of the fatigue life at each stress level
2. After cycling for 50% of the fatigue life at 35,000 psi, the maximum stress level in a fatigue specimen is increased to 56,000 psi. Estimate the number of cycles the specimen would survive at 56,000 psi
3. If the first stress level is 56,000 psi, which is then followed by 35,000 psi, estimate the number of cycles at the second stress level

P4.25. Adam et al.* have found that, depending on the fiber type, the post-fatigue residual strength of [0/90] cross-plied composites may show either a gradual decrease with increasing number of cycles (usually after a rapid reduction in the first few cycles) or virtually no change until they fail catastrophically (sudden death). They proposed the following empirical equation to predict the residual strength:

$$\sigma_{\text{res}} = \sigma_{\max}(\sigma_{\text{U}} - \sigma_{\max})(1 - r^x)^{1/y},$$

where

$$r = \frac{\log N - \log 0.5}{\log N_{\text{f}} - \log 0.5}$$

x, y = parameters obtained by fitting the residual strength equation to the experimental data (both vary with material and environmental conditions)

Graphically compare the residual strength after fatigue for the following $[(0/90)_2/0/90]_S$ epoxy laminates at $\sigma_{\max} = 0.9, 0.7$, and $0.5\ \sigma_{\text{U}}$:

Fiber	**σ_{U} (MPa)**	**x**	**y**
HTS carbon	944	1.8	23.1
E-glass	578	1.5	4.8
Kevlar 49	674	2.1	8.8

P4.26. Poursartip et al.† have proposed the following empirical equation to represent the fatigue damage (delamination) growth rate at $R = 0.1$ in $[\pm 45/90/45/0]_S$ carbon fiber–epoxy laminate:

$$\frac{\mathrm{d}D}{\mathrm{d}N} = k_1 \left(\frac{\Delta\sigma}{\sigma_{\text{U}}}\right)^{k_2},$$

* T. Adam, R.F. Dickson, C.J. Jones, H. Reiter, and B. Harris, A power law fatigue damage model for fibre-reinforced plastic laminates, *Proc. Inst. Mech. Eng., 200*:155 (1986).

† A. Poursartip, M.F. Ashby, and P.W.R. Beaumont, The fatigue damage mechanics of fibrous composites, *Polymer NDE* (K.H.G. Ashbee, ed.), Technomic Pub. Co. (1986).

where

D = damage (ratio of delaminated area to total surface area)

$\Delta\sigma$ = stress range

σ_U = ultimate tensile strength

k_1, k_2 = constants determined by fitting a least-square regression line to damage growth rate vs. stress range data

Assuming that the damage can be represented by

$$D = k_3(1 - E/E_0),$$

where

E is the modulus after N cycles

E_0 is the initial modulus

k_3 is a constant

Find expressions for the terminal damage and the number of cycles to failure in terms of $\Delta\sigma$.

P4.27. The following figure shows the load–time curve recorded during the instrumented Charpy impact testing of an unnotched 0° T-300 carbon–epoxy specimen. The pendulum velocity just before impacting the specimen was 16.8 ft./s. The specimen dimensions were as follows: length between specimen supports = 1.6 in.; thickness = 0.125 in.; and width = 0.5 in. Calculate the dynamic flexural strength, dynamic flexural modulus, initiation energy, propagation energy, and total impact energy for the specimen. State your assumptions and critically evaluate your answers.

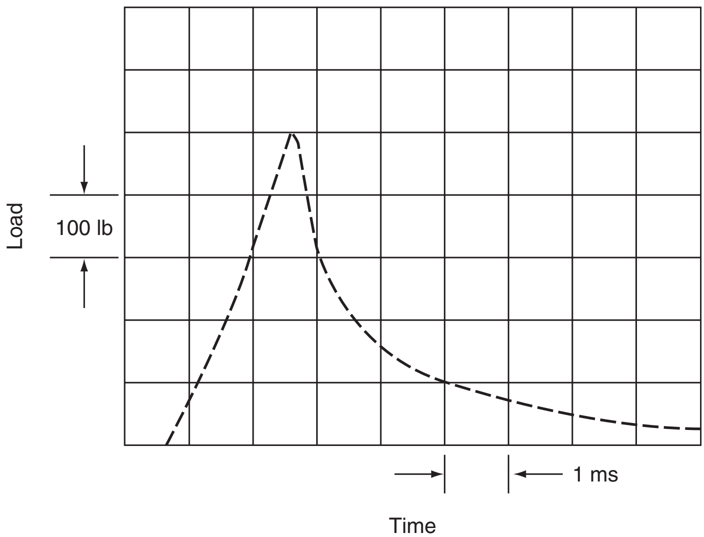

P4.28. In a drop-weight impact test, a 1 in. diameter spherical ball weighing 0.15 lb is dropped freely on 0.120 in. thick $[0/\pm45/90]_{3S}$ carbon fiber–epoxy beam specimens and the rebound heights are recorded. The beam specimens are simply supported, 0.5 in. wide and 6 in. long between the supports. The drop heights, rebound heights, and specimen deflections in three experiments are as follows:

Drop Height (ft)	**Rebound Height (ft)**	**Measured Maximum Deflection (in.)**
1	0.72	0.056
4	2.20	0.138
6	3.02	0.150

(a) Calculate the energy lost by the ball in each case.
(b) Assuming that all of the energy lost by the ball is transformed into strain energy in the beam, calculate the maximum deflection of the specimen in each case. The flexural modulus of the laminate is 20×10^6 psi.
(c) Explain why the measured maximum deflections are less than those calculated in (b).

P4.29. The following table* gives the tensile strength and Charpy impact energy data of a unidirectional hybrid composite containing intermingled carbon and Spectra 1000 polyethylene fibers in an epoxy matrix. The polyethylene fibers were either untreated or surface-treated to improve their adhesion with the epoxy matrix. Plot the data as a function of the polyethylene fiber volume fraction and compare them with the rule of mixture predictions. Explain the differences in impact energy in terms of the failure modes that might be expected in untreated and treated fiber composites. Will you expect differences in other mechanical properties of these composites?

* A.A.J.M. Peijs, P. Catsman, L.E. Govaert, and P.J. Lemstra, Hybrid composites based on polyethylene and carbon fibres, Part 2: Influence of composition and adhesion level of polyethylene fibers on mechanical properties, *Composites, 21*:513 (1990).

Polyethylene Fiber Volume Fraction (%)	Tensile Strength (MPa)		Charpy Impact Energy (kJ/m^2)	
	Untreated	Treated	Untreated	Treated
0	1776	1776	90.8	98.8
20	1623	1666	206	100
40	1367	1384	191	105.1
60	1222	1282	171.2	118.2
80	928	986	140.8	124.8
100	1160	1273	116.7	145.3

P4.30. Show that the time required for a material to attain at least 99.9% of its maximum possible moisture content is given by

$$t = \frac{0.679c^2}{D_z},$$

where
t is time in seconds
c is the laminate thickness

P4.31. The maximum possible moisture content in a $[0/90/\pm45]_S$ T-300 carbon fiber–epoxy composite ($v_f = 0.6$) is given by

$$M_m = 0.000145(\text{RH})^{1.8}.$$

A 6.25 mm thick panel of this material is exposed on both sides to air with 90% relative humidity at 25°C. The initial moisture content in the panel is 0.01%.

(a) Estimate the time required for the moisture content to increase to the 0.1% level
(b) If the panel is painted on one side with a moisture-impervious material, what would be the moisture content in the panel at the end of the time period calculated in (a)?

P4.32. Following Equation 4.43, design an experiment for determining the diffusion coefficient, D_z of a composite laminate. Be specific about any calculations that may be required in this experiment.

P4.33. Estimate the transverse tensile strength, transverse modulus, and shear modulus of a 0° unidirectional T-300 carbon fiber-reinforced epoxy composite ($v_f = 0.55$) at 50°C and 0.1% moisture content. The matrix tensile strength, modulus, and Poisson's ratio at 23°C and dry conditions are 56 MPa, 2.2 GPa, and 0.43, respectively; T_{gd} for the matrix is 177°C.

P4.34. Shivakumar and Crews* have proposed the following equation for the bolt clamp-up force F_t between two resin-based laminates:

$$F_t = \frac{F_0}{1 + 0.1126(t/a_{th})^{0.20}},$$

where
F_0 = initial (elastic) clamp-up force
t = elapsed time (weeks)
a_{th} = a shift factor corresponding to a specific steady-state temperature or moisture

1. At 23°C, the a_{th} values for an epoxy resin are 1, 0.1, 0.01, and 0.001 for 0%, 0.5%, 1%, and 1.5% moisture levels, respectively. Using these a_{th} values, estimate the time for 20%, 50%, 80%, and 100% relaxation in bolt clamp-up force.
2. At 66°C and 0.5% moisture level, the bolt clamp-up force relaxes to 80% of its initial value in 3 weeks. Calculate the a_{th} value for this environmental condition.

P4.35. A quasi-isotropic $[0/\pm45/90]_{8S}$ panel of T-300 carbon fiber–epoxy develops a 12 mm long sharp crack at its center. The panel width and thickness are 200 and 8 mm, respectively. The unnotched tensile strength of the laminate is 565 MPa. Determine the safe load that can be applied normal to the crack plane before an unstable fracture occurs. Describe the possible fracture modes for the cracked panel.

P4.36. The load–displacement record shown in the figure was obtained in a double-cantilever beam (DCB) test of a unidirectional 0° carbon fiber–epoxy laminate. The initial crack length was 25 mm and the specimen was unloaded–reloaded after crack extension of every 5 mm. Plot (a) compliance vs. crack length and (b) strain energy release rate G_I vs. crack length for this specimen. What is the Mode I interlaminar fracture toughness of this material? The specimen width was 25 mm.

---

* K.N. Shivakumar and J.H. Crews, Jr., Bolt clamp-up relaxation in a graphite/epoxy laminate, *Long-Term Behavior of Composites, ASTM STP, 813*:5 (1983).

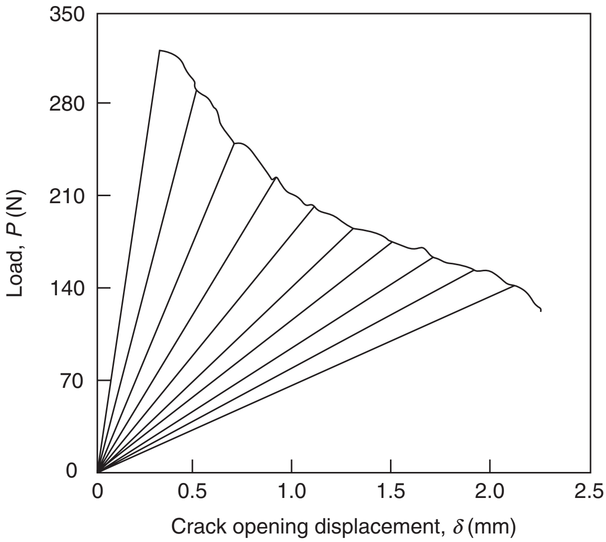

P4.37. The compliance data obtained in a 4-ENF test of a 0° unidirectional carbon fiber–epoxy laminate are given in the following table. The specimen width was 25.4 mm and the initial crack length was 50 mm. The load at which the initial crack was observed to grow was 700 N.

Determine the Mode II interlaminar fracture toughness of the material.

Crack Length (mm)	**Compliance (mm/N)**
60	5.85×10^{-3}
65	6.20×10^{-3}
70	6.60×10^{-3}
75	6.96×10^{-3}